STUDIES OF SOFT X-RAY EMISSION DURING SOLAR FLARES

by

MANDAYAM NAYAKA ANANDARAM

M.Sc, St. Francis Xavier University, 1970

A DISSERTATION SUBMITTED IN PARTIAL FULFILLMENT
OF THE REQUIREMENTS FOR THE DEGREE OF

DOCTOR OF PHILOSOPHY

in the Department
of
Physics

ACCEPTED
FACULTY OF GRADUATE STUDIES

....
DEAN

DATE..

We accept this dissertation as conforming
to the required standard

. . . .

. . . .

. . . .

. . . .

. . . .

. . . .

UNIVERSITY OF VICTORIA

September 1973

Supervisor : Dr. Jeremy B. Tatum

ABSTRACT

Solar flare soft x-ray emission from 0.5 Å to 8.5 Å was observed during 1967-68 by U S Naval Research Laboratory Bragg crystal (LiF and EDDT) spectrometers aboard the OSO-4 satellite and also by NRL broad band ionization detectors aboard the OGO-4 satellite.

In this work, instrumental parameters for the LiF crystal spectrometer based on experimental values have been determined and used in the data analysis. The source continuum spectra between 1 Å and 3.8 Å have been obtained for selected flares from OSO-4 spectrometer scans. As these spectra are each affected by time variations over 14 minutes, they are compared with the thermal continuum (free-free and free-bound) spectra predicted in the following manner. The instantaneous electron kinetic temperature and emission measure (equal to the product of the square of the electron number density and the total volume) of the flare plasma are determined from the available OGO-4 broad band data. The expected continuum flux is calculated by using these parameters. The comparison shows that there is good agreement between 2 Å and 3.8 Å. Thus it has been concluded that reliable values of the average electron temperature can be determined from the OGO-4 flare data.

The earlier wavelength assignment and line identification list published by Meekins et al (1970, Solar Physics 13, 198) has been substantially improved in this work by separately summing a large number of OSO-4 spectrometer scans of the flaring and active sun. All identified wavelengths are found to agree with the more accurate theoretical values to within ± 0.01 Å. Identifications of several weak lines as due to hydrogen-like and helium-like ions of chlorine and phosphorus have also been suggested. The temporal behaviour of selected ion line intensities (due to Fe, Ca, Si, S, Al, and Mg) indicates that they follow the expected temperature variations during the flare.

The total continuum emission in the 0.5 to 3 Å and the 1 to 8 Å broad band segments has been determined from OGO-4 data for 21 flares. In doing this, a simple and approximate method of converting the total emission based on the gray body approximation (in which the OGO-4 data are reported) to one based on the thermal continuum spectrum has been developed. This study shows that the total energy lost in the 0.5 to 8 Å soft x-ray channel is of the order of 10^{28} to 10^{30} ergs depending on the $H\alpha$ importance of the flare (from sub- to class 2); it is also shown that this energy is comparable with that emitted in higher wavelength segments estimated by other authors.

....

....

....

....

....

ACKNOWLEDGEMENTS

I would like to thank a number of people for their enthusiastic help in making this dissertation research possible.

I thank my supervisor Dr. Jeremy Tatum for his constant encouragement and his wholehearted help during the course of my studies and research in the university. I also thank him and the University of Victoria for their financial support.

I thank the dedicated group of solar physicists at the U. S. Naval Research Laboratory, Washington, D.C., without whose interest, advice and help during my summer visits, this research would not have been possible. They are, Dr. George Doschek, Dr. Donald Horan, Dr. John Meekins, Mr. Robert Kreplin, and Mr. Arlyn Unzicker. In particular, I thank Dr. Doschek for suggesting the topics for research as well as lending the large amount of OSO-4 spectrometer data for my study; Dr. Meekins for kindly giving data on the measured values of LiF crystal reflectivities; Dr. Horan and Mr. Kreplin for lending OGO-4 broad band data; Mr. Unzicker for his invaluable help in determining the efficiency of OSO-4 detectors. I am also grateful to these people for the stimulation and insight they have provided in my discussions with them.

My thanks also go to Dr. Richard Tousey for introducing me to the NRL group and the authorities of NRL for allowing me to work in their laboratory.

I thank the members of my supervisory committee who have signed the title page, for the many contributions they have made toward improving the content of this dissertation, and for being prompt in reading and commenting on the manuscript.

I thank Mr. W. Nottingham of the Martin Marietta Corporation for summing the selected OSO-4 scans from their data tapes and my colleague Mr. Don Van den Berg for his assistance in computer programming.

Finally, I thank my wife Usha for her encouragement, patience and assistance. In addition to her full-time work, she has spent her evenings and weekends typing the entire dissertation. She also suggested occasional improvements in the style and I am very proud to acknowledge her help in the production of this dissertation. I also thank my parents for their interest in my progress.

TABLE OF CONTENTS

TABLE OF CONTENTS (Continued)

LIST OF TABLES

LIST OF FIGURES

LIST OF FIGURES (Continued)

CHAPTER I

INTRODUCTION

I.1 BACKGROUND

Solar radiation spans all regions of the electromagnetic spectrum from the radio wavelengths to hard x-rays below 1 Angstrom. This thesis is concerned with the study of the solar soft x-ray emission in the wavelength region 1 to 8.5 Å observed by the Naval Research Laboratory experiments aboard several orbiting satellites.

Solar radiation in the visible region has been studied by means of ground based instrumentation ever since Fraunhofer first observed the solar absorption lines. However, solar x-radiation has not been available for analysis until recently because of absorption by the earth's atmosphere. The extent of absorption as a function of the wavelength of the radiation is shown in Figure I-1. Hulburt (1938) was one of the first to suggest that the sun emits x-rays and that this was responsible for the earth's ionosphere. The fact that sudden ionospheric disturbances seemed to be closely related to solar flares suggested that the sun's ionizing radiation is enhanced during these chromospheric eruptions and that this emission originated in the same general region as the optical flare (Martyn et al., 1937; Newton and Barton, 1937; and Giovanelli, 1938). The ionosphere can thus be treated as a broad band detector for solar x- and ultra-violet radiation (Kundu, 1965; Donnelly, 1968, 1969; and Mitra, 1972). The exact analysis, however, is subject to uncertainties regarding the constituents of the earth's upper atmosphere, incident solar radiation and atomic rate parameters applicable to ionospheric reactions. These may cause wrong interpretations. An example is the now incorrect assumption (Hallam,

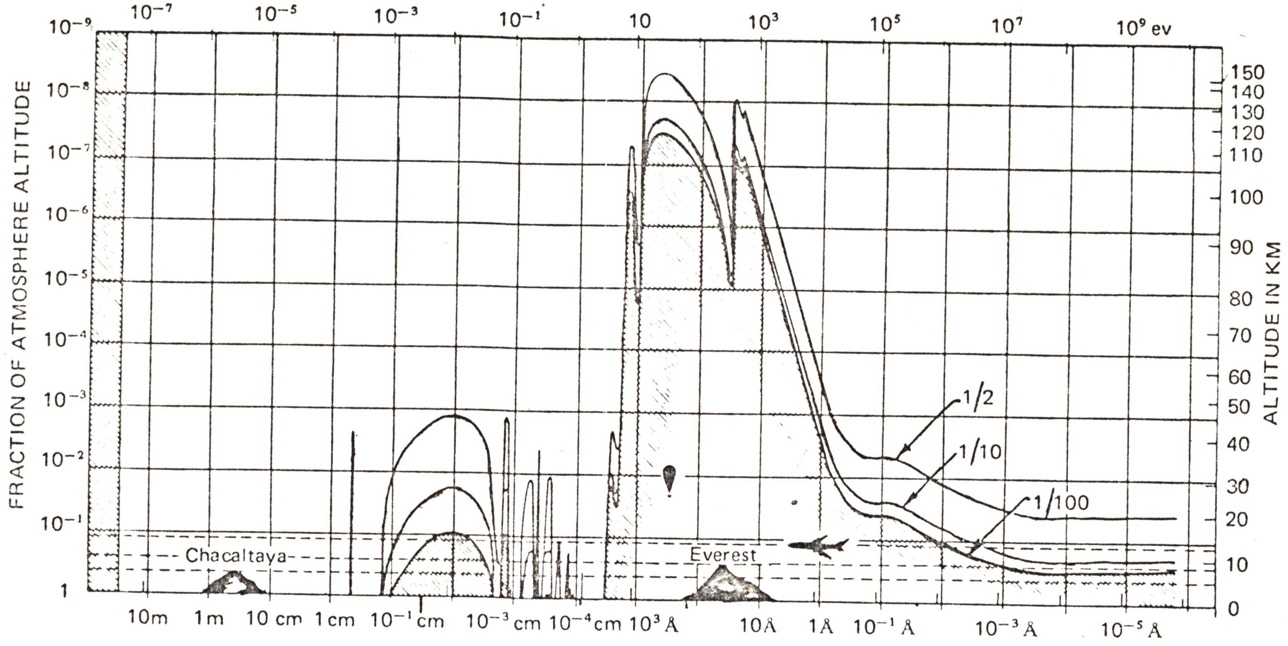

Figure I-1. Attenuation of radiation by the atmosphere as a function of wavelength. The curves show the altitude at which the spectral energy is reduced to 1/2, 1/10, and 1/100 of that outside the atmosphere (Giacconi, 1973).

1964) that most of the enhanced ionizing radiation during a solar flare is due to the hydrogen Lyman-alpha emission (Warwick, 1963). Many x-ray bursts of small amplitude do not produce any observable ionospheric effects (Dickerman and Thornton, 1966). The Figure I-1 also shows that balloon flights, which have been used to study hard x-rays (Peterson and Winckler, 1958), can not reach the altitude at which soft x-rays retain much of their spectral characteristics. Thus, ground-based and low-altitude observations are inadequate for the study of soft x-radiation. Direct observations by rockets or satellites above the earth's atmosphere are the only recourse (Thomas, 1970).

The U. S. Naval Research Laboratory (NRL) investigators have pioneered these techniques (Friedman, 1960). The first experimental evidence for solar soft x-radiation ($>$ 1 Å) (Burnight, 1949) came with the darkening of a photographic plate shielded by a thin beryllium filter, when it was flown in a V-2 rocket flight on August 6, 1948. Subsequent rocket flights (V-2 and Aerobee) by the NRL group led to the improvement of the instrumentation for more detailed studies (Friedman 1962, 1963) and are conducted even now to study solar eclipses (Speer et al., 1970). These rocket flights provided information about the main characteristics of solar soft x-radiation. They showed that increases in soft x-rays (1-8 Å) were responsible for ionizing the D-region of the ionosphere, and therefore responsible for high-frequency radio fade-out and sudden ionospheric disturbances. However, these sub-orbital flights suffered from serious drawbacks. One was that the flights lasted only a few minutes and could not observe the x-ray activity over long periods of time; the other was that they could not be made to coincide with the peak of x-ray enhancements during solar flares.

Thus it was clear that only orbiting satellites instrumented for x-ray observation could provide the needed long term, continuous monitoring capability. NRL was the first to launch a successful solar x-ray satellite, SOLRAD 1 in June 1960 (Kreplin et al., 1962). UK, USSR and other countries have also developed their own programs to study solar x-radiation (eg., Culhane et al., 1969b). NRL alone has launched ten SOLRAD satellites so far, each with improvements in detection sensitivity and has also placed x-ray detectors aboard other satellites. In the interval from March 1967 to March 1968 about a dozen satellites were monitoring the solar x-radiation (OGO-4 and -5, OSO-3 and -4, Explorers 30, 33, 35, and 37, Cosmos 166, Vela 7 and 8 to name a few). Many of these carried broad-band detectors giving a single output proportional to the flux received in the 2 - 12 Å band or in the 8 - 12 Å band. Some, such as OGO-4, contained several detectors sensitive to different segments of the soft x-ray flux (eg., 0.5 - 3, 1 - 8, 8 - 20 and 44 - 60 Å). This provision makes it possible to determine the electron temperatures and emission measures of solar flares (described in Chapter III). Among several experiments, OSO-4 carried x-ray proportional counters (Culhane et al., 1969b), an x-ray telescope experiment (Vaiana and Giacconi, 1969) and NRL Bragg crystal spectrometers (Meekins,1972) covering the 1 - 8 Å region. These experiments provided detailed and continuous coverage of solar activity in the x-ray region.

I.2 IMPORTANCE OF SOLAR X-RAY OBSERVATION

There are several advantages in investigating the x-ray emissions compared to the visual observations. Some of these, which are summarised below (Moser, 1967; Thomas, 1970; Walker, 1972), have motivated the research reported in this thesis. They are:

(a) The x-ray emitting (or active) regions in the corona can be observed during their entire disk passage, while the coronal condensations can be seen in visible light only at the limb.

(b) Continuous x-ray monitoring has the ability to "see" active regions long before any plages or sunspots are visually observed. Enhancements of x-rays have been detected as much as two days prior to visual sightings. Also, events associated with active regions have been observed for one or two days after these regions passed out of view around the west limb of the sun. (This fact indicates that x-rays are emitted from regions high above the photosphere)

(c) Because visual flares are classified by areas and not by energy output, it is not possible to know when a particular flare will cause terrestrial atmospheric disturbances. Since x-ray bursts are usually associated with solar flares and last longer than the observable flash phase, they give more information on these complex phenomena.

(d) Soft x-ray enhancement is the very first manifestation of a solar flare. By monitoring continuously the x-radiation we can predict with better accuracy periods of increased solar activity. The objective of the SOLRAD program is to provide a flare early-warning system. This is a necessity since large x-ray bursts are known to completely disrupt radio and telecommunications.

(e) Solar x-radiation gives information about plasma under conditions unobtainable in the laboratory. The coronal spectrum provides a unique opportunity to investigate the thermal and non-thermal atomic processes in high-temperature plasmas. Since the active and flaring regions consist of very hot plasmas confined by magnetic fields, and since bursts seem to be related to instabilities in these fields, solar x-ray observations also touch on problems associated with controlled thermonuclear fusion.

(f) A thorough knowledge of solar x-ray emission processes will give rise to a better understanding of the activity of flare stars and cosmic x-ray sources which are now being investigated by UHURU (Giacconi, 1973) and other satellites.

I.3 PLAN OF THE THESIS

This thesis deals with the analysis of the soft x-ray emission data obtained by the NRL Bragg crystal spectrometer experiment aboard OSO-4 and by the broad-band ionization chambers aboard OGO-4 from October 1967 to March 1968.

This thesis begins with a review of the important atomic processes responsible for the x-ray continuum and line emission in the coronal plasma. The processes discussed in Chapter II are thermal electron bremsstrahlung and radiative recombination which are mainly responsible for the continuum emission ; and electron impact excitation, dielectronic recombination and inner-shell excitation, which are responsible for the line emission.

The development of the OGO-4 broad-band detectors and the OSO-4 Bragg spectrometers are largely the work of the two principal NRL investigators Robert Kreplin and John Meekins respectively. Horan (1970, 1971) has analyzed the OGO-4 data for solar flares by determining the time history of the electron temperature T (K) and the characteristic emission measure defined by $N_e^2 V$ (cm^{-3}) where N_e is the number of electrons per unit volume and V is the volume of the flare plasma. Meekins et al., (1968, 1970) reported the wavelengths and line identifications based on their analysis of the spectrometer data (1 to 8.5 Å). Meekins et al., (1970) were able to qualitatively account for the observed continuum by assuming the processes which are described in Chapter II. They noted that the line intensities appeared to indicate different electron temperatures and hence argued that the flare plasma had a multithermal composition. Chapter III is devoted to a brief review of the principles of these experiments and the results obtained by the above mentioned investigators.

The work of Meekins, Doschek and their coworkers were, however, based on either the uncorrected data or data corrected by theoretical instrumental parameters for the Bragg spectrometers. They found (Doschek, private communication) that one of the major causes of uncertainty in the theoretical correction parameters was the uncertain composition of the mica window of the spectrometer Geiger counters. In addition, the theoretical analysis of He-like and Li-like ion lines by Gabriel and Jordan (1969a, 1969b), and Gabriel (1972b), and identifications of optical transitions in highly ionized iron ions by Doschek et al., (1972) indicated that there were a few mis-identifications in the OSO-4 line list reported by Meekins et al., (1970). In the light of these developments, Chapter IV will describe the work done on the first two objectives of this thesis, viz.,

(i) to determine experimentally the absolute quantum efficiency of the Geiger counters (sample numbers 1176 and 1186) and thereby obtain more reliable instrumental parameters, and

(ii) to obtain a revised list of the OSO-4 wavelength and line identifications by a selective summation of a large number of spectrometer scans.

Horan (1970) compared the OSO-4 spectrometer data with the simultaneous broad-band data for solar flares. He found that the temperatures based on line intensity ratios were not consistent with those based on the continuum. This is in part because of the rapid changes in the flare temperature and emission measure during the 14 minute time interval required to complete the spectrometer scan. Doschek (Chubb, 1972) attempted to compare the predicted continuum flux from the time history of the flare temperature and emission measure as determined by the broad-band data with the observed continuum flux at different wavelengths in the LiF crystal spectrometer data (1 - 3.8 Å). He found that the agreement between the predicted and the observed flux became worse at wavelengths less than 2.5 Å in the particular scan studied (Chubb, 1972), and that there was no satisfactory agreement in other cases. Therefore Chapter V describes the third objective of this thesis, viz., a renewed attempt to compare the available simultaneous data with the aid of the experimentally determined instrumental correction parameters.

Chapter V will then describe the fourth objective of this thesis, viz., a study of the total energy emitted in the soft x-ray band during several flares of various areal importance observed by the broad-band detectors. Both as absolute amounts and as amounts relative to the total emission at other wavelengths, such values would serve as helpful guides for the construction of better flare models (Thomas, 1970).

Chapter VI will conclude this thesis with a summary and discussion of the results obtained.

CHAPTER II

THERMAL SOFT X-RAY EMISSION PROCESSES

II.1. INTRODUCTION

The wealth of solar emission data flowing from rockets and satellites has spurred theoretical investigations of the coronal plasma processes responsible for the radiation. Among the most important discoveries of the previous decade has been the realization of the importance ofdielectronic recombination (Burgess, 1965), in establishing the ion balance in the corona. The dielectronic recombination process consists of an electron recombining with an ion having at least one bound electron to form a doubly excited system which subsequently decays by line emission rather than by autoionization. Burgess showed that this method of recombination may be an order of magnitude more effective than the well-known two body radiative recombination. Before the importance of dielectronic recombination was realized, the coronal temperature determined on the basis of ionization equilibrium calculations were much lower than those determined by other methods such as Doppler line widths. The inclusion of dielectronic recombination ionization equilibrium calculations (Appendix A) removed this glaring discrepancy (Billings, 1966; Zirin, 1966).

This chapter will be devoted to a brief discussion of the important atomic processes that give rise to solar radiation in the soft x-ray *region (1 - 10 Å) and their dependence on the electron density* N_e *and the electron kinetic temperature* T *which characterize the coronal plasma*

Recent excellent reviews on the methods of determining these parameters in the coronal plasma are given by Gabriel and Jordan (1972), Walker (1972), Doschek (1972), and Gabriel (1972b).

The soft x-radiation comes from optically thin regions that constitute the solar corona. The ideally quiet corona is characterized by high kinetic temperatures ($\sim 10^6$ K) and low electron densities ($\sim 10^8$ cm^{-3}). However, the dominant radiation field corresponds to the photospheric radiation temperature of about 5800 K which is too weak to induce radiative transitions involving x-ray photons. Therefore the coronal material cannot be in local thermodynamic equilibrium. Hence the time-independent ionization equilibrium of all coronal elements will mainly be determined by the balance between electron impact ionization and radiative plus dielectronic recombination. Similarly, the excitation equilibrium of the bound levels in a coronal ion is determined by collisional excitation and radiative decay. In the theoretical treatment of collision processes discussed in this thesis it has been assumed that the electrons and positive ions each have Maxwellian velocity distributions corresponding to one kinetic temperature. The reason for making this assumption is that it provides a convenient starting point for the interpretation of the observed data.

The three important forms of solar emission in the soft x-ray region are:

(1) Free-free continuum (FF or thermal bremsstrahlung),

(2) Free-bound continuum (FB or radiative recombination),

(3) Bound-bound radiation (BB or line emission).

A quantitative analysis of these requires a knowledge of the coronal abundances of the elements and their ionization and excitation equilibrium distribution. A brief description of the methods used in these calculations is given in Appendix A. The coronal abundances adopted by different authors are given in Table II-1.

TABLE II-1

TYPICAL CORONAL ABUNDANCES (Scale: N(Hydrogen) = 1)

Element	Culhane (1969a)	Bame et al. (1970)	Tucker and Koren (1971)	Withbroe (1971)	Mewe (1972b)
He	2.0×10^{-1}	3.0×10^{-2}	2.0×10^{-1}	1.6×10^{-1}	2.0×10^{-1}
C	4.0×10^{-4}	-	5.0×10^{-4}	3.7×10^{-4}	4.0×10^{-4}
N	6.0×10^{-5}	-	6.3×10^{-5}	8.8×10^{-6}	6.0×10^{-5}
O	3.0×10^{-4}	2.0×10^{-4}	3.2×10^{-4}	4.4×10^{-4}	3.0×10^{-4}
Ne	4.0×10^{-5}	-	4.0×10^{-4}	2.6×10^{-5}	4.0×10^{-5}
Na	-	-	-	-	4.0×10^{-6}
Mg	3.0×10^{-5}	-	3.2×10^{-5}	3.1×10^{-5}	3.0×10^{-5}
Al	-	-	-	2.0×10^{-6}	2.0×10^{-6}
Si	5.0×10^{-5}	4.2×10^{-5}	5.0×10^{-5}	3.1×10^{-5}	5.0×10^{-5}
S	2.0×10^{-5}	-	2.0×10^{-5}	1.6×10^{-5}	2.0×10^{-5}
Ar	4.0×10^{-6}	-	-	3.0×10^{-6}	4.0×10^{-6}
K	-	-	-	-	1.0×10^{-7}
Ca	2.0×10^{-6}	-	2.0×10^{-6}	-	3.0×10^{-6}
Ti	-	-	-	-	1.0×10^{-7}
Cr	-	-	-	-	2.0×10^{-7}
Mn	-	-	-	-	1.0×10^{-7}
Fe	5.0×10^{-5}	3.4×10^{-5}	3.0×10^{-5}	3.1×10^{-5}	5.0×10^{-5}
Ni	-	-	5.0×10^{-6}	-	4.0×10^{-6}

II.2 FREE-FREE AND FREE-BOUND CONTINUUM RADIATION

Elwert (1954) carried out the first continuum calculations based on a simple hydrogenic approximation. Culhane (1969) has developed the most complete method of calculating these continua using the ionization equilibrium calculations by Jordan (1969, 1970).

The soft x-ray region 1 - 8 Å corresponds to 12 - 1.5 keV in energy, which is non-relativistic for electrons. At these non-relativistic energies the electron-electron bremsstrahlung is negligible and photon production occurs during Coulomb scatterings of electrons by protons and other ions. The main contributors to the FF flux in the solar corona are hydrogen and helium. The other elements make only a small contribution. The uncertainty in the abundance of helium by several factors (Table II-1) is the major cause of uncertainty in the FF flux.

The free-free (or bremsstrahlung) flux, of frequency ν from unit volume of plasma per second per unit frequency interval is given by

$$I = h\nu N_Z N_e \int \sigma(v) f(v)\, v\, dv \quad \mathrm{erg\ cm^{-3}\ s^{-1}\ Hz^{-1}} \qquad \text{(II.1a)}$$

where N_Z is the number of ions of nuclear charge Z and N_e is the number of electrons per unit volume, $\sigma(v)d\nu$ is the cross section for the production of a photon frequency between ν and $\nu + d\nu$ by an electron of velocity v, f(v) is the Maxwellian velocity distribution and h is Planck's constant. After substituting for $\sigma(v)$ and f(v) and integrating, equation (II.1a) becomes

$$I = \frac{2^5 \pi e^6}{3^{1.5} m^2 c^3} \left(\frac{2\pi m}{kT} \right)^{\frac{1}{2}} N_e N_Z Z^2 g \exp(-h\nu/kT) \qquad \text{(II.1b)}$$

where e and m are the charge and mass of the electron respectively, c is the velocity of light, g is the Gaunt factor and T is the electron temperature. Brussard and Van de Hulst (1962) have discussed the accuracy of various methods to calculate the bremsstrahlung flux (referred to as the free-free flux in astrophysical literature) from a non-relativistic Maxwellian plasma. Culhane (1969a) showed on the basis of their paper that the FF flux from a unit volume of the coronal plasma at the distance of the earth is given by

$$F(FF,\lambda,T) = 7.15 \times 10^{-50}\ N_H\ N_e\ T_6^{-\frac{1}{2}}\ \lambda^{-2}\ \exp(-144/\lambda\, T_6\ )\ d\lambda\ .$$
$$\cdot \sum_Z (N_Z\ /N_H)\ Z^2\ g(Z,T,c/\lambda) \quad \mathrm{erg\ cm^{-2} s^{-1}\ \mathring{A}^{-1}/cm^3} \qquad (II.2)$$

Here N_H is the number density of hydrogen atoms, T_6 is the temperature (in 10^6 K), $g(Z,T,c/\lambda)$ is the temperature average of the free-free Gaunt factor tabulated by Karzas and Latter (1961), λ is the wavelength (Å), and the other quantities are defined in equation (II.1a).

The other important continuum process is radiative recombination (also known as free-bound process) of electrons with ions. If an electron with energy E_e recombines with an ion Z having an ionic charge z (number of electrons ionized + 1) and in the state n, then the emitted photon has an energy $h\nu = E_e + I(Z,z,n)$, where $I(Z,z,n)$ is the ionization potential of the particular level. Since the free electron energy is continuous, there results a recombination continuum with edges at the $I(Z,z,n)$ of each level. The calculation of FB flux, therefore, involves a summation over all the individual levels concerned. Since the recombination cross section has a strong dependence on the ionic charge ($\propto z^4$; Elwert, 1954), at high temperatures most of the recombination is due to the capture of electrons by almost completely ionized atoms of O, Ne, Mg, Fe, etc. At lower temperatures, where these elements are in lower stages of ionization, most of the recombination is due to electron captures by the more abundant elements hydrogen and helium (for cosmic abundances; Tucker, 1966). Thus the FB flux tends to dominate the x-ray continuum at lower coronal temperatures. At high temperatures (as in flares) the FF flux dominates the continuum.

Culhane's expression for the FB flux from a unit volume of the coronal plasma at the distance of the earth is

$$F(FB,\lambda,T) = 6.01 \times 10^{-53}\, N_H\, N_e\, T_6^{-1.5}\, \lambda^{-2} \exp(-144/\lambda T_6)$$

$$\cdot \sum_Z (N_Z/N_H) \sum_i (N_{i+1}/N_Z) \sum_{n=n_0}^{\infty} G_n \quad \text{erg cm}^{-5}\ \text{s}^{-1}\ \text{Å}^{-1} \qquad \text{(II.3)}$$

where $$G_n = \rho_n X_{i,n}^2\ g(Z,n,c/\lambda)\ n^{-1} \exp\left[0.012\, X_{i,n} / T_6\right] \qquad \text{(II.4)}$$

Here ρ_n represents the number of vacancies in the nth shell of the ion which can accept a captured electron, $X_{i,n}$ is the ionization potential (in eV) of an electron in the nth shell of an ion of ionization stage i and $g(Z,n,c/\lambda)$ is the free-bound Gaunt factor; N_{i+1}/N_Z is the fractional abundance of the element in the (i+1)th stage of ionization which can be obtained from Jordan's calculations (1969, 1970).

Horan (1970) has described a convenient summation procedure. Tucker and Koren (1971) have tabulated 64 terms consisting of the five or six lowest levels of the more abundant ions and one or two lowest levels for the less abundant ions that contribute to the summation, as a function of λ and T. They have shown that at a given temperature less than ten of the above mentioned terms are effective.

Considering the tediousness of the summation for the FB flux, Culhane and Acton (1970) developed an empirical analytical expression which could be readily used to calculate the FF and FB fluxes in the soft x-ray region. This was done by the use of an approximation for the Gaunt factors and an average value of Z^2. The combined photon flux due to an emission measure S (cm^{-3}) of the plasma at earth is given by

$$N(FF+FB,E,T) = 3.6 \times 10^{-39}\, \overline{Z^2}\, T^{-0.5}\, E^{-1} \exp(-E/kT)$$

$$\cdot \left(g(E,T)+f(E,T) \right) S \quad \text{photons cm}^{-2}\ \text{s}^{-1}\ \text{eV}^{-1}, \qquad \text{(II.5)}$$

where T is the temperature in degrees Kelvin, E is the photon energy in eV, $\bar{g}(E,T)$ and $f(E,T)$ are the approximate expressions for the FF and FB Gaunt factors given by

$$\bar{g}(E,T) = (E/kT)^{-0.3} , \qquad \text{(II.6)}$$

and

$$f(E,T) = \bar{g}(E,T) \left[(88000.0\ E^{-1})^{(kT/3000.0)} - 1 \right]^{-1} \qquad \text{(II.7)}$$

respectively. Here k is the Boltzmann's constant (eV/K), $\overline{Z^2} = 1.6$ and $S = \int N_e^2\, dV$ (cm^{-3}). In the usual astrophysical units equation (II.5) is rearranged into

$$N(FF+FB, \lambda ,T) = 1.3 \times 10^{-42}\ T_6^{-0.2}\ \lambda^{-0.7} \exp(-144/ \lambda\, T_6) \cdot \left[1 - (7.1\lambda)^{-(T_6/35.1)}\right]^{-1} . S$$

$$\text{photons cm}^{-2}\ \text{s}^{-1}\ \text{Å}^{-1} \qquad \text{(II.8)}$$

where T_6 is the temperature in 10^6 K and λ is the wavelength in Å. The photon flux can be converted to the corresponding energy flux as follows:

$$E(FF+FB, \lambda ,T) = N(FF+FB, \lambda ,T) \times 1.9875 \times 10^{-8} / \lambda$$

$$\text{ergs cm}^{-2}\ \text{s}^{-1}\ \text{Å}^{-1} . \qquad \text{(II.9)}$$

According to Culhane and Acton (1970) this equation is valid for photons in the energy interval 1.5 - 15 KeV (8.3 - 0.83 A) for the temperature range 4 - 20 x 10^6 K; it agrees with the sum of equations (II.2) and (II.3) to better than 15 per cent.

Figure II-1 shows the photon flux calculated from equation (II.8) for selected wavelengths as a function of the temperature due to an emission measure S = 10^{50} cm^{-3}. It shows that as the wavelength of the photons decreases the photon flux becomes more sensitive to the temperature.

In theoretical calculations a quantity that is convenient for computation is the flux per unit emission measure (Horan, 1970) given by

$$C(FF+FB, \lambda ,T) = E(FF+FB, \lambda ,T)/S \qquad \text{ergs cm s}^{-1}\ \text{Å}^{-1} , \qquad \text{(II.10)}$$

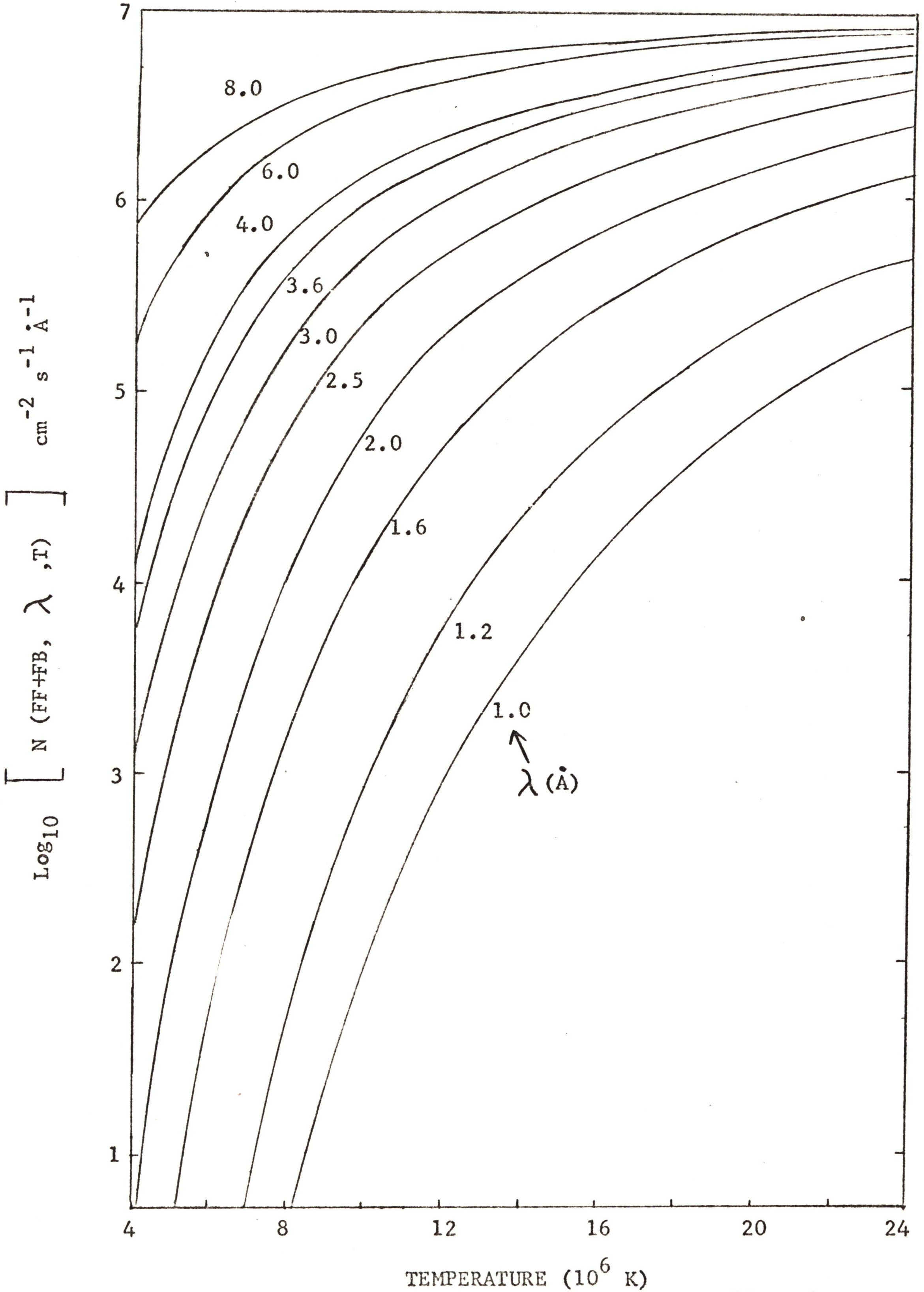

Figure II-1. Photon flux for an emission measure of 10^{50} cm^{-3} at earth. Wavelengths are indicated for each curve.

where E(FF+FB, λ ,T) is given by the equation (II.9). Equation (II.8) can be used to compute the photon flux per unit emission measure.

Multiplication of equations (II.8) and (II.9) by the factor 4π (1 astronomical unit)^2 gives the flux emitted by the coronal plasma in all directions.

II.3 LINE EMISSION

The major bound-bound processes that generate the line spectrum are:

(1) Electron impact excitation and radiative decay,

(2) Dielectronic recombination, and

(3) Inner-shell electronic excitation.

Most of the lines in the soft x-ray region are due to H- and He-like ions of coronal elements. Transitions and wavelengths of lines are given in Table IV-4. The luminosity L (erg s^{-1}) of a plasma radiating in a spectral line resulting from a transition u → ℓ between an upper level u and a lower level ℓ is given by

$$L = A_{u\ell}\, E_{u\ell} \int N_u \, dV \qquad \text{erg s}^{-1} , \qquad \text{(II.11)}$$

where the integral is taken over the volume of the emitting plasma. In this equation, $A_{u\ell}$ is the transition rate (the Einstein coefficient) for the spontaneous emission for the transition, $E_{u\ell}$ is the energy of the transition, and N_u is the number of ions (cm^{-3}) in the initial level u. N_u is given (equation A.11) by

$$N_u = N_e \, N_g \, C_{gu} \, / \sum_{\ell} A_{u\ell} , \qquad \text{(II.12)}$$

where g refers to the ground state of the ion under consideration and C_{gu} is the collisional excitation rate (equation A.12). Assuming that the density is uniform throughout the emitting volume of the plasma, the integral sign in the equation (II.11) can be removed. Then the luminosity per unit volume will be given by

$$P_u = N_e N_{Z,z} C_{gu} B_{u\ell} E_{u\ell} \qquad \text{ergs cm}^{-3} \text{ s}^{-1}, \qquad (II.13)$$

where $B_{u\ell} = A_{u\ell} \Big/ \sum_{\ell} A_{u\ell}$ is the radiative branching ratio for the particular transition and $N_{Z,z}$ is the number of ions of element Z (cm^{-3}) in the ionization stage z. For coronal conditions $N_{Z,z} = N_g$ to within two percent and therefore this has been used in the equation (II.13). Mewe (1972b) has listed the value of $B_{u\ell}$ for a large number of transitions. It is nearly unity for most of the transitions of importance in the soft x-ray region. In such cases the term $B_{u\ell}$ may be omitted in the above equation.

Many authors (e.g., Landini and Monsignori Fossi, 1970; Tucker and Koren, 1971; Mewe, 1972b) have tabulated the predicted intensities of expected lines; but the values do not agree with one another. The differences between the published tabulations arise from the following factors:

(1) Uncertainties in the coronal abundances of elements (Table II-1),

(2) Differences in the methods of computing Maxwellian averages of collision cross sections (Appendix A), and

(3) Theoretical uncertainties in the atomic parameters such as the oscillator strength.

In terms of the quantities used in equation (II.13) the luminosity of the emitting plasma can be written as

$$L = N_e N_H \left(\frac{N_Z}{N_H}\right) \left(\frac{N_{Z,z}}{N_Z}\right) C_{gu} B_{u\ell} E_{u\ell} V \qquad \text{ergs s}^{-1} \qquad (II.14)$$

where V is the volume of the plasma, and N_H is the number of hydrogen atoms (cm^{-3}). The relative abundance of the element with respect to hydrogen

N_Z / N_H, is given in Table II-1, and the relative population of the ion (Z,z) with respect to its total population for several elements is given by Jordan (1969,1970). This equation can be used to compute the ratio of intensities of any two lines emitted by the same coronal region. It can be shown from the equation (II.14) that the ratio of the Lyman-α line intensity $I(L\alpha)$ of a hydrogenic ion to the resonance line intensity I(He-R) of the helium-like ion of the same element is given by

$$\frac{I(L\alpha)}{I(\text{He-R})} = \frac{f(L\alpha)}{f(\text{He-R})} \; \frac{A(\text{H-like},T)}{A(\text{He-like},T)} \; \exp(-\Delta E/kT) \qquad \text{(II.15)}$$

where $f(L\alpha)$ is the oscillator strength of the Lyman-α line and f(He-R) is that of the He-like resonance line, $\Delta E = E(L\alpha) - E(\text{He-R})$, A(H-like,T) and A(He-like,T) are the relative populations of the hydrogenic and helium-like ionization stages of the element respectively (given by the relevant ratio $N_{Z,z} / N_Z$). Since $\Delta E/kT$ is not large, the temperature dependent ratio of the relative ion populations largely controls the intensity ratio. This ratio has been used to classify solar flares on the basis of the observed line intensity ratios (Chubb, 1972).

The case of helium-like ion resonance, intercombination and forbidden lines that dominate the soft x-ray spectra is very interesting. Their theoretical investigation was prompted by the observation of the single line at 22.09 Å on the long wavelength side of the O VII resonance line in the soft x-ray spectrum from active regions (Fritz, et al., 1967; Rugge and Walker, 1968; Jones, et al., 1968) and was comparable with the resonance line intensity. However, this line was known to be quite weak in laboratory spectra. Gabriel and Jordan (1969a) made a theoretical investigation of energy levels using the multi-configuration Hartree-Fock program developed by Froese (1969) and suggested that this line was the unexpected forbidden transition $1s^2\ ^1S - 1s\ 2s\ ^3S$ in O VII. This has been confirmed by further theoretical calculation and observation of similar transitions in other coronal ions (Gabriel, 1972b).

The term structure of the two-electron ions is characterized by the high ionization potential of the 1s electrons as well as the relatively high excitation potential of the first excited n = 2 terms. The excited configurations of the type $1s\ 2\ell$ give singlet terms $2\ ^1L$, and triplet terms $2\ ^3L$. These excited states are all grouped relatively close to the ionization limit so that it is not possible to observe ratios of intensities from spectral lines having very different excitation potentials. In addition, the helium-like ion abundance is not as sensitive to temperature as the relative abundances of the lower ion stages (Appendix A). Therefore these ions are not a suitable choice for measurements of electron temperature. However the existence of the three long lived terms $2\ ^3S$, $2\ ^1S$ and $2\ ^3P$ gives rise to some complex variations of intensities with electron density. Table II-2 lists the important transitions and the Z dependence of their rates (Mewe, 1972a; Gabriel and Jordan, 1972). This makes it

TABLE II-2

Z DEPENDENCE OF TRANSITION RATES IN He-LIKE IONS

Transition	Type	Factor
$1\ ^1S - 2\ ^3S$	Relativistic Magnetic Dipole	Z^{10}
$1\ ^1S - 2\ ^1S$	2-photon Electric Dipole	Z^6
$1\ ^1S - 2\ ^3P_1$	Spin-orbit Interaction	Z^9
$1\ ^1S - 2\ ^3P_2$	Magnetic Quadrupole	Z^8
$1\ ^1S - 2\ ^1P$	Electric Dipole ($\Delta n \neq 0$)	Z^4
$2\ ^1S - 2\ ^1P$	Electric Dipole ($\Delta n = 0$)	Z

possible to estimate electron densities from the He-like line intensities. It can be seen that the forbidden transitions become increasingly important for heavier elements. The theory of line intensity ratios has been worked out by Gabriel and Jordan (1969b, 1972), Freeman et al., (1971), Blumenthal et al., (1972) and Mewe (1972a). It will be briefly treated here.

Gabriel and Jordan solved the equations of statistical equilibrium for the ground state and the six n = 2 levels that arise from 1s 2s and 1s 2p configurations. The two useful line intensity ratios considered are:

$$R = \frac{I(2\,{}^3S \rightarrow 1\,{}^1S)}{I(2\,{}^3P_1 \rightarrow 1\,{}^1S) + I(2\,{}^3P_2 \rightarrow 1\,{}^1S)} , \tag{II.16}$$

$$G = \frac{I(2\,{}^3S \rightarrow 1\,{}^1S) + I(2\,{}^3P_2 \rightarrow 1\,{}^1S) + I(2\,{}^3P_1 \rightarrow 1\,{}^1S)}{I(2\,{}^1P \rightarrow 1\,{}^1S)} , \tag{II.17}$$

where the levels are shown in Figure II-2. The ratio R of the relativistic magnetic dipole line to the intercombination line intensities (equation II.16) is given by

$$R = R_o \left[1 + \left[N_e\, C(2\,{}^3S \rightarrow 2\,{}^3P) + \phi \right] (1 + F) \Big/ A(2\,{}^3S \rightarrow 1\,{}^1S) \right]^{-1} , \tag{II.18}$$

$$\text{where } R_o = (1 + F) \Big/ B - 1 , \tag{II.19}$$

$$F = C(1\,{}^1S \rightarrow 2\,{}^3S) \Big/ C(1\,{}^1S \rightarrow 2\,{}^3P), \tag{II.20}$$

and B is the radiative branching ratio for the two intercombination transitions to the ground state (Mewe, 1972a). The photo-excitation rate ϕ for $2\,{}^3S \rightarrow 2\,{}^3P$ is important only for C V in the sun and is negligible for the heavier ions considered in this thesis.

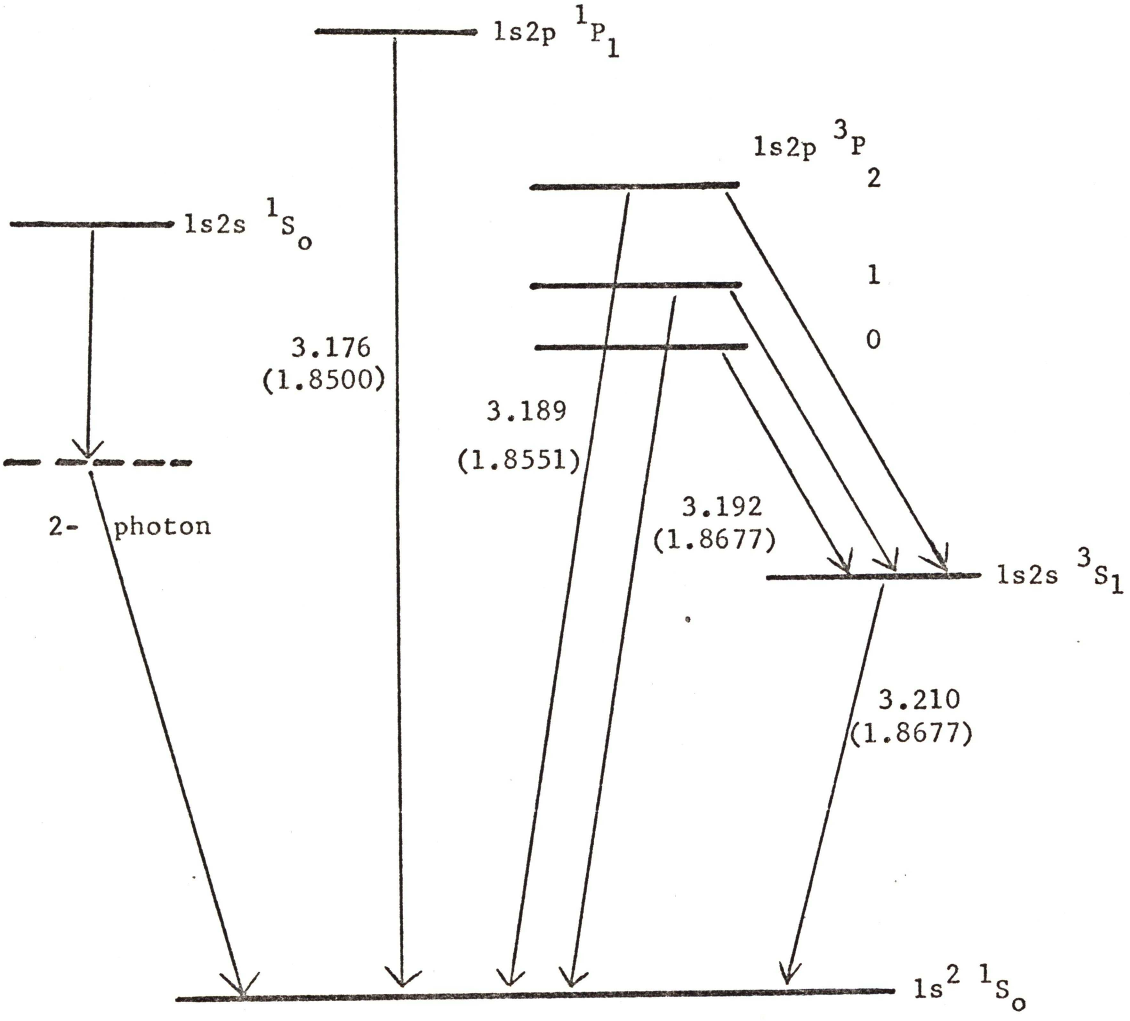

Figure II-2. Grotrian Diagram for a helium-like ion such as Si XIII, Ca XIX, or Fe XXV. Wavelengths (all in Å) shown are those of transitions in calcium (and iron in brackets). The nature of the transitions is explained in Table II-2.

At low N_e ($\sim 10^8$ cm^{-3}) all the excited states are primarily populated from the ground state by collisional excitation, and these decay directly or cascade to the ground by line emission. In the limit of low density the ratio R reduces to R_o (equation II.19) which is independent of N_e and T. Thus, for low N_e, the ratio R is largely independent of N_e. However, for N_e in the range given by $N_e C(2\ ^3S \rightarrow 2\ ^3P) \approx A(2\ ^3S \rightarrow 1\ ^1S)$, R decreases with increasing N_e, approaching zero asymptotically in the limit of large N_e. Then the least value of N_e at which R becomes senistive can be found by assuming that the observational precision in R is 10%, so that $R = 0.9\ R_o$. Now equation (II.18) gives the low density limiting value N_e' as

$$N_e' = \frac{1}{9} \frac{A(2\ ^3S \rightarrow 1\ ^1S)}{(1 + F)\ C(2\ ^3S \rightarrow 2\ ^3P)} . \qquad \text{(II.21)}$$

The ratio G of the intercombination plus forbidden line to resonance line intensities (equation II.17) is also found to be independent of N_e in the low density limit. While many reported observations conclude that G has a constant value of ~ 1.1, Doschek (1972) and Gabriel (1972b) point out that those analyses (ibid.) have neglected the contribution from the dielectronic recombination satellite lines (see section II.4).

Now, as N_e increases from N_e', collisions $2\ ^3S \rightarrow 2\ ^3P$ first depopulate $2\ ^3S$, decreasing the $1\ ^1S - 2\ ^3S$ line intensity. Then at intermediate densities, $2\ ^1S \rightarrow 2\ ^1P$ collisions depopulate the $2\ ^1S$ term thereby increasing the resonance line intensity. This process is important only for laboratory plasmas (Gabriel, 1972b). The critical density for the transition between these two conditions is given by

$$N_e'' \approx A(2\ ^1S \rightarrow 1\ ^1S)\ /\ C(2\ ^1S \rightarrow 2\ ^1P) \qquad \text{(II.22)}$$

The relative intensities of the intercombination and forbidden lines with respect to that of the resonance line in the low density case ($< N_e'$), N_e', N_e'' and the temperature of maximum helium-like resonance line emission, T_m, are given in Table II-3 (Gabriel, 1972b).

TABLE II-3

RELATIVE INTENSITIES OF He-LIKE LINES AND ELECTRON DENSITIES*

Ion	$T_m \times 10^6$ K	$^1S_o - ^3P_1$	$^1S_o - ^3P_2$	$^1S_o - ^3S_1$	N_e' (cm^{-3})	N_e'' (cm^{-3})
Mg	6.0	0.25	0.03	0.82	7×10^{11}	3×10^{15}
Si	9.3	0.25	0.07	0.70	4×10^{12}	2×10^{16}
S	13.6	0.25	0.13	0.64	2×10^{13}	1×10^{17}
Ar	18.9	0.25	0.19	0.58	7×10^{13}	2×10^{17}
Ca	25.4	0.25	0.26	0.51	2×10^{14}	6×10^{17}
Fe	52.8	0.25	0.35	0.41	5×10^{15}	7×10^{18}

* Valid for $G = 1.1$ and $F = 0.45$ (see Gabriel, 1972b).

It can be seen from the above table that, as Z increases N_e' also increases and is of the order of $10^{14} - 10^{15}$ (cm^{-3}) for ions of Ca and Fe. Such values of N_e are improbable even in the most intense flares. Therefore in ordinary situations one would expect the ratio R (equation II-18) to be independent of N_e for at least the heavier ions in Table II-3. The reported observational results suggest that this is indeed the case (see Walker, 1972; Doschek, 1972; Gabriel, 1972b).

II.4 DIELECTRONIC RECOMBINATION

The dielectronic recombination process (explained below and in Appendix A) leads to an enhancement of the intensity of the resonance line and the production of a large number of satellite lines. The satellite lines situated on the long-wavelength side of helium-like resonance lines were first reported from laboratory spark sources by Edlén and Tyrén (1939). Their theoretical interpretation came only after the observation of an intense satellite structure near the Fe XXV resonance line at 1.85 A by Neupert et al., (1967), and Meekins et al., (1968, 1970) in the soft x-ray spectra obtained by the OSO-3 and OSO-4 satellites. They suggested that these lines are the inner shell 1s - 2p transitions from Fe XXIV and its lower ionization stages. Walker and Rugge (1971), Doschek (1972) and others have also drawn attention to similar satellite features near hydrogen-like and helium-like lines of other coronal ions.

Gabriel and Paget (1972) showed that the satellite lines of helium-like ion lines are produced by dielectronic recombination of those ions and also by inner shell excitation of the lithium-like ions. They showed by experimental analysis (of laboratory plasmas) that dielectronic recombination was the dominant mechanism. Following their suggestion, Gabriel (1972a, 1972b) worked out the wavelengths and expected intensities of the lithium-like satellite lines due to both mechanisms mentioned above. These lines arise in the following transitions:

$$\begin{array}{llll}
1s^2\ 2s\ {}^2S & \text{--}\ 1s\ 2p({}^1P)\ 2s\ {}^2P^o & (A) & \\
 & \text{--}\ 1s\ 2p({}^3P)\ 2s\ {}^2P^o & (A) & \\
 & \text{--}\ \qquad\qquad\quad {}^4P^o & - & \\
1s^2\ 2p\ {}^2P^o & \text{--}\ 1s\ 2p^2\ {}^4P & - & \\
 & \text{--}\ \qquad\quad {}^2P & - & (II.23) \\
 & \text{--}\ \qquad\quad {}^2D & (A) & \\
 & \text{--}\ \qquad\quad {}^2S & (A) & \\
 & \text{--}\ 1s\ 2s^2\ {}^2S & (A) &
\end{array}$$

where those marked (A) have permitted autoionizing transitions in LS coupling. As an example, consider the energy level diagram for a helium-like and a lithium-like atom in Figure II-3.

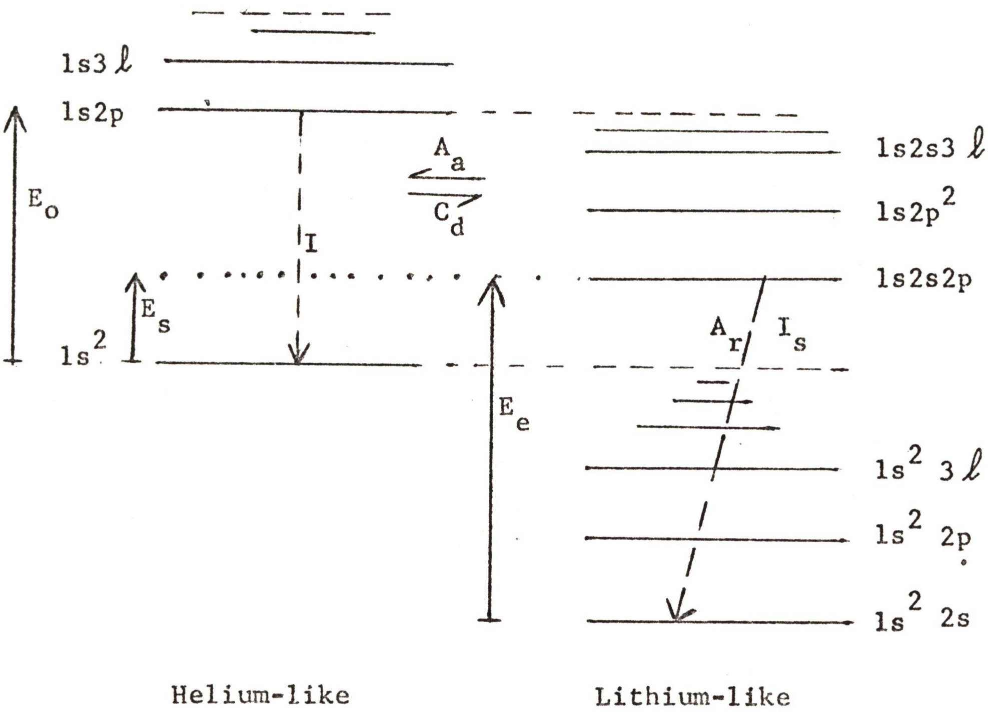

Figure II-3. An example of autoionization and dielectronic recombination between helium-like and lithium-like ions.

In this diagram, the satellite initial level 1s2s2p, well above the ionization limit of the Li-like ion, can be produced by the process,

$$1s^2\ {}^1S + \epsilon\ p\ {}^2P^o \rightleftharpoons 1s\ 2s\ 2p\ {}^2P^o ,$$

where the free electron has a kinetic energy ϵ. The forward process is a dielectronic recombination of the He-like ion with a rate C_d ($cm^3\ s^{-1}$), whereas the reverse process is an autoionization of the satellite level with a rate A_a (s^{-1}). This level can also spontaneously decay (to the ground level of the Li-like ion considered) with a rate A_r and emit a satellite line of energy E_e as shown. This energy may be quite close to the energy E_o of He-like resonance line. Then the photon intensity of the satellite line, I_s, is given (Gabriel, 1972a) by

$$I_s = N_e N_{Z,z}(\text{He-like})\ C_d\ A_r\ (A_a + \sum A_r)^{-1}, \qquad (\text{II}.24)$$

where $N_{Z,z}$(He-like) is the number of He-like ions of the element per unit volume, $A_r\ (A_a + \sum A_r)^{-1}$ is the radiative branching ratio for the satellite transition and C_d and A_a are related to each other through the principle of detailed balance (Gabriel and Paget, 1972). If I is the photon intensity of the He-like resonance line, then

$$I = N_e N_{Z,z}(\text{He-like})\ C_{\ell u}\ (1 + \alpha), \qquad (\text{II}.25)$$

where $C_{\ell u}$ is the collisional excitation rate (equation A.16) and $\alpha = D/C_{\ell u}$, the ratio of the contribution to the resonance line intensity by all the dielectronic recombination satellites which are indistinguishable in wavelength (given by D) and $C_{\ell u}$. Gabriel (1972b) uses the equation given (see Appendix A) by Burgess (1965) but applies a correction of not more than 10 per cent based on Shore's (1969) more detailed treatment of the process of dielectronic recombination.

The ratio of dielectronic satellite to resonance line intensity, I_s/I, can be found from equations (II.24) and (II.25). Gabriel (1972b) expresses this ratio as a function of the characteristic temperature T_m (given in Table II-3) at which the helium-like ion resonance line has its maximum emission in an isothermal steady plasma, and a multiplying factor to obtain the ratio at any other temperature T. Further discussion is given in Gabriel's papers (1972a, 1972b).

The wavelengths of helium-like ion lines and their stronger dielectronic satellites are given in Table II-4 for selected ions. A complete list of the 22 Li-like satellites for all the coronal ions up to copper is given in Gabriel (1972b). The key letters of the transitions given here are explained in Table IV-4 . The Li-like satellites can have as much as 30 - 40 per cent of the intensity of the ion resonance line for heavier He-like ions such as Ca XIX and Fe XXV.

TABLE II-4

WAVELENGTHS OF He-LIKE ION LINES AND THEIR Li-LIKE SATELLITES

Key Letter	Elements				
	Si	S	Ar	Ca	Fe
He - R	6.647 Å	5.038 Å	3.948 Å	3.176 Å	1.8500 Å
He - I2	6.685	5.063	3.965	3.189	1.8551
He - I1	6.688	5.066	3.969	3.192	1.8591
He - F	6.739	5.101	3.993	3.210	1.8677
Li - a	6.726	5.090	3.985	3.203	1.8618
Li - d	6.726	5.090	3.985	3.203	1.8624
Li - e	6.782	5.128	4.012	3.223	1.8721
Li - j	6.744	5.103	3.995	3.210	1.8657
Li - k	6.741	5.100	3.991	3.207	1.8631
Li - m	6.682	5.062	3.966	3.189	1.8562
Li - q	6.718	5.085	3.981	3.200	1.8604
Li - r	6.720	5.087	3.983	3.202	1.8635

II.5 INNER-SHELL EXCITATION

Inner-shell excitation takes place by the left to right process of transitions given in equation (II.23) for the lithium-like ions. The excited states then undergo spontaneous transition to the ground states, emitting lines with the same wavelength as the dielectronic satellites, or some of the excited states may autoionize . The intensity I_s' of the inner-shell excited satellites will be proportional to the lithium-like ion population and is given by

$$I_s' = N_e N_{Z,z}(\text{Li-like})\, C' A_r (A_a + \sum A_r)^{-1} \qquad \text{(II.26)}$$

which is similar to equation (II.25) except that the inner-shell excitation rate C' is calculated by the method described by Gabriel (1972b). Now the ratio of the lithium-like satellite to the helium-like resonance line is given by the ratio of equations (II.26) and (II.25). However, I'_s/I is now also a function of lithium-like to helium-like ion abundance ratio which increases with Z at T_m. This ion abundance ratio is a function of T and the departure from ionization equilibrium. If T_Z is the ionization temperature at which the actual ratio is in ionization equilibrium, then $T_Z = T$ for ionization equilibrium in the plasma, $T_Z < T$ for transient ionizing conditions and $T_Z > T$ for transient recombination conditions.

The wavelengths given by Gabriel (1972b) have errors less than *±0.001 Å (± 0.0003 Å for iron). In most cases a resolution of this* order in an observed x-ray spectrum should be more than adequate to distinguish the He-like ion lines and the Li - like satellites (see Table II-4), although there are a few cases where it would be desirable to match Gabriel's degree of resolution in order to achieve an identification with certainty.

It is thus possible to determine the electron temperature and the relative distribution of ion stages. This, in turn, can determine whether the plasma is ionizing, or in steady state, or is recombining. Examples of this method are given by Gabriel (1972b).

Theoretical calculations of comparable accuracy are not yet available for He-like satellites of hydrogenic Lyman lines of ions, although crude calculations have been reported for a few satellites of the Mg XII line by Walker and Rugge (1971).

II.6 SUMMARY

This chapter deals with a review of the important atomic processes which are considered in published literature to be responsible for the thermal continuum (FF + FB) and line emission from the flare plasma.

The appropriate quantitative treatments developed by various authors have also been discussed. The main points are:

(1) The photon flux at earth (photons cm^{-2} sec^{-1} $Å^{-1}$) due to the thermal continuum emission can be calculated by using the simplified analytical expression (II.8). This expression will be used in Chapter V to predict the continuum spectrum between 1.0 and 3.8 Å.

(2) If the velocities of electrons and ions conform to a Maxwellian distribution, then electron collisional excitation and dielectronic recombination will be mainly responsible for the observed line intensities. Only in the case of heavy ions like calcium and iron, will the inner-shell excitation be an additional contributor to line intensities (of Li-like lines); in light ions (like silicon) this mechanism is of negligible importance.

CHAPTER III

DESCRIPTION OF OGO-4 AND OSO-4 EXPERIMENTS

III.1 THE NRL OGO-4 EXPERIMENT

The NRL broad-band detectors were conceived and developed by Kreplin (1961) to make a systematic study of solar soft x-rays continuously through orbiting spacecraft. The NASA's Orbital Geophysical Observatory-4 satellite (OGO-4, 1967-73A) which was launched on July 28, 1967, contained four broad-band ionization chamber detectors sensitive to 0.5 - 3 Å (referred to as the 0 - 3 Å detector), 1 - 8 Å, 8 - 20 Å and 44 - 60 Å bands of the x-ray spectrum, respectively. These detectors had no spatial resolution because they viewed the entire sun; but their time resolution was better than 5 seconds. The detector sensitive to the highest wavelength band ceased its operation in November 1967. The output current of these ionization chamber detectors are, in principle, proportional to the incident flux. Since the exact nature of the flux spectrum was unknown in 1961 (and is not precisely known even now), Kreplin assumed a gray-body spectrum (see below) with a colour temperature T_c of 10×10^6 K for the 0 - 3 Å band and of 2×10^6 K for the other bands. Then the detector currents were converted to an integral energy of flux by using the appropriate current-to-flux conversion constants at the above mentioned colour temperatures. The technical details of this experiment are described by Kreplin et al., (1969), Horan (1970, 1971), and by Dere et al., (1973), to which reference can be made. The physics of the experiments and Horan's analysis of the data from 0 - 3 Å and 1 - 8 Å detectors will be briefly described below.

III.2 PROCESSING OF THE OGO-4 BROAD-BAND DETECTOR DATA

The response of an ionization chamber to radiation of a given wavelength is determined by the detector window material and thickness and the gas used to fill the detector (Horan and Kreplin, 1972). The window completely absorbs low-energy radiation and provides a long-wavelength limit to the detector's sensitivity. The gas filling of the detector is transparent to high-energy radiation which provides a short-wavelength limit to the detector's sensitivity. The soft x-radiation which lies between these two wavelength limits will be only partially absorbed by the window material and that portion which penetrates the window will interact with the filling gas. The interaction between the radiation and the gas produces electron-ion pairs in the gas. The electrons and ions move, under the influence of an applied electric field, to the anode and cathode respectively, producing a current whose magnitude can be related to the energy flux incident upon the detector window.

Let $E(A, \lambda, T)$ represent the solar emission spectrum where A describes the mechanism involved (such as FF+FB or FF+FB+Line), λ is the wavelength and T is the temperature. Then the actual current generated per unit area in the broad-band detector is given by

$$I = e\,\omega \int_0^\infty E(A, \lambda, T)\ \epsilon(\lambda)\, d\lambda \qquad \text{amp. cm}^{-2} \qquad \text{(III.1)}$$

where e is the electronic charge, ω is the number of ion pairs produced in the gas per unit energy of the incident photon and $\epsilon(\lambda)$ is the efficiency of the detector. For actual calculations, the integration limits are determined by the range of wavelengths over which the detector's efficiency is non zero (see Horan, 1970 for details).

Since the exact nature of the solar emission spectrum $E(A, \lambda, T)$ is not known, Kreplin (1961) assumed a diluted black body spectrum (hence known as the gray body approximation and is denoted by GB wherever appropriate) given by,

$$E(GB, \lambda, T_c) = 2\pi hc^2 D(t) \lambda^{-5} \left[\exp(hc/k\lambda T_c) - 1\right]^{-1}, \qquad \text{(III.2)}$$

where h is Planck's constant, c is the speed of light, k is Boltzmann's constant, T_c is the colour temperature of the emitting region and D(t) is a time-dependent dilution factor which indicates the amount by which the solar emission intensity falls below that expected from a true black body radiation at the temperature T_c. The value of D(t) for any colour temperature T_c can be obtained by comparing the current I generated by solar soft x-rays with the calculated value of

$$I' = e\omega \int E(GB, \lambda, T_c)\, \epsilon(\lambda)\, d\lambda \quad \text{amp. cm}^{-2} . \qquad \text{(III.3)}$$

Since the solar spectrum over the entire soft x-ray region cannot be adequately approximated by a gray body spectrum for a single colour temperature, appropriate colour temperatures are selected for the spectral segment to which the detector is sensitive. Kreplin (1961) chose what have now become the standard values for all SOLRAD and OGO broad band detectors:

$T_c = 10 \times 10^6$ K for 0 - 3 A band

$T_c = 2 \times 10^6$ K for 1 - 8 A and 8 - 20 A bands

$T_c = 0.5 \times 10^6$ K for 44 - 60 A band

Using these values of temperatures the current to flux conversion constants have been calculated for each detector. They are defined by

$$K(GB, T_c) = \frac{\int E(GB, \lambda, T_c)\, d\lambda}{e\omega \int E(GB, \lambda, T_c)\, \epsilon(\lambda)\, d\lambda} , \qquad \text{(III.4)}$$

The values used in OGO-4 data processing are:

$$0 - 3\ \text{Å} : K_{03}(GB, 10 \times 10^6\ K) = 7.54 \times 10^8 \text{ erg s}^{-1} \text{ amp}^{-1}$$

$$1 - 8\ \text{Å} : K_{18}(GB, 2 \times 10^6\ K) = 2.62 \times 10^8 \text{ erg s}^{-1} \text{ amp}^{-1} .$$

.....(III.5)

Now the integral solar energy flux can be calculated from the appropriate detector current I by the equation

$$\phi\,(GB,T) = K(GB,T_c)\ I \qquad \text{erg cm}^{-2}\ \text{s}^{-1}, \qquad (III.6)$$

where $\phi\,(GB,T)$ is referred to as the gray body flux since Kreplin's gray body conversion constants have been used. This is done whether the flux is from a flaring sun or a non-flaring sun and facilitates automatic processing of the large amount of data produced by the broad band detectors.

The gray body fluxes defined by equation (III.6) are plotted against the Universal Time (UT) of observation by OGO-4 spacecraft. Typical data plots for five solar flares selected from data kindly supplied by Dr. Horan are shown in Figures III-1 to III-5, which show the time-history of the fluxes from 0 - 3 Å, 1 - 8 Å and 8 - 20 Å detectors (note that the ordinate scale for the 8 - 20 Å flux has been shifted as shown for the sake of clarity). The corresponding Hα patrol data for these flares are given in Table III-1 (Solar Geophysical Data bulletins, 1968).

TABLE III-1

Hα PATROL DATA FOR SELECTED FLARES

Figure No.	1967 Date	Begin (UT)	Max (UT)	End (UT)	Importance	Position on Sun
III-1	July 30	06 15	06 20	07 00	1b	N26 W29
III-2	Aug 02	00 43	00 48	01 02	1n	N26 W58
III-3	Oct 25	23 12	23 28	24 00	1b	N10 W28
III-4	Oct 26	06 08	06 14	06 40	1b	N10 W38
III-5	Nov 16	21 24	21 43	23 18	3b	N11 E33

It is seen that the time of maximum of the Hα flare observation coincides with the peak of the 0 - 3 Å flux. It is also clear from the plots that

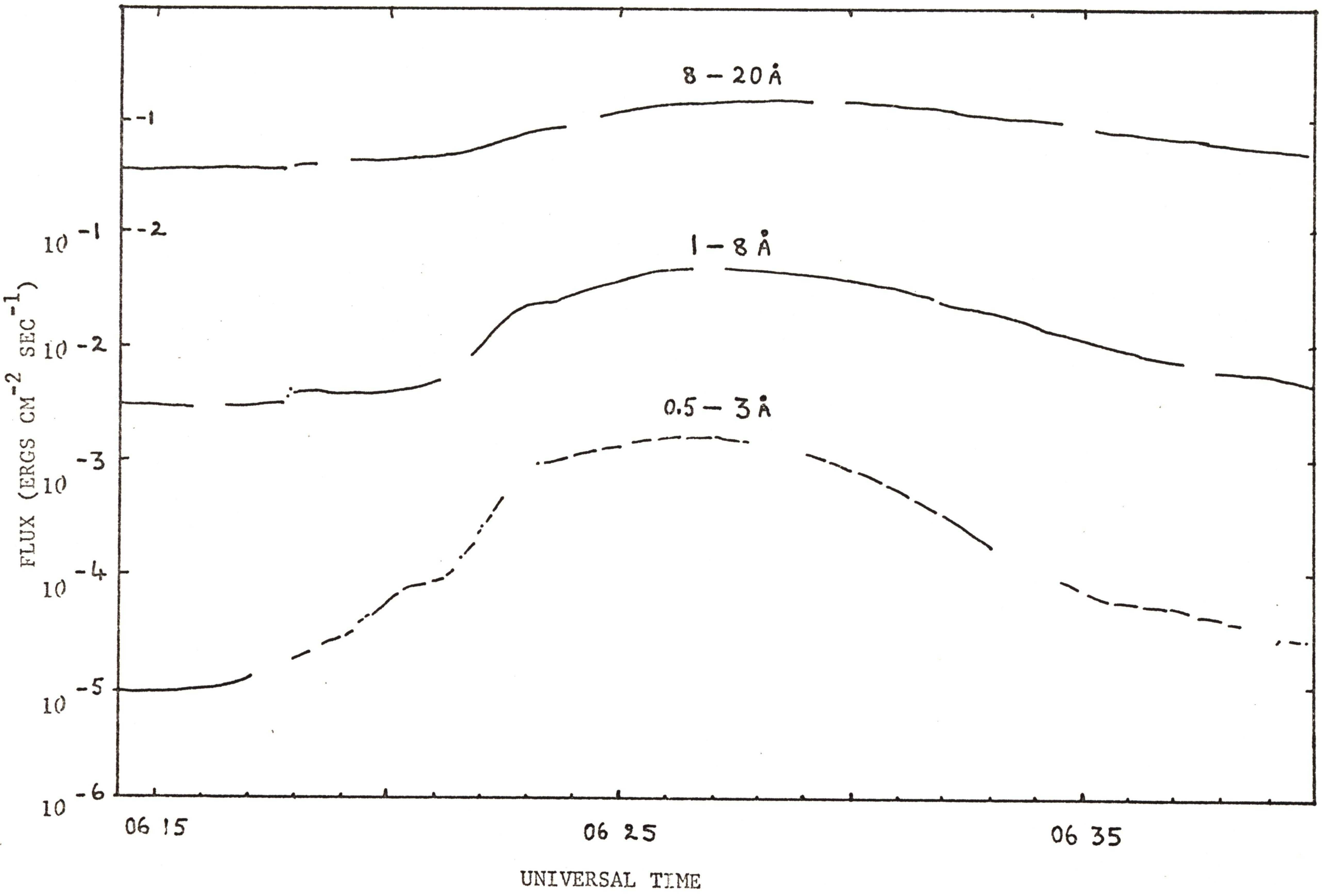

Figure III-1. OGO-4 broad band detector fluxes (gray body based) for class 1b flare of July 30, 1967 during the time shown. The wavelength bands of detectors are indicated on the graphs. Note the shift in the scale of 8 - 20A flux.

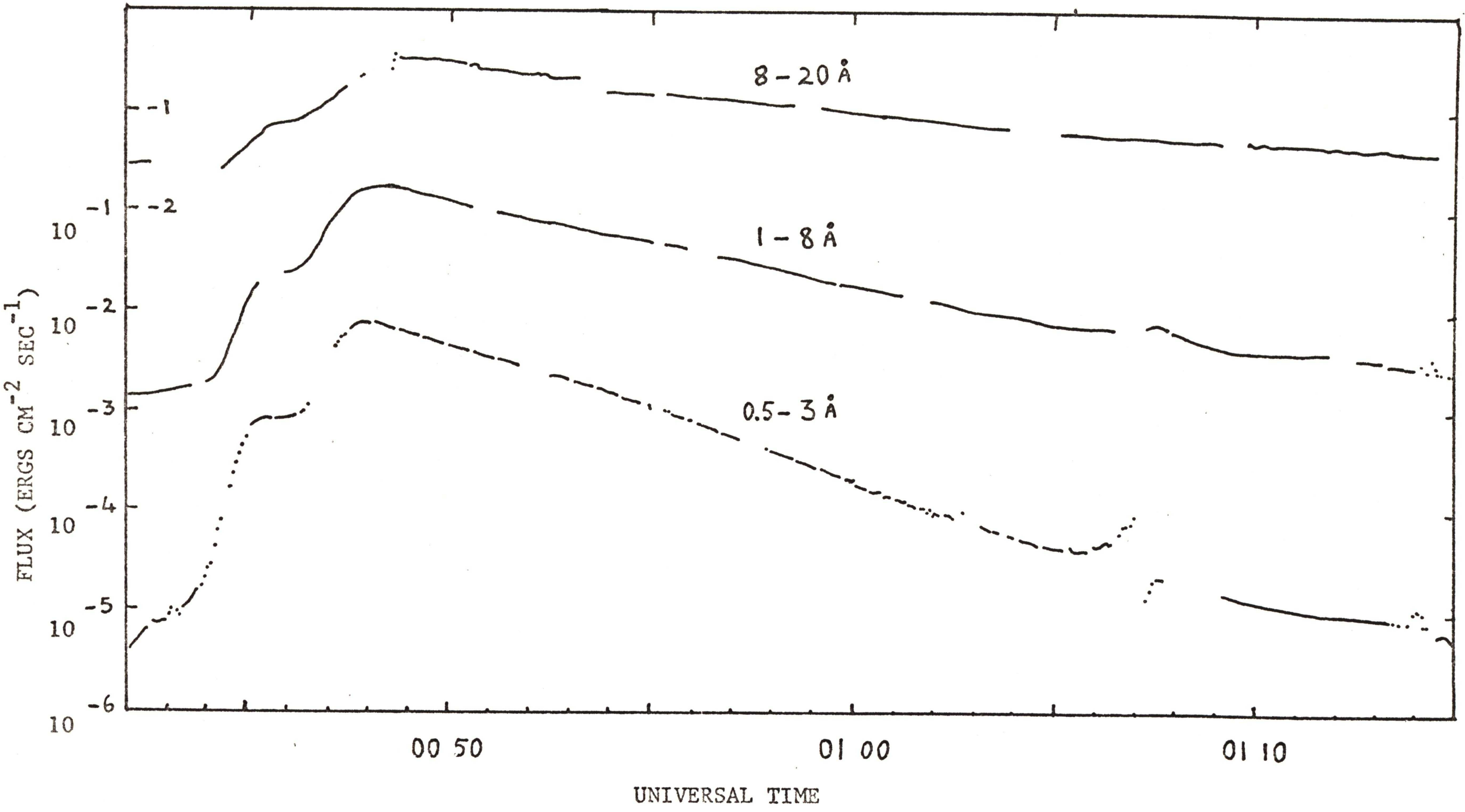

Figure III-2. OGO-4 broad band detector fluxes (gray body based) for class 1n flare of August 2, 1967 during the time shown. The wavelength bands of detectors are indicated on the graphs. Note the shift in the scale of 8 - 20 A flux.

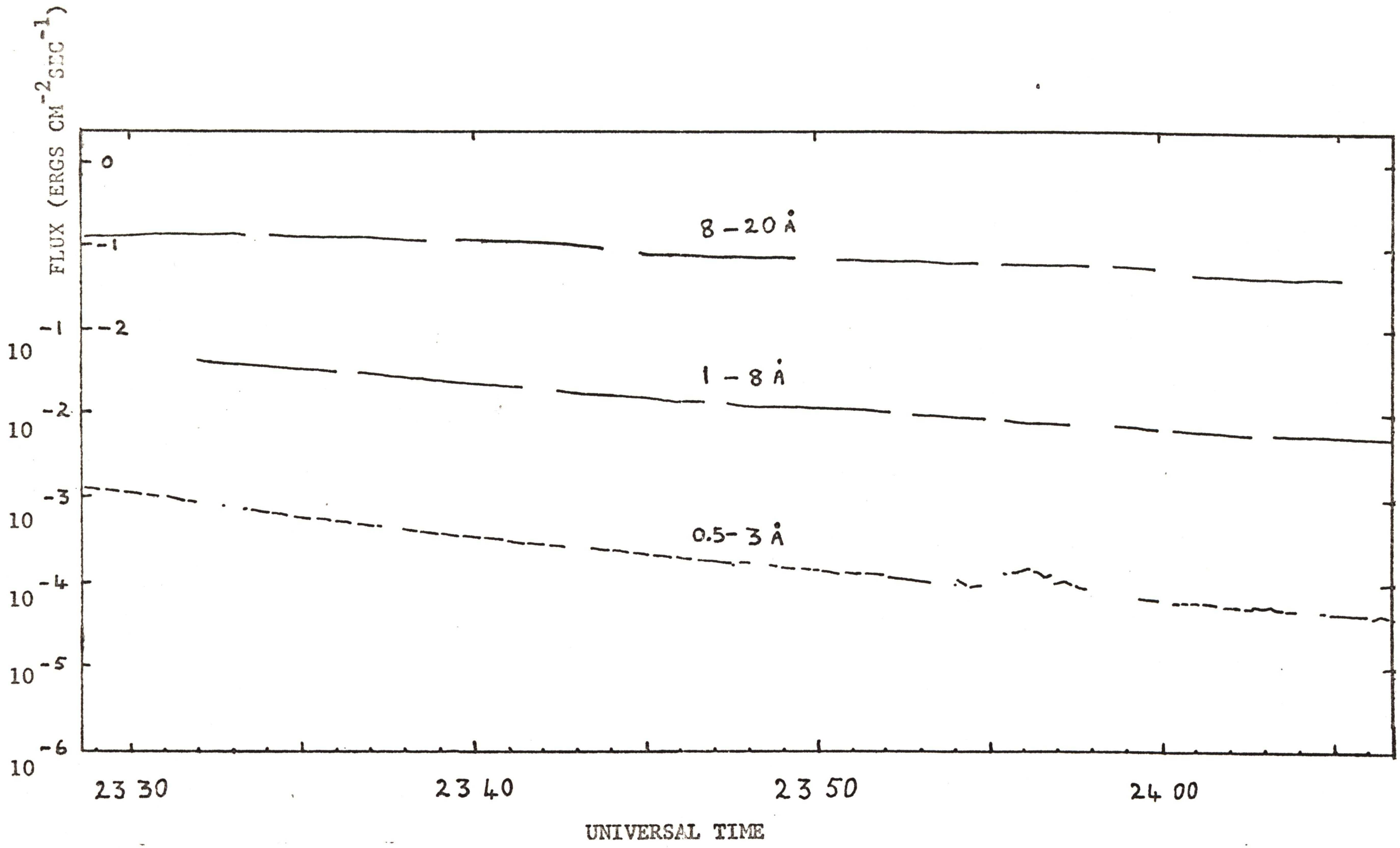

Figure III-3. OGO-4 broad band detector fluxes (gray body based) for class 1b flare of October 25, 1967 during the time shown. The wavelength bands of detectors are indicated on the graphs. Note the shift in the scale of 8 - 20 A flux.

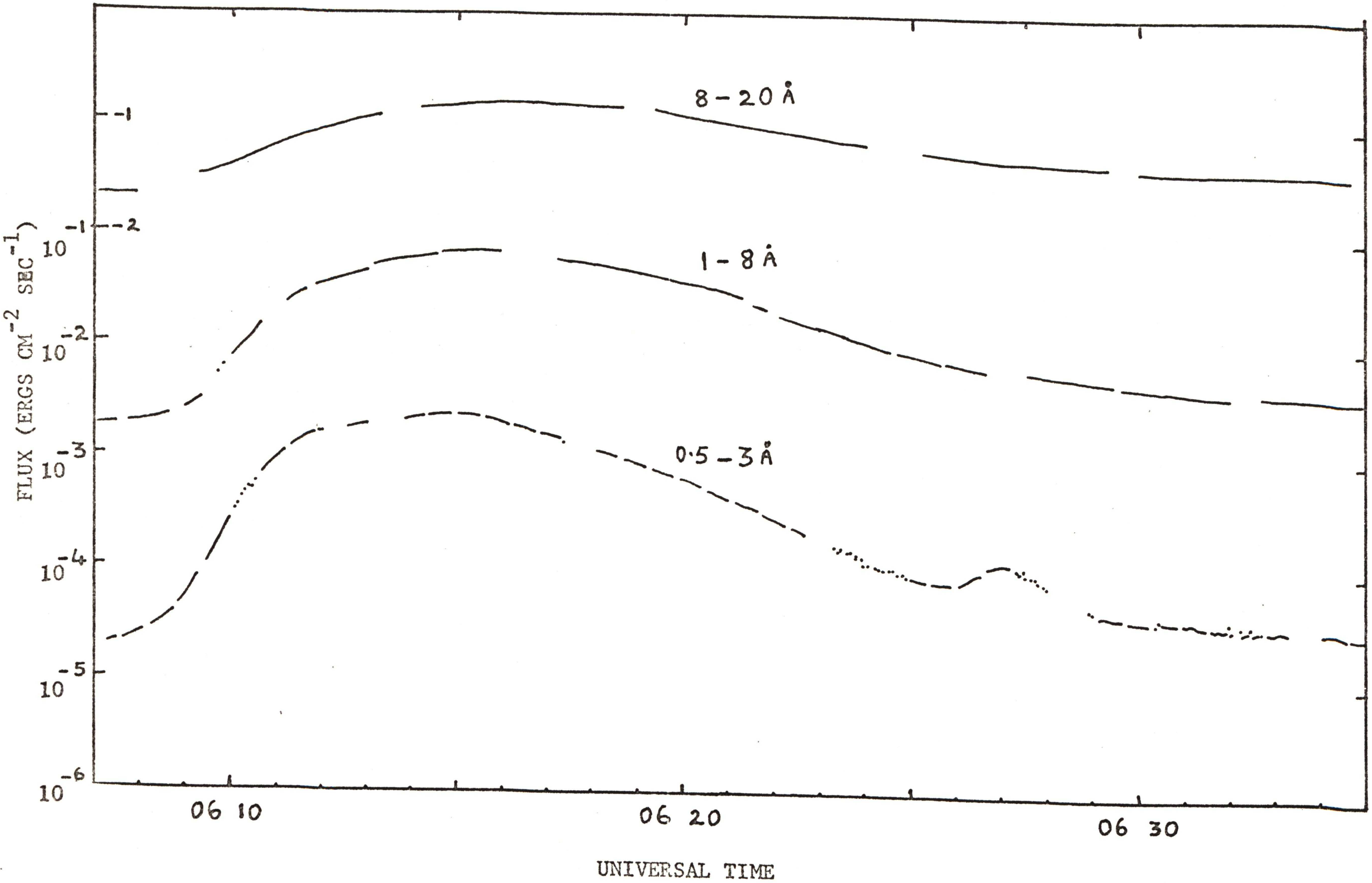

Figure III-4. OGO-4 broad band detector fluxes (gray body based) for class 1b flare of October 26, 1967 during the time shown. The wavelength bands of detectors are indicated on the graphs. Note the shift in the scale of 8 - 20 A flux.

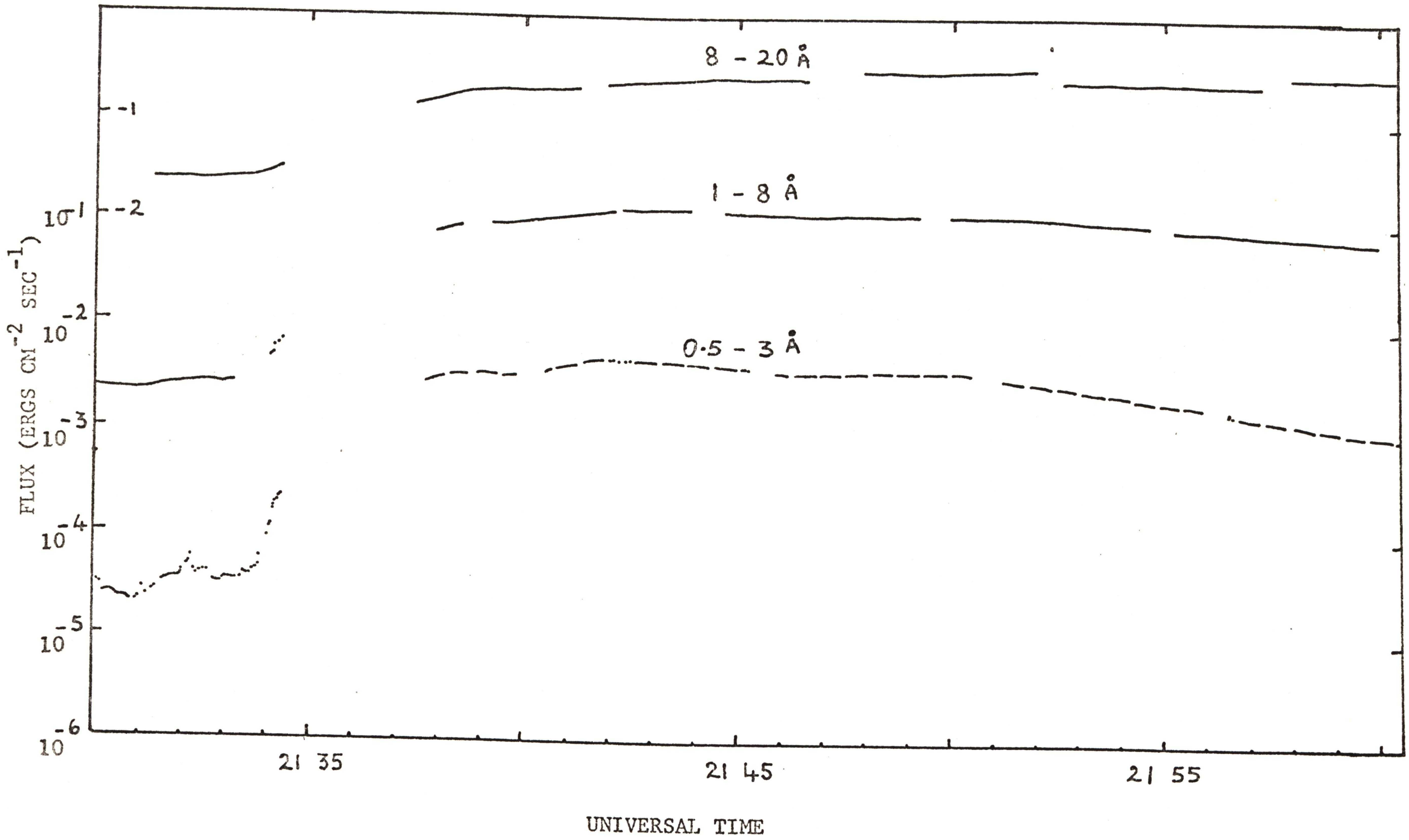

Figure III-5. OGO-4 broad band detector fluxes (gray body based) for class 3b flare of November 16, 1967 during the time shown. The wavelength bands of detectors are indicated on the graphs. Data loss before 2138 UT is due to a memory dump. Note the shift in the scale of 8 - 20 A flux.

the 1 - 8 Å flux reaches its peak after the 0 - 3 Å flux and this is followed by the 8 - 20 Å flux. In addition, the ratio of the peak flux to the flux before the commencement of the flare is the largest for the 0 - 3 Å flux; it exceeds two orders of magnitude for large flares (e.g., see Fig. III-5)

III.3 HORAN'S METHOD OF DATA ANALYSIS

The use of a gray body spectral assumption at a constant colour temperature is convenient for reducing large amounts of data as described above, but it is not physically realistic. Therefore Horan (1971) makes a more realistic spectral assumption for soft x-rays in the 0.5 - 8.0 Å region. He assumes that the emission is produced by thermal processes and that it consists mostly of continuum due to free-free (bremsstrahlung) and free-bound (radiative recombination) electron transitions. The emission spectrum is given by

$$E(FF{+}FB, \lambda, T) = C(FF{+}FB, \lambda, T)\, S \quad \mathrm{erg\ cm^{-2}\ s^{-1}\ A^{-1}}, \qquad (III.7)$$

where $C(FF{+}FB, \lambda, T) = C(FF, \lambda, T) + C(FB, \lambda, T)$ erg cm s^{-1} A^{-1}; (III.8a)

$$C(FF, \lambda, T) = F(FF, \lambda, T) \,/\, N_e N_H \,, \qquad (III.8b)$$

$$C(FB, \lambda, T) = F(FB, \lambda, T) \,/\, N_e N_H \qquad (III.8c)$$

and $S = \int N_e^2 \, dV$ $\mathrm{cm^{-3}}$ is the emission measure of the source region. The expressions for FF and FB fluxes per unit volume given by $F(FF, \lambda, T)$ and $F(FB, \lambda, T)$ respectively were taken from Culhane (1969a) (see equations II.2 and II.3, where the terms are defined; equation III.8a can also be calculated by using equation II.10 to within 10 per cent).

The ratio of the currents generated in 0 - 3 Å and 1 - 8 Å detectors is given by

$$r(FF+FB,T) = \frac{e\,\omega_{03}\int E_{03}(FF+FB,\lambda,T)\,\epsilon_{03}(\lambda)\,d\lambda}{e\,\omega_{18}\int E_{18}(FF+FB,\lambda,T)\,\epsilon_{18}(\lambda)\,d\lambda}, \qquad (III.9)$$

where the subscripts 03 and 18 refer to the two detectors under consideration. This ratio is a unique function of the electron temperature provided the source region is isothermal and the emission measure is the same for both spectral bands. In terms of the more convenient gray body fluxes this ratio can be written using equation (III.6) as,

$$R(FF+FB,T) = \frac{\phi_{03}(GB,T)}{\phi_{18}(GB,T)} = \left[\frac{K_{03}(GB,T_c)}{K_{18}(GB,T_c)}\right] r(FF+FB,T), \qquad (III.10)$$

where $K_{03}(GB,T_c)$ and $K_{18}(GB,T_c)$ are defined by equation (III.5).

Once the electron temperature is known, it is possible to calculate the absolute flux $\phi(FF+FB,T)$ based on a free-free and free-bound continuum spectrum from the observed gray body based flux $\phi(GB,T)$. For the 1 - 8 Å detector the flux correction factor which converts $\phi(GB,T)$ to $\phi(FF+FB,T)$ is given by the ratio

$$\frac{\phi_{18}(FF+FB,T)}{\phi_{18}(GB,T)} = \frac{K_{18}(FF+FB,T)}{K_{18}(GB,T_c)}, \qquad (III.11)$$

where the FF+FB conversion constant $K_{18}(FF+FB,T)$ is defined by

$$K_{18}(FF+FB,T) = \frac{\int C(FF+FB,\lambda,T)\,d\lambda}{e\,\omega_{18}\int C(FF+FB,\lambda,T)\,\epsilon_{18}(\lambda)\,d\lambda}, \qquad (III.12)$$

and $C(FF+FB,T)$ is the continuum flux per unit emission measure defined in equation (III.8).

Since the electron temperature and the gray body based flux $\phi(GB,T)$ of the solar source are known, the emission measure S of the source region can be determined by the following expression (for 1 - 8 Å detector):

$$\frac{\phi_{18}(GB,T)}{S} = K_{18}(GB,T_c)\ e\ \omega_{18} \int C(FF{+}FB,T)\,\epsilon_{18}(\lambda)\ d\lambda \qquad \text{(III.13)}$$

where the right hand side of the expression represents the gray body flux per unit emission measure. Horan (1970) and Dere et al., (1973) have given the values of R(FF+FB,T) and $\phi_{18}(GB,T)/S$ (equation III.10 and III.13). These are given in Table III-2 for temperatures upto 20 x 10^6K and are shown (by crosses) in Figure III-6. Also listed in the table are the flux correction factors defined by equation (III.11) for 0 - 3 Å and also for 1 - 8 Å detectors (note that this is equal to the ratio of the absolute flux (FF+FB) to the gray body based flux).

Thus the steps involved in Horan's method of determining the electron temperature and emission measure from OGO-4 flare data are the following:

(1) The 1 - 8 Å gray body flux must be split into two components when a flare is in progress by the formula

$$\phi(GB,T) = \phi_{flare}(GB,T) + \phi_{background}(GB,T') \qquad \text{(III.14)}$$

The value of $\phi_{background}(GB,T')$ is the value of the 1 - 8 Å gray body flux before the flare begins. This step approximates the multi-thermal nature of the solar corona. This background flux is produced by regions at about $T' \sim 2 \times 10^6$K. The larger the flare, the less critical this background value is.

(2) Determine the flare electron temperature T by taking the ratio of the 0.5 - 3 Å gray body flux to the 1 - 8 Å gray body flare flux $\phi_{flare}(GB,T)$ as determined by equation (III.14). Compare this ratio with the values of R(FF+FB,T) given in Table III-2. It is not possible to accurately determine temperatures greater than 20 x 10^6K. This can be seen in Figure III-6a where the curves become insensitive to high temperatures.

(3) Determine the flare emission measure S by dividing the 1 - 8 Å gray body flare flux $\phi_{flare}(GB,T)$ by the appropriate value of the 1 - 8 Å gray body flux per unit emission measure which is shown in Figure III-6b and is also listed in Table III-2.

Dere et al., (1973) have extended the calculations of Horan by including the line emission flux as predicted by the published tabulations (Tucker and Koren, 1971; Mewe, 1972b). An idea of the importance of the line flux can be obtained from Figure III-7. This figure shows the integral continuum (FF+FB) flux per unit emission measure as calculated by integrating the equation (II.10) and the total line emission flux per unit emission measure of all expected lines given by Mewe (1972b) between the wavelength limits of both detectors. Also shown is the total line flux per unit emission measure calculated from the tabulation of Tucker and Koren (1971) for the 1 - 8 Å detector in order to compare it with Mewe's values. It is seen that the line emission (mostly due to Si, Al and S in 5 - 8 Å region) is important for the 1 - 8 Å detector and is comparable to the continuum flux upto 12×10^6K. However, a study of available flare spectra obtained by OSO-4 spectrometers (see section III.5) suggests that the total line flux constitutes not more than 10 per cent of the soft x-ray continuum. Therefore Horan neglected the line emission in his calculations. From Figure III-7, it can be seen that the extent of error due to the neglect of the theoretical line flux is dependent on the temperature. The ratios R(FF+FB+L,T) of the gray body fluxes of the two detectors and the gray body flux per unit emission measure (calculated by Dere et al., 1973) which now include the theoretical line flux are shown (by circles) in Figures III-6a and III-6b respectively. A comparison of R(FF+FB,T) and R(FF+FB+L,T) shows that Horan's (1971) method underestimates the flare

TABLE III-2

PARAMETERS FOR OGO-4 DATA ANALYSIS ASSUMING A CONTINUUM SPECTRUM**

T (10^6K)	R(FF+FB,T)	ϕ_{18}(GB,T)/S*	$\frac{\phi_{03}(FF+FB,T)}{\phi_{03}(GB,T_c)}$	$\frac{\phi_{18}(FF+FB,T)}{\phi_{18}(GB,T_c)}$
2	1.33×10^{-5}	1.28×10^{-54}	0.019	0.953
3	1.90×10^{-4}	1.19×10^{-53}	0.177	0.873
4	8.27×10^{-4}	5.02×10^{-53}	0.422	0.752
5	2.04×10^{-3}	1.34×10^{-52}	0.635	0.653
6	3.98×10^{-3}	2.62×10^{-52}	0.782	0.576
7	6.77×10^{-3}	4.41×10^{-52}	0.875	0.517
8	9.88×10^{-3}	6.84×10^{-52}	0.929	0.470
9	1.33×10^{-2}	9.96×10^{-52}	0.959	0.432
10	1.73×10^{-2}	1.37×10^{-51}	0.972	0.402
11	2.13×10^{-2}	1.79×10^{-51}	0.976	0.377
12	2.47×10^{-2}	2.24×10^{-51}	0.974	0.356
13	2.82×10^{-2}	2.77×10^{-51}	0.968	0.339
14	3.30×10^{-2}	3.28×10^{-51}	0.960	0.325
15	3.75×10^{-2}	3.70×10^{-51}	0.952	0.313
16	4.19×10^{-2}	4.15×10^{-51}	0.943	0.302
17	4.52×10^{-2}	4.62×10^{-51}	0.933	0.294
18	4.73×10^{-2}	5.12×10^{-51}	0.924	0.286
19	4.85×10^{-2}	5.73×10^{-51}	0.916	0.280
20	4.93×10^{-2}	6.42×10^{-51}	0.907	0.274

* units: ergs cm^{-2} s^{-1}/ cm^{-3}

** Dere et al. (1973)

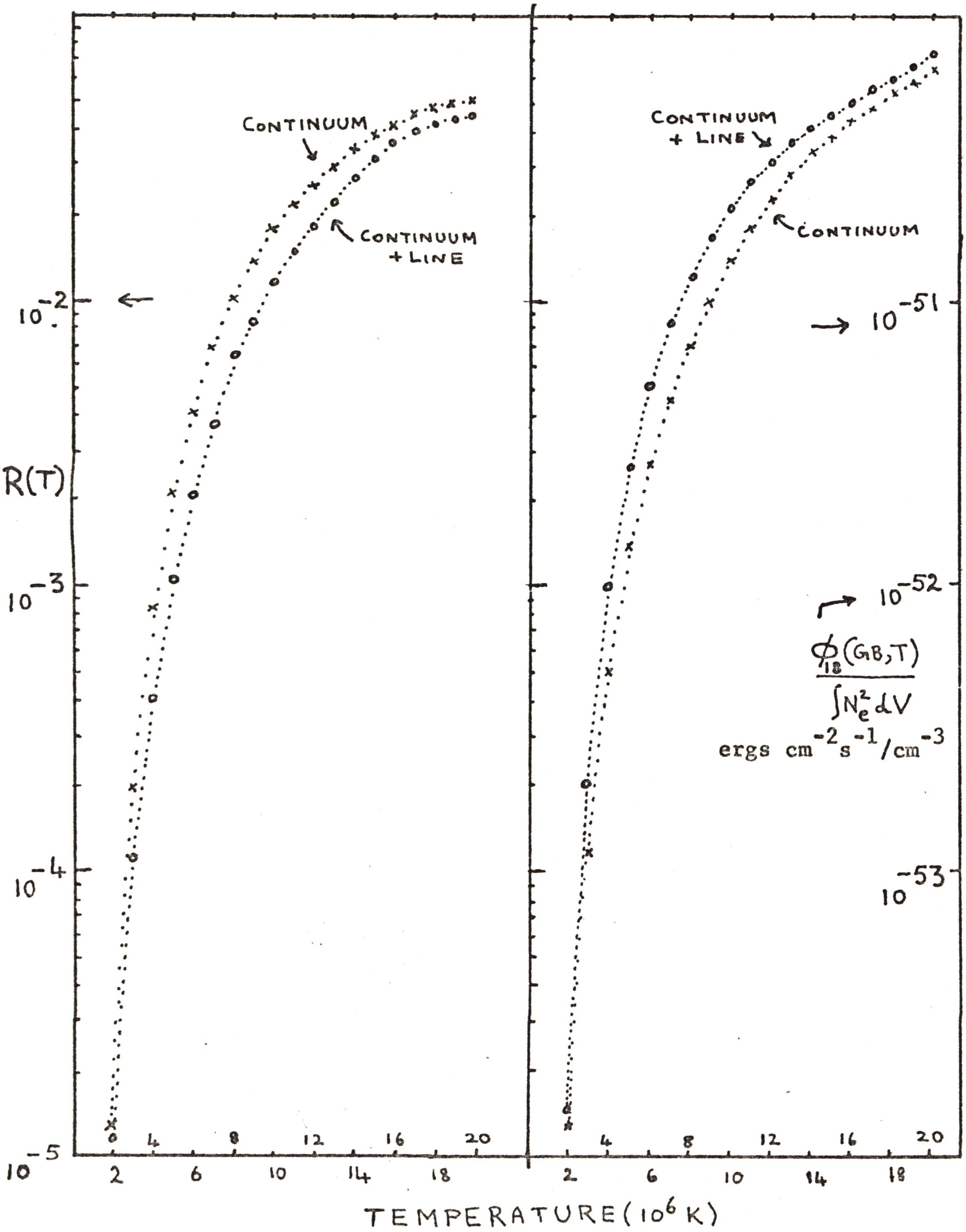

Figure III-6. (a) Ratio of gray body fluxes from 0-3 A and 1-8 A broad band detectors, and (b) 1-8 A gray body flux per unit emission measure, both as a function of T. Crosses indicate values which assume free-free and free-bound continuum emission; circles indicate values which assume both continuum and line emission. (Plotted from values given by Dere et al., 1973.)

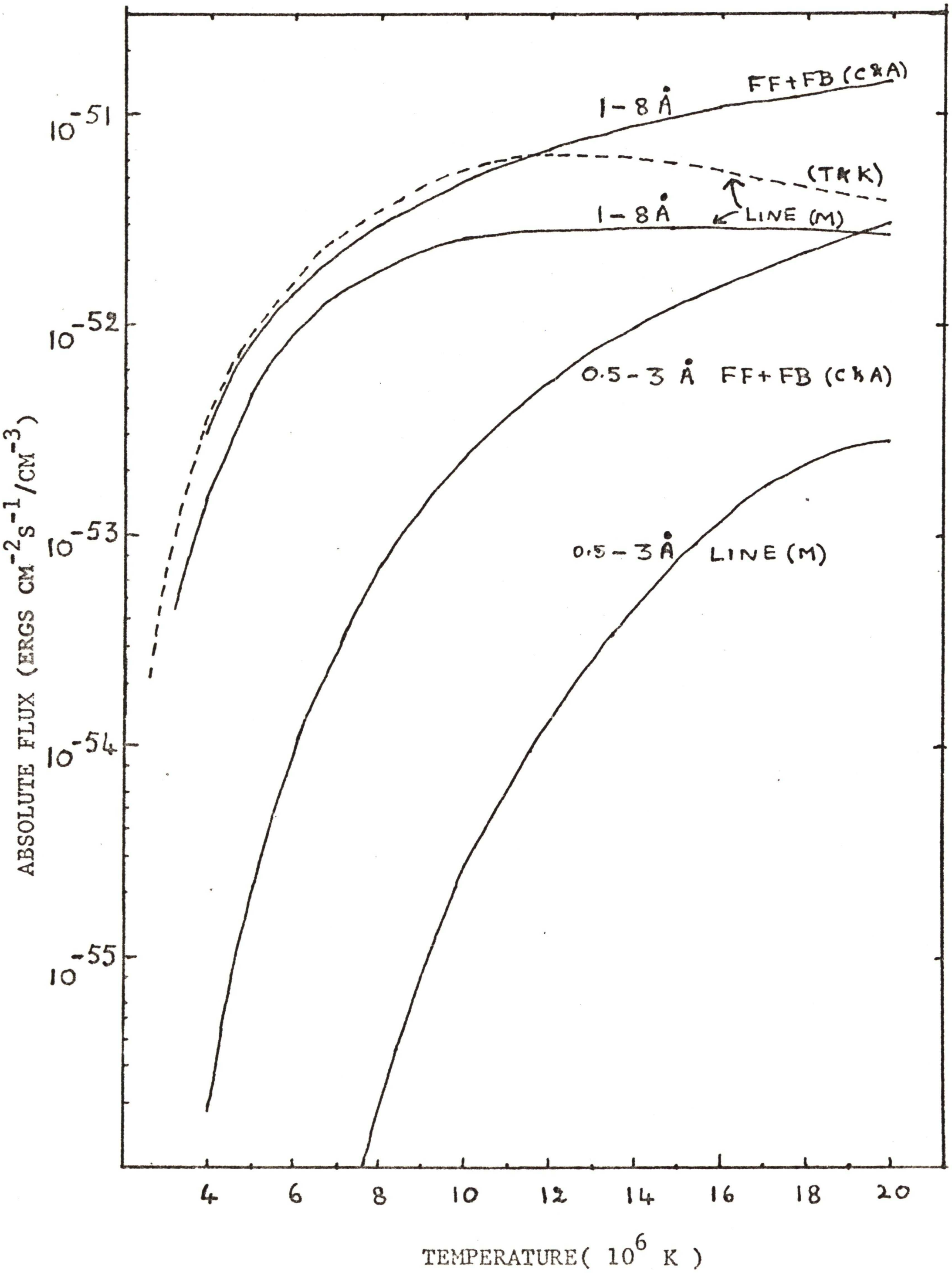

Figure III-7. Absolute broad band fluxes per unit emission measure due to continuum (FF+FB) and due to line emission in both 0.5 to 3 Å and 1 to 8 Å bands are plotted against T. Culhane and Acton's (C&A) expression (II.10) was integrated for the continuum flux; Tucker and Koren's(1971) (T&K) as well as Mewe's (1972b) (M) tabulations were summed to obtain line fluxes. Notice the differences between the values of T&K and M.

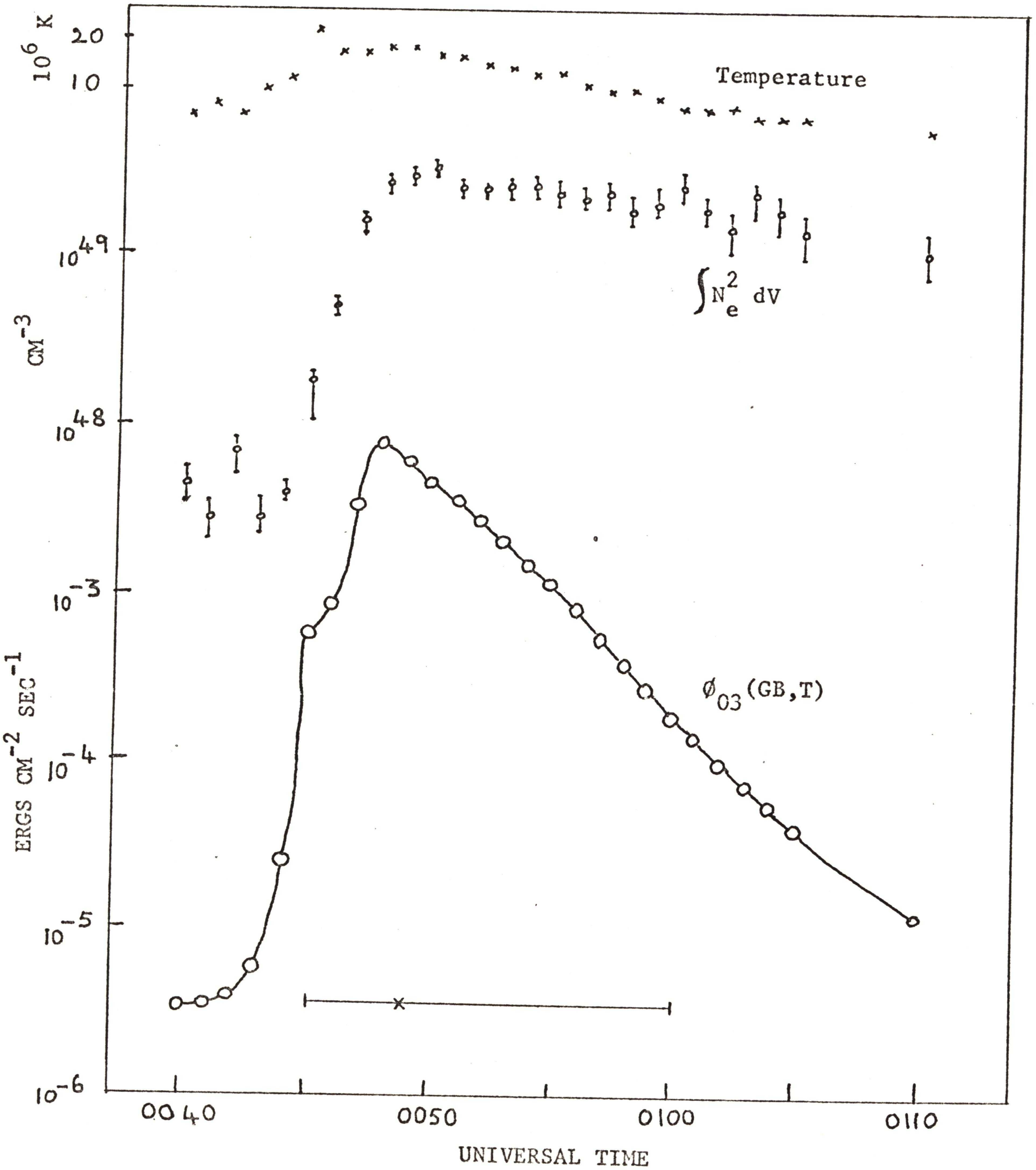

Figure III-8. Time history of the observed gray body flux (0 - 3 Å) for the flare of August 2, 1967 (same as in Fig III-2); emission measure and temperature of the flare plasma, also shown above, were calculated by Horan (1970) by assuming that FF+FB continuum emission is responsible for the observed flux.

temperature by neglecting the line flux and therefore overestimates the emission measure. The dependence of the flare time history on the spectral assumptions discussed above will be dealt with in Chapter V.

III.4 RESULTS OF FLARE DATA ANALYSIS

Horan (1970, 1971) studied 17 solar flares which occurred during the latter half of 1967. He determined the time history of the flare temperature and emission measure from the available data from 0 - 3 Å and 1 - 8 Å bands. These flares included three varieties: fast-rising disk flares, slow rising disk flares, and limb flares. The flares listed in section III.2 are examples of those termed as fast-rising by the rate of increase of the pre-peak x-ray energy flux. Typical results of his analysis are shown in Figure III-8 which is based on data of Figure III-2. It shows the time history of ϕ_{03}(GB,T), the observed flux from the 0 - 3 Å detector, and the computed values of the emission measure and the temperature at the time of observation.

The important results of his analysis of all the 17 flares are the following (Horan, 1971):

(1) There is no characteristic difference between disk flares and limb flares.

(2) The temperature rises rapidly and peaks before either the 0 - 3 Å x-ray flux or the emission measure implying that a greater number of electrons is involved in the emission as the flare evolves, even though the average energy per unit volume is decreasing.

(3) The 0 - 3 Å x-ray flux peaks after the temperature peaks and before the emission measure peaks.

(4) The emission measure rises rapidly by a few orders of magnitude during the initial phase of the event, reaches a peak value and remains

fairly constant for a considerable time ($\sim$ 30 minutes).

Horan's main conclusions are the following:

(1) During the initial phases of the flare, the behaviour of the soft x-ray flux (0 - 3 Å or 1 - 8 Å) is primarily determined by the emission measure.

(2) During the decay phases of the flare, the behaviour of the soft x-ray flux is mainly determined by the decreasing temperature.

(3) Since OGO-4 detectors view the entire sun, the background x-ray flux has a considerable effect on the determination of the temperature and emission measure of the flares, particularly during their beginning phases. This background flux is due to extensive active solar regions with electron temperatures less than 8×10^6K (Horan et al., 1973, show by their multithermal analysis that plasma components at temperatures from 2 to 5×10^6K are present before the onset of the flare). Since the flare has a higher temperature and a much less extensive source region, what the OGO-4 data analysis does is to force fit a single average temperature to fluxes coming from the flare plasma (see equation III.14).

(4) The temperatures determined from line intensity ratios from available OSO-4 spectrometer data are inconsistent with those determined from simultaneous OGO-4 data. This is accounted for in part by the fact that during the 14 minute scanning time of the OSO-4 spectrometer, different lines are scanned at different flare conditions (T and S).

III.5 THE NRL OSO-4 SPECTROMETER EXPERIMENT

The NASA's OSO-4 spacecraft (OSO-4, 1967-100A) was launched on October 18, 1967, and carried a number of instruments as described in section I.2 to study the solar soft x-ray emission. Dr. John Meekins, the principal investigator of the NRL experiment, placed two Bragg crystal spectrometers in the pointed section of the OSO-4 spacecraft. Technical details of the instrument are described by Meekins et al., (1968, 1970), Horan (1970) and Meekins (1972). A brief outline is given below.

A photograph of the instrument is given in Figure III-9 (courtesy of Meekins). One of the spectrometers contains a lithium fluoride crystal (LiF for which the atomic plane spacing $d \approx 2 Å$ so that $2d \approx 4 Å$), which scans from 0.7 to 3.8 Å; the other contains an ethylene diamine d-tartrate crystal (EDDT; $2d \approx 8 Å$), which scans from 1.5 to 8.5 Å. Both spectrometers lie one above the other on a common axis of rotation and are driven by the same stepping motor in steps of 6 arc-minutes (0.1 degree) width each. The crystals cover their respective spectral ranges in 660 steps and scan in both increasing and decreasing directions of wavelength.

The soft x-radiation from the entire sun passes through an entrance aperture covered with an aluminum coated Mylar filter ($C_{10}H_8O_4$, 6.25×10^{-4} cm. thick; area density of Mylar, $\rho x = 0.84$ mg cm^{-2}; area density of Al, $\rho x = 0.054$ mg cm^{-2}). The purpose of this filter is to reflect unwanted UV radiation and heat. The radiation transmitted by the filter is diffracted by the two crystals according to Bragg's law

$$n\lambda = 2d \sin\theta , \qquad \text{(III.15)}$$

where n is the order of diffraction, λ is the wavelength of the radiation diffracted (Å), d is the atomic plane spacing of the crystal, and θ is the angle between the incident radiation and the atomic planes of the crystal (also known as the Bragg angle).

The diffracted radiation is viewed by two identical side-window Geiger counters. The detectors co-rotate at twice the angular rate of the crystals in order to satisfy the Bragg relation for all angles θ. The Geiger counters, which are 1.87 cm deep, are filled to a pressure of 650 mm Hg with one per cent of bromine as quenching agent in argon (area density of argon, ρx = 2.585 mg cm^{-2}; area density of bromine, ρx = 0.104 mg cm^{-2}). In order to be compatible with the halogen quench, the detectors are provided with mica windows (area density $\approx$ 1.5 mg cm^{-2}; believed to be Ruby India variety). The Geiger counters were operated at 1200 volts and had a dead time τ = 200 micro seconds which included that of the associated electronics. The efficiency of the detectors were not experimentally determined before launch (Doschek, personal communication).

Limitations: The original objective of the experiment was to obtain high resolution spectra of the continuum and line emission components of the solar flare soft x-ray emission and also be able to measure the Doppler line profiles. However, the spacecraft limitations (Meekins, 1972) forced many restrictions on the design of the instrument and consequently the final instrument could not measure all the parameters required to describe the solar flare plasma state. Some of the restrictions and their consequences are the following:

(i) The selection of crystals with limited area required relatively long integration times to obtain a sufficient number of counts from lines and continuum radiation of the solar spectrum below 10 Å. This requirement made the scan rate so slow (1.28 sec per step) that it took nearly 14 minutes to complete a scan.

(ii) The wavelength resolution had to be reduced by increasing the width $\Delta\theta$ of each spectrometer step to 0.1 degree (1.745×10^{-3} radian) so that some information on the time history of the x-ray emission in various parts of the spectrum during the rapidly changing flare conditions can be obtained. In order to measure the line intensities accurately and

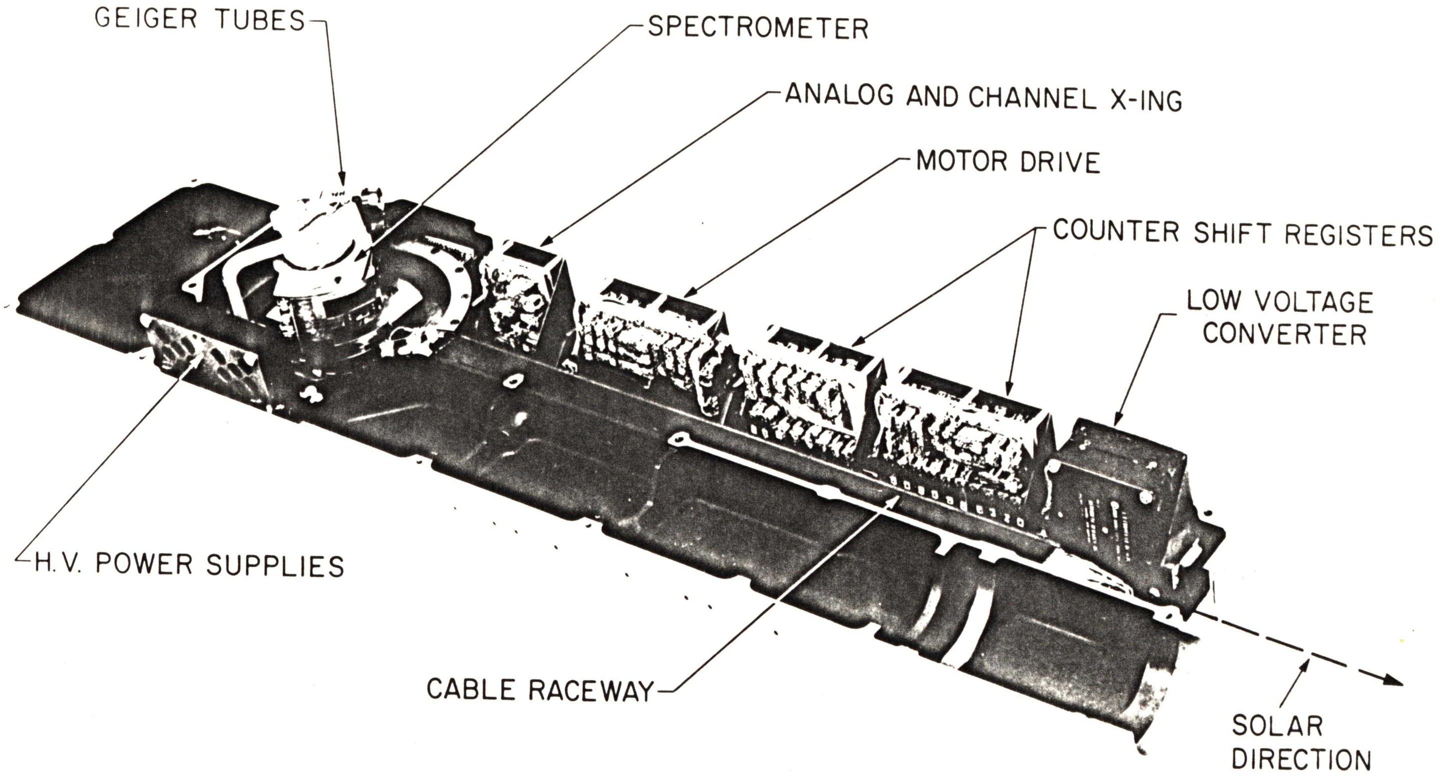

Figure III-9. Photograph of the NRL Bragg Crystal Spectrometer instrument mounted at the pointed section of the OSO-4 spacecraft (courtesy of Dr.J. F. Meekins).

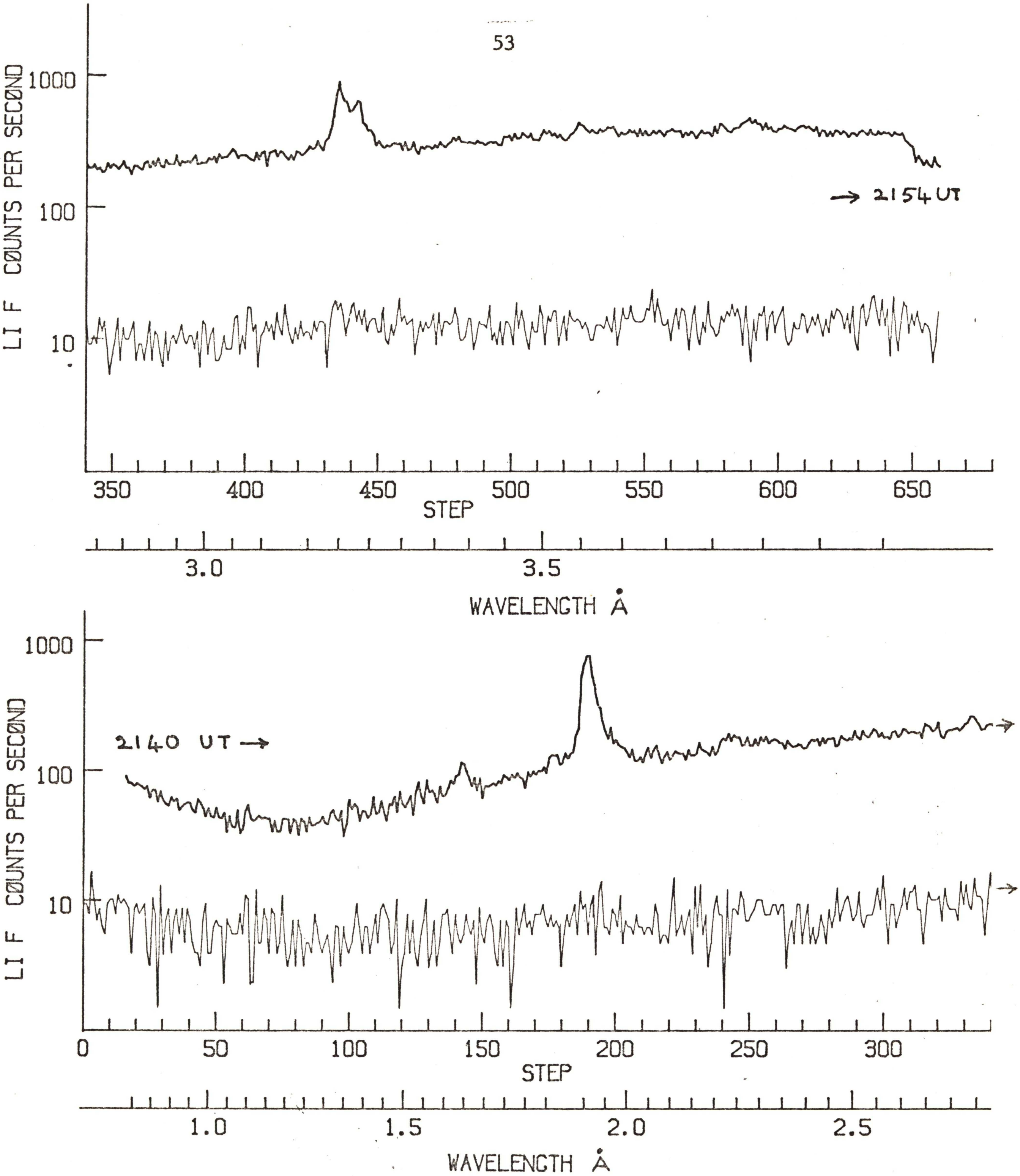

Figure III-10. OSO-4 LiF spectrometer scan (upper) of a class 3b solar flare of November 16, 1967 at 2143 UT. The scanning time, from 2140 UT (step #0) to 2154 UT (step #660), covers the maximum phase of the flare (see OGO-4 data in Fig III-5). Notice the raster motions near step #180 and #410. Also notice that most of the spectral energy is in the form of continuum. For comparison a typical scan (lower) from an active sun is also shown. Background is ~8 c/s. (Courtesy of Meekins)

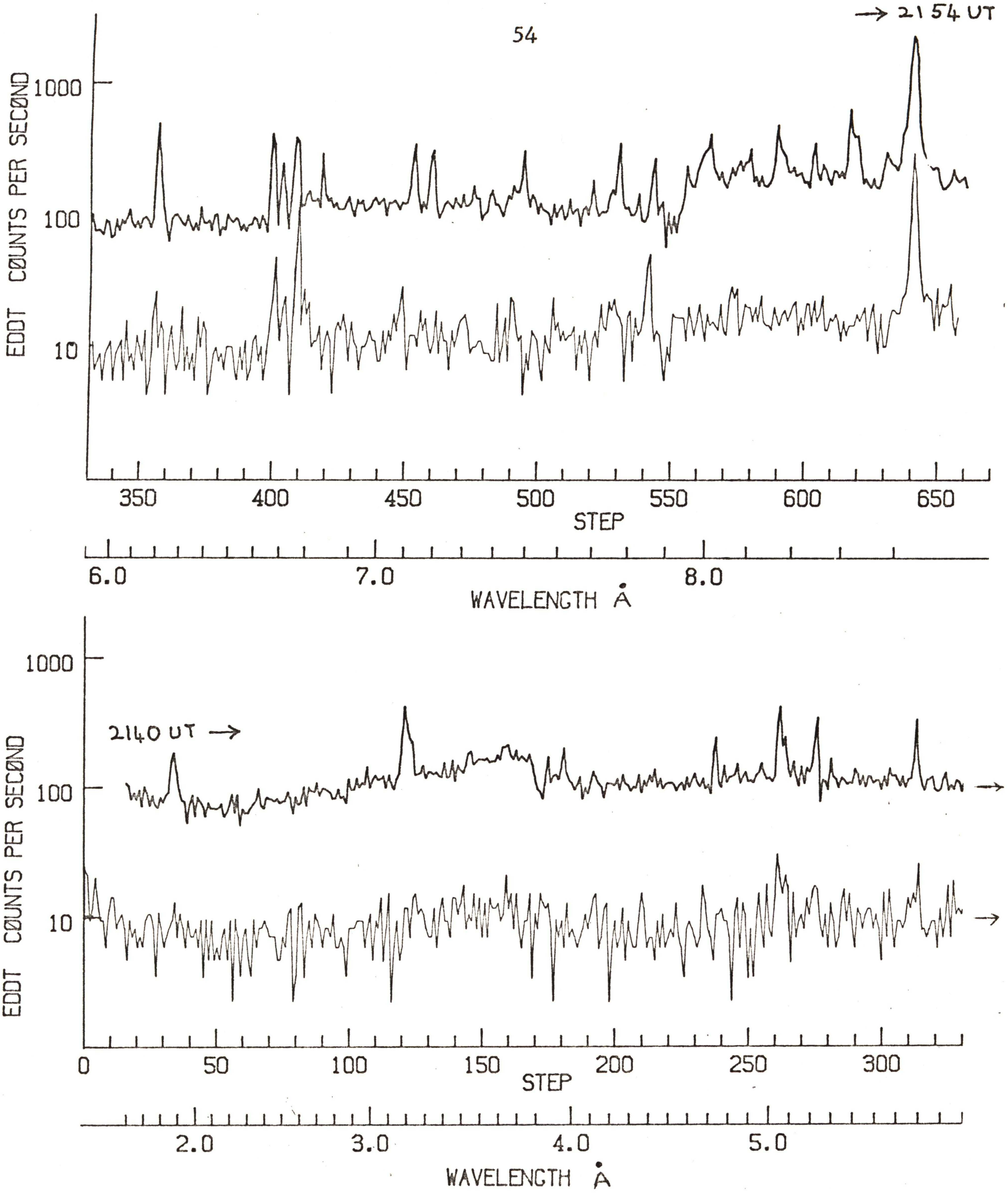

Figure III-11. OSO-4 EDDT spectrometer scan (upper) of a class 3b solar flare of November 16, 1967 at 2143 UT. The scanning time, from 2140 UT (step #0) to 2154 UT (step #660), covers the maximum phase of the flare (see OGO-4 data in Fig III-5). Notice the raster motions near step #180 and #410. Also notice that most of the spectral energy is in the form of continuum. For comparison a typical scan (lower) from an active sun is also shown. Background is ~8 c/s. (Courtesy of Meekins) avoid the possibility of missing any line between successive steps, the crystals were selected to have the full-width at half-maximum (FWHM) of their rocking curves (explained in Appendix B) greater than or equal to $\Delta\theta$ (0.1 degree).

(iii) Because of (ii) the instrument spectral resolution was insufficient to measure profiles even with fine collimation. For this reason fine collimation was not employed.

DATA PRESENTATION

The counts per sample period measured in the detectors as a function of the step number (out of 660 steps making up a complete scan) are telemetered to the ground receivers by on board storage and delayed transmission (this facility failed in May 1968). Therefore the data are displayed as counts per second as a function of the step number N and also of the corresponding wavelength λ(A). Examples of the data are shown in Figures III-10 and III-11 from LiF and EDDT spectrometers respectively. They compare scans from a typical non-flaring (quiet or active, lower plot) and a flaring (upper plot) sun.

The linear relationship between the step number N and the corresponding Bragg angle θ is given by

$$\theta = N\Delta + \varphi + \alpha$$

where Δ = 0.1 degree

φ = 9.778 degrees (LiF); 8.984 degrees (EDDT)

$\alpha = \begin{cases} \text{Elevation angle of the spacecraft above the center} \\ \text{of the solar disk; } \pm 1 \text{ arc minute for the pointed} \\ \text{mode.} \end{cases}$

The wavelength λ has a non-linear relationship to θ and is given by (for n = 1)

$$\lambda = 2d \sin\theta$$

where $2d = \begin{cases} 4.006\ \text{Å LiF} \\ 8.798\ \text{Å EDDT} \end{cases}$

III.6 THEORY OF DATA ANALYSIS

It is necessary to determine the absolute photon flux entering the instrument before attempting to analyze the data. Let the incident photon flux be denoted $I(\lambda)$ photons $cm^{-2}\ s^{-1}\ Å^{-1}$ between wavelengths λ and $\lambda + d\lambda$ corresponding to the Bragg angle between θ and $\theta + d\theta$. This is to be calculated from the observed count rate r_c (sec^{-1}) at a certain step number corresponding to θ.

To do this, consider the Figure III-12 which sketches how the various components of the spectrometer affect the incident photon flux.

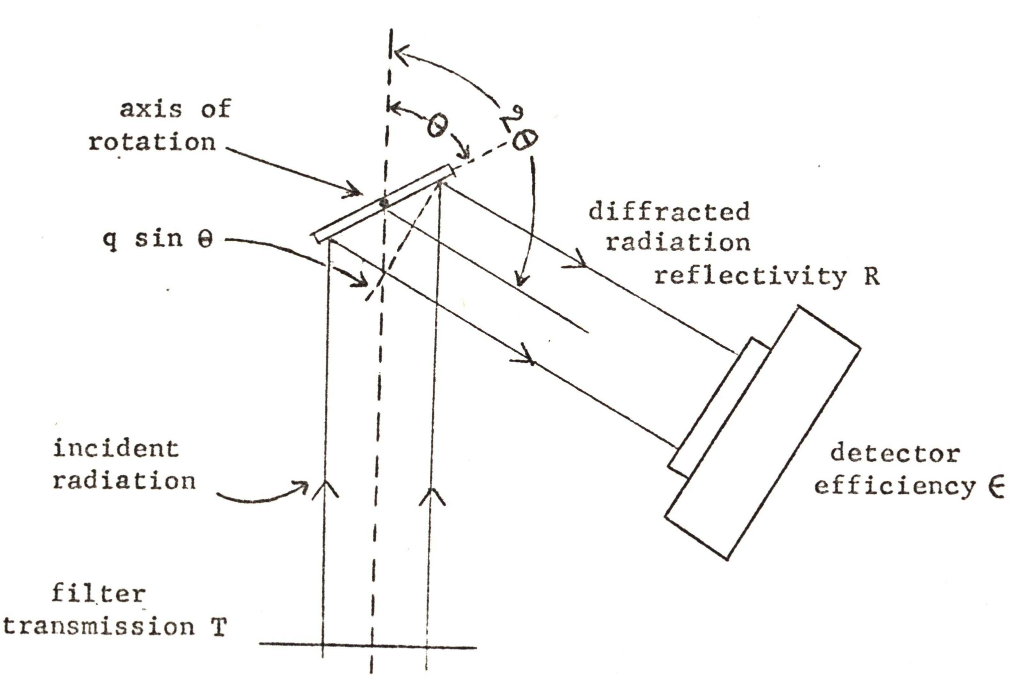

Figure III-12. The main components of a Bragg crystal spectrometer which affect the incident x-radiation are sketched. The length l (see text) of the detector window is perpendicular to the axis of rotation. This may be larger or smaller than the effective length q sin θ of the crystal.

Several factors affect the incident photons as they reach the detector and are counted. They are:

(1) The probability $T(\lambda)$ that a photon of wavelength λ is transmitted by the filter.

(2) The integral reflectivity of the crystal $R(\lambda)$ as the photons are diffracted at the appropriate Bragg angle θ.

(3) The quantum efficiency $\epsilon(\lambda)$ of the Geiger counter which is due to photon transmission by the mica window and absorption by the gas.

(4) The effective area A' of the detector which is determined by the relative orientation between the detector window (length $\ell = 1.918$ cm, breadth $b = 0.419$ cm) and the crystal surface (square with side $q = 2.54$ cm). It is clear from Figure III-12 that the effective area is equal to $bq \sin\theta$ or $b\ell$, whichever is less. This determines the photon flux reaching the detector.

(5) The dead time τ of the Geiger counter.

If r_c is the observed counting rate, it is related to the rate of photon absorption r_p by the detectors by the relation

$$r_p = \frac{r_c}{1 - \tau r_c} - r_B , \qquad \text{(III.16)}$$

where r_B is the background counting rate which is determined from quiet scans to be about 8 counts/sec and is independent of the Bragg angle θ.

If I_θ is the incident flux (photons/area/time/angle) then it is related to the true counting rate r_p by

$$I_\theta = \frac{r_p}{A' R \epsilon T} \quad \mathrm{cm}^{-2}\ \mathrm{s}^{-1}\ \mathrm{radian}^{-1} \qquad \text{(III.17)}$$

Now I_θ is displayed as a function of the angle and it is possible to separate the line and continuum fluxes such that

$$I_\theta = I^c_\theta + I^L_\theta ,$$

where the superscripts c and L refer to the continuum and the line components respectively.

Meekins (1972) has shown that the total photon flux in a line is

$$I^L(\lambda) = \sum I^L_\theta \,\Delta\theta \qquad \text{photons,} \qquad \text{(III.18a)}$$

where $\Delta\theta = 0.001745$ radian. For approximately flat continuum,

$$I^c(\lambda) = \frac{1}{\Delta\lambda}\int_{\Delta\lambda} I^c(\lambda)\, d\lambda = \frac{1}{\Delta\lambda}\int I^c_\theta\, d\theta = I^c_\theta\left(\frac{\Delta\theta}{\Delta\lambda}\right) = I^c_\theta/(2d\cos\theta)$$

$$\text{photons/Å} \qquad \text{.....(III.18b)}$$

The sum of equations (III.18a) and (III.18b) gives the incident photon flux (photons $\mathrm{cm}^{-2}\ \mathrm{s}^{-1}\ \mathrm{Å}^{-1}$)

$$I(\lambda)_c = \frac{I^c_\theta}{(2d\cos\theta)} + I^L(\lambda)\, S(\lambda,\lambda_0) \qquad \text{(III.19)}$$

Here $S(\lambda, \lambda_0)$ is the Gaussian profile of a line centered at λ_0 (valid for optically thin plasmas) and is of the form (for Doppler broadening only)

$$S(\lambda,\lambda_0) = \left(\frac{mc^2}{2\pi kT\lambda_0}\right)^{1/2} \exp\left[-\frac{mc^2}{2kT\lambda_0^2}(\lambda^2-\lambda_0^2)\right] , \qquad \text{(III.20)}$$

where m is the mass of the ion forming the line, c is the velocity of light, k is Boltzmann's constant and T is the kinetic temperature of the ions. This correction cannot be applied until the identification of the line is established and the temperature of its emission is determined. However it is easier to analyze the incident continuum flux. It can be seen in Figure III-10 that most of the spectrum from 1 to 3.8 Å can be considered to be a continuum except for the line features at 1.9 Å and at 3.2 Å. In such cases equation (III.17) and (III.18b) can be combined to give the incident continuum flux (first order correction only)

$$I(\lambda) = \frac{r_p}{A'Q} , \qquad \text{(III.21a)}$$

where $Q = R \epsilon T\,(2d \cos \theta)$, (III.21b)

and also $2d \cos \theta = \sqrt{(2d)^2 - \lambda^2}$

This equation is not dependent on the plasma parameters and therefore the spectrum of the incident continuum flux can be derived from the observed continuum count rate. It is, however, necessary to know as accurately as possible the values of the three parameters $R(\lambda)$, $\epsilon(\lambda)$ and $T(\lambda)$. As no pre-flight experimental calibrations were made, Meekins (1972) carried out a theoretical evaluation of the parameter Q (equation III.21b). This is shown in Figures III-13a and III-13b as a function of λ for the two spectrometers. The discontinuities in these theoretical calibration curves are due to the following absorption edges:

Element	Source	Edge at
Potassium	Mica Window	3.43 Å
Argon	Counter fill gas	3.87 Å
Silicon	Mica Window	6.74 Å
Aluminum	Mica Window; Filter	7.95 Å

Except for the minor potassium absorption edge, the other absorption edges produce readily identifiable jumps in the continuum as can be seen in the EDDT flare spectrum (Figure III-11) and also in the LiF flare spectrum (Figure III-10), where the scan limit is near the Ar absorption edge.

A few words concerning $R(\lambda)$ and $\epsilon(\lambda)$: As discussed in Appendix B, the reflectivities of real crystals cannot be theoretically calculated and

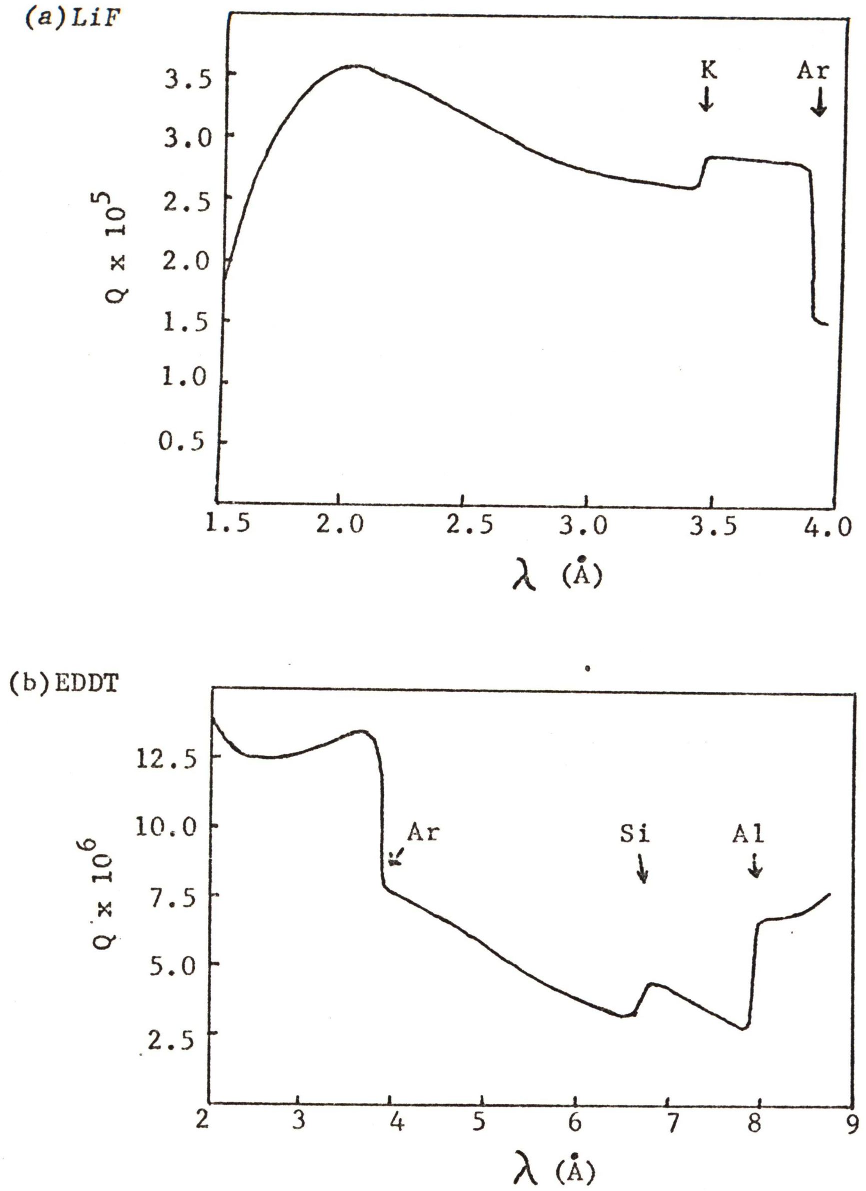

Figure III-13. Plot of calculated instrumental calibration parameter Q (= R ϵ T.2d cos θ) as a function of wavelength: for (a) LiF spectrometer, (b) EDDT spectrometer.
The absorption edges due to potassium, argon, silicon and aluminum are also indicated. The effect of these absorption edges may be seen in the flare scan in Figure III-11.
(Meekins, 1972)

have to be experimentally determined. Meekins (1973) finds that the reflectivities also depend on the order of diffraction n of the line and λ. The higher order reflectivities $R(n, \lambda)$ where $n > 1$, are not negligible compared to the first order reflectivity $R(1, \lambda)$. These reflectivities have recently been experimentally determined (Meekins, private communication) for orders upto $n = 4$ for LiF crystals similar to those flown in OSO-4.

Doschek and Meekins (1973) have also drawn attention to the fact that because of uncertainties in the amounts of various elements (Si, Al etc.) in the mica window of the Geiger counters, the calculated efficiencies ($\epsilon(\lambda)$) have considerable errors particularly at the absorption edges. Therefore the theoretical parameter Q (equation III.21b) cannot be relied upon. The experimental evaluation of these instrumental parameters will be discussed in Chapter IV.

ERRORS AND ACCURACY OF THE DATA

The OSO-4 spectrometers have produced a large number of scans similar to those in Figures III-10 and III-11, during the operative lifetime of the spacecraft. From these scans those pertaining to interesting events such as solar flares can be selected and studied. The accuracy of wavelengths in the data is affected by the following factors:

(1) Most of the scans (as much as 90 per cent of the usable scans) were obtained when the spacecraft was operating in the raster mode required for other experiments placed aboard OSO-4. Then the pointed section of the spacecraft would perform a raster scan of the sun covering 40 arc minutes by 40 arc minutes (Horan, 1970). In the worst case, this rastering motion introduces an angular uncertainty $\Delta \theta$ as great as 50 arc minutes for a limb flare which corresponds to an error $\Delta\lambda$ as great as 0.09 Å at the shorter

wavelengths. The error $\Delta\lambda$ can be precisely determined from the shift in the position of a well known line such as the Lyman-α line of Mg XII at 8.421 Å. The angular error $\Delta\theta$ can then be determined from the equation

$$\Delta\lambda = \Delta\,\theta(2d \cos\theta).$$

Once $\Delta\theta$ is known $\Delta\lambda$ at other values of λ can be obtained from the above equation.

When the rastering motion reverses its direction it jolts the stepping motor of the spectrometers. This can be seen at step numbers 180 and 410 in both Figures III-10 and III-11. At those points the data becomes distorted and cannot be used for analysis. This is particularly serious when lines are present.

(2) For the remainder of the scans which are obtained with the spacecraft pointing at the centre of the solar disk, a flare located at the solar limb produces an uncertainty in $\Delta\theta \approx 15$ arc minute compared to radiation coming from the centre. In the extremely rare case of two or more flares occurring simultaneously it would be difficult to determine $\Delta\theta$ with the available resolution.

(3) The wavelength resolution in the spectrometers is determined by the step increment of 0.1 degree (1.745×10^{-3} radians). The corresponding value of $\delta\lambda$ is given by

$$\delta\lambda = 1.745 \times 10^{-3} \cdot \sqrt{(2d)^2 - \lambda^2}$$

where $\lambda = 2d \sin\theta$. The values of $\delta\lambda$ at the extremes ($9^\circ \lesssim \theta \lesssim 72^\circ$ for both crystals) of the spectral scans are given by

θ		9^o	72^o
$\delta\lambda$ (LiF)	:	6.9×10^{-3} Å	2.2×10^{-3} Å
$\delta\lambda$ (EDDT)	:	1.5×10^{-2} Å	4.8×10^{-3} Å

The resolution is given by $\delta\lambda/\lambda$. It can be seen that the highest resolutions occur near the longest wavelength limits of the scans. Also the resolution of the LiF spectrum is better than that of EDDT spectrum by a factor of 2 to 3 for wavelengths upto 3.9 Å.

III.7 PRELIMINARY ANALYSIS OF OSO-4 DATA

A preliminary list of identified lines and their approximate wavelengths, as determined from the uncorrected scans of a flare, was given by Meekins et al., (1968, 1970). The line identifications were done according to these criteria: The wavelengths as determined by the scan data must agree closely with either theoretical or laboratory determined wavelengths (available up to the time of publication); the most probable transition for the ion in this wavelength region must be observed; and the appearance of the lines must be consistent with the physical conditions of the flare plasma which are approximately known. Most of the lines were due to the well known transitions of H-like and He-like coronal ions. A few lines between 8 and 8.4 Å were tentatively identified as the K-α transitions of aluminum. Similar transitions of other ions were also given by them.

Meekins et al., (1970) also qualitatively analyzed the scans of the largest flare event observed by the OSO-4; it was a class 3b flare which occurred on November 16, 1967. The first scan began at 2140 UT at the short wavelength limit and at 2154 UT reached the long wavelength limit of both spectrometers; it is shown in Figures III-10 and III-11. The OGO-4 record of the same event is shown in Figure III-5. This shows that the 0 - 3 Å flux has changed by at least a factor of 2 during the same OSO-4 scan period. Meekins et al., (1970) compared the plasma parameters determined from the OSO-4 data with those determined from OGO-4 data. Ignoring temporal variations in the OSO-4 data they found that the ratio of Lα line intensities of Mg XII and Si XIV gave a temperature of $\sim 10 \times 10^6$ K; that of Si XIV and S XVI gave a temperature of $\sim 18 \times 10^6$K. The ratio of Lα line of Si XIV to He-like resonance line of Si XIII (equation II.15) gave a temperature of $\sim 14 \times 10^6$ K and a similar ratio for sulfur gave a temperature of $\sim 19 \times 10^6$ K. The OGO-4 flux ratios (0 - 3 Å and 1 - 8 Å) indicated a temperature of 14×10^6 K at 2144 UT assuming the continuum was due to free-free and free-bound emission. The OSO-4 continuum spectrum between 1.5 Å and 3.8 Å was corrected by calculated instrumental parameters as described in section III.6. This was fitted by a least-squares method to a continuum flux expression of the type

$$F = a \lambda^{-2} \exp(-b/\lambda) \qquad \text{(III.22)}$$

where a and b are fitted parameters (note that this is similar to Culhane's equations given by II.2 and II.3). Meekins et al., (1970) found that different regions of the spectrum gave temperatures ranging from 14×10^6K to 28×10^6K. They estimated the emission measure to be about 7×10^{50} cm^{-3} based on a pure free-free flux. The difference in temperature determinations from OGO-4 and OSO-4 data led Meekins et al., (1970) to suggest that the flare plasma should have a multithermal composition. Similar studies by Horan (1970) lead to the same conclusion. These studies also suggest that it is desirable to correct for temporal variations before attempting to determine plasma parameters from OSO-4 spectrometer scans.

III.8 SUMMARY

In this chapter the theory and operation of OGO-4 broad band detectors and OSO-4 Bragg crystal spectrometers are reviewed. The methods developed by Horan and Meekins to analyse the data are also reviewed. The main points to be noted are:

(1) The observed broad band detector fluxes are processed under a gray body approximation at selected colour temperatures.

(2) These gray body based fluxes can be expressed as thermal continuum (free-free + free-bound) based fluxes or as continuum plus line emission based fluxes by the use of the appropriate conversion factors.

(3) The temperature and emission measure of the flare plasma can be determined from the ratios of fluxes in 0 - 3 Å and 1 - 8 Å bands; these are also based on the spectral assumptions mentioned above (the differences will be discussed in Figure V-3).

(4) OSO-4 flare scans show that most of the incident flux between 0.7 and 8.5 Å is in the form of continuum emission.

(5) Many of the spectral lines have been identified (Meekins et al., 1970) as due to Lyman lines of H-like ions and resonance lines of He-like ions. Similar line lists have also been compiled by Walker and Rugge (1970); Neupert (1971) and by Doschek (1972); Doschek's list will be used for comparison with the OSO-4 line list obtained in this thesis (Table IV-4).

(6) Studies based on uncorrected spectrometer data have shown that the electron temperatures determined from the scans are inconsistent with those determined from OGO-4 data.

CHAPTER IV

SPECTROMETER CALIBRATION AND ANALYSIS OF FLARE SPECTRA

IV.1 EXPERIMENTAL CALIBRATION OF THE LiF SPECTROMETER

The calculation of the theoretical calibration parameter Q was discussed in section III.6. It was defined by the product

$$Q = R_m(\lambda)\ \epsilon(\lambda)\ T(\lambda)\ 2d \cos \theta \tag{IV.1}$$

where $R_m(\lambda)$ is the theoretical integrated reflectivity of the crystal (discussed in Appendix B), $\epsilon(\lambda)$ is the efficiency of the Geiger counter, $T(\lambda)$ is the transmission coefficient of the aluminum coated mylar filter, and $2d \cos \theta$ is the wavelength dispersion parameter of the crystal. It was also pointed out that the integrated reflectivity of a real crystal has to be experimentally measured and that the detector efficiency was subject to uncertainties in the composition of the mica window. The latter problem is quite serious in the case of the silicon absorption edge. It happens that the forbidden line of Si XIII (λ = 6.747 Å) falls just beyond the absorption edge at 6.74 Å. Thus this line appears with a higher intensity than that of the resonance line of Si XIII (λ = 6.650 Å) in all OSO-4 scans (see Figure III-11). Doschek and Meekins (1970) found that this situation remained even after applying equation (IV.1); it was contrary to the observations of other investigators that the intensity of the forbidden line was always less than that of the resonance line of Si XIII (Walker and Rugge, 1971). Hence Doschek and Meekins (1973) felt that the detector efficiency should be experimentally measured. This has now been carried out for 1 to 3.8 Å by the author at NRL as described below. The filter transmission was also calculated. The measured values of LiF crystal reflectivities were kindly provided by Meekins.

TRANSMISSION OF THE FILTER, $T(\lambda)$

The probability $T(\lambda)$ of photon transmission by the aluminum coated Mylar filter is calculated from

$$T(\lambda) = \exp\left(-\sum \mu_m \rho x\right) \qquad \text{(IV.2)}$$

where μ_m is the mass absorption coefficient ($cm^2\ gm^{-1}$) of an element and ρx is the area density ($gm\ cm^{-2}$) of the element. Their product is summed over all the elements (C, H, O and Al) present in the filter material. The mass absorption coefficients are taken from the tables of McMaster et al. (1969) and can be expressed as a polynomial in $\ln \lambda$ as

$$\ln \mu_m = \sum_{k=0}^{4} a_k (\ln \lambda)^k \qquad \text{(IV.3)}$$

where the five coefficients a_k are calculated for all elements present in the filter (also Geiger counter) and are listed in Table IV-1. These were determined by a least-squares polynomial fit to equation (IV.3). The area

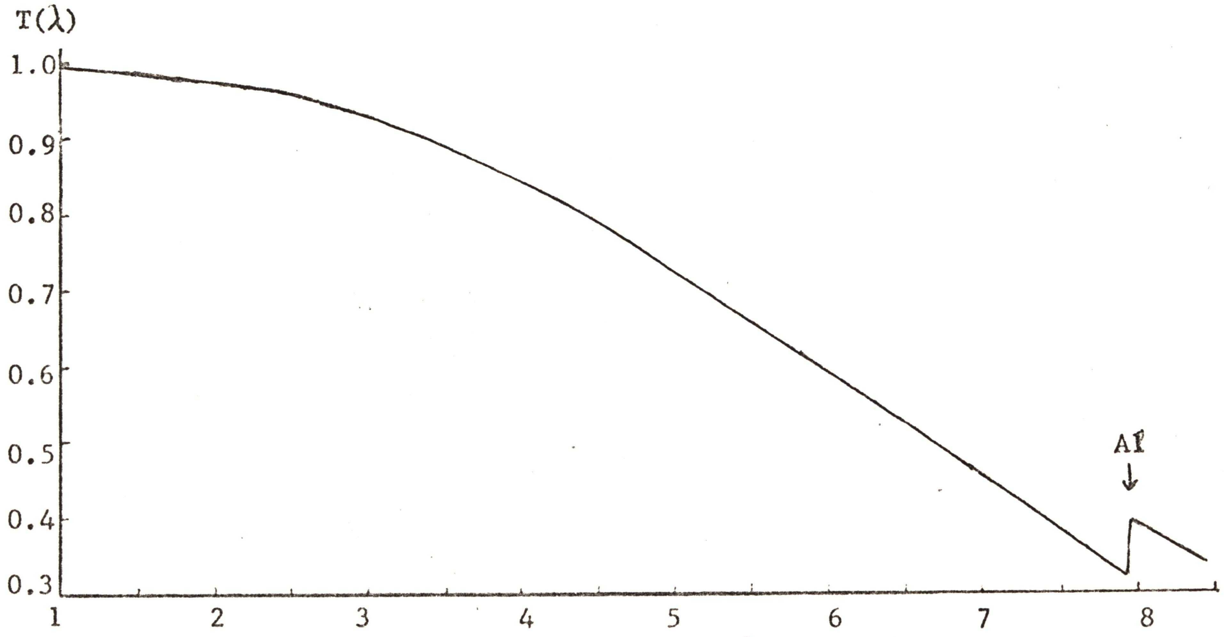

Figure IV-1. Transmission vs λ of the aluminum coated Mylar filter which shields the OSO-4 spectrometer. The absorption edge at 7.952 Å is due to aluminum.

TABLE IV-1

POLYNOMIAL COEFFICIENTS RELATING $\ell n \, \mu_m$ TO $\ell n \, \lambda$ *

Element	Validity From(Å)	To(Å)	a_0	a_1	a_2	a_3	a_4
Hydrogen	0.100	12.400	-0.9370	-0.0085	-0.1971	0.3107	-0.0185
Carbon	0.100	12.400	0.1906	2.6482	0.6575	-0.3369	0.0511
Oxygen	0.100	12.400	1.0968	2.9135	0.2886	-0.1829	0.0274
Magnesium	0.100	9.500	2.4044	3.0129	0.0187	-0.0845	0.0106
Aluminum	0.100	7.952	2.6289	2.9754	0.0264	-0.0991	0.0177
	7.952	44.000	-7.5580	10.8800	-2.7630	0.2972	0.0000 #
Silicon	0.100	6.745	2.8954	2.9859	-0.0139	-0.0956	0.0173
	6.745	12.400	0.7130	2.6493	0.0000	0.0000	0.0000
Argon	0.100	3.871	3.5390	2.8690	0.0000	0.0000	0.0000 #
	3.871	43.192	3.7350	-2.0330	3.3120	-0.9724	0.0996 #
Potassium	0.000	3.437	3.7805	2.8775	-0.1112	-0.0633	0.0107
	3.437	12.400	1.3296	3.0181	-0.0955	0.0000	0.0000
Iron	0.100	1.743	4.5766	2.7133	-0.1567	-0.0450	0.0041
	1.743	12.400	2.3092	3.0242	-0.1231	0.0000	0.0000
Bromine	0.100	0.920	5.1601	2.4119	-0.1819	0.0000	0.0000
	0.920	6.957	3.3106	2.7940	-0.0352	-0.0123	0.0003
	6.957	7.767	3.4810	2.5091	0.0000	0.0000	0.0000
	7.767	7.997	3.1277	2.5140	0.0000	0.0000	0.0000
	7.997	12.400	1.9163	2.3671	0.0000	0.0000	0.0000

These values were taken from Horan (1970).

* Wavelengths are in Ångström units; μ_m's are in $cm^2 \, g^{-1}$.

density of each element present in Mylar ($C_{10}H_8O_4$, total area density = 0.84 mg cm^{-2}) is given by the product of the relative atomic weight of the element in the molecule (e.g., 10 C/(10 C + 8 H + 4 O) for carbon) and the total area density of Mylar. The graph of T(λ) calculated from equation (IV.1) is shown in Figure IV-1. The aluminum coating in the filter produces the absorption edge at 7.952 Å in the diagram.

INTEGRATED REFLECTIVITY R(n, λ) - Experimental Measurement

Meekins (1973) has determined the integrated reflectivity of a lithium fluoride crystal sample similar to the one used in OSO-4, using the double crystal spectrometer technique described in Appendix B. These reflectivities, which are for unpolarized x-radiation, have been determined up to n = 4 orders of diffraction and are shown in Figure IV-2. It can be seen that as the value of n increases, R(n,λ) have been determined for wavelengths up to λ_{max}/n where $\lambda_{max} \approx 4$ Å for LiF spectrometer. It can also be seen that the higher order reflectivities are less than 20 per cent of R(1, λ). The integrated reflectivity of the EDDT crystal used in OSO-4 is yet to be determined (Meekins, private communication).

EFFICIENCY OF GEIGER COUNTERS, $\epsilon(\lambda)$

The efficiencies of two sample tubes 1186 and 1176 belonging to the same batch as those used in the OSO-4 spectrometers were determined at the Naval Research Laboratory. Using the method developed by Meekins (1973), the author and Unzicker determined the efficiencies covering the spectral range of the LiF spectrometer (0.7 - 3.8 Å). They were subsequently determined for higher wavelengths upto 8.5 Å (Meekins and Unzicker, private communications).

The experimental arrangement used to determine the detector efficiency for any wavelength λ is shown in Figure IV-3.

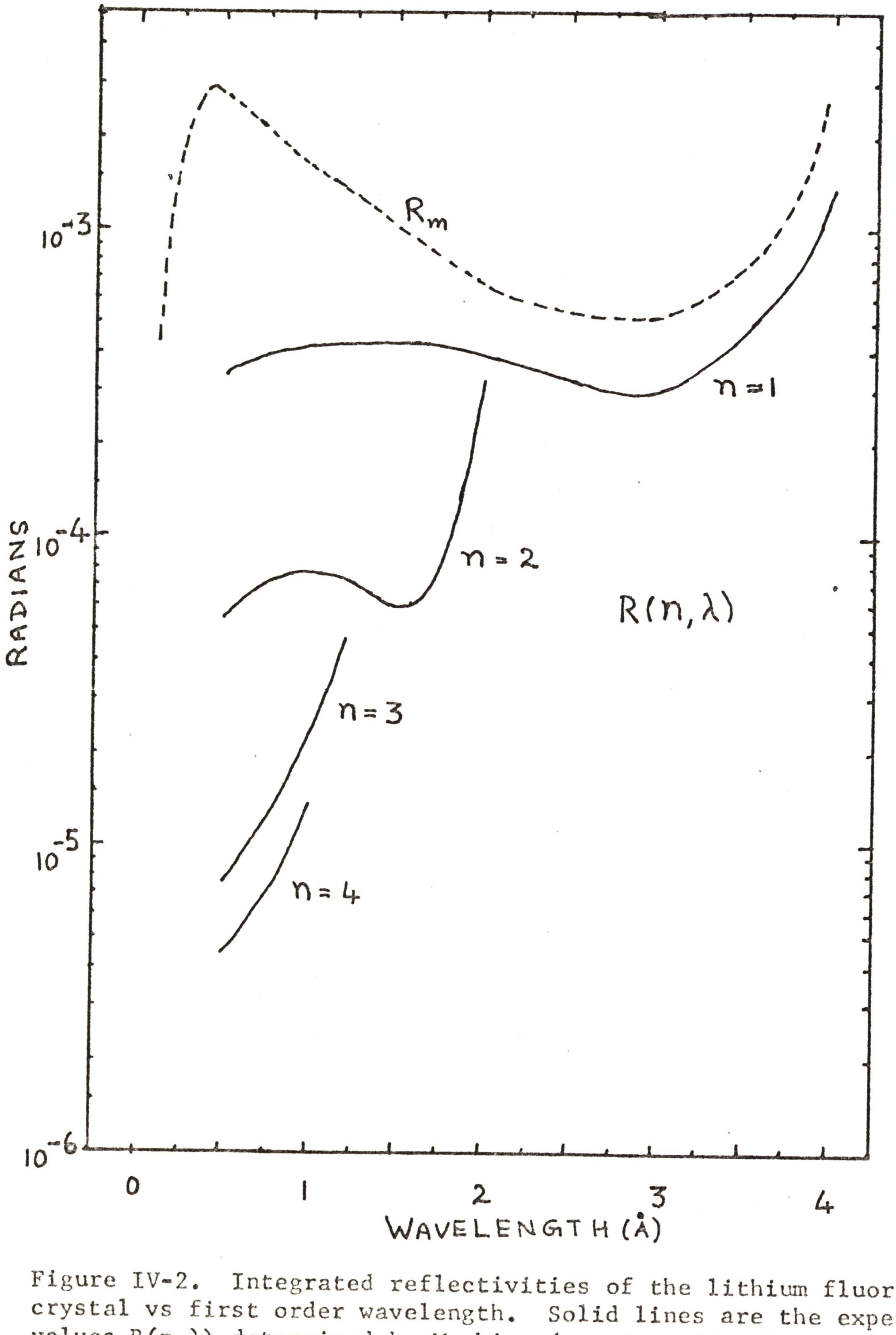

Figure IV-2. Integrated reflectivities of the lithium fluoride crystal vs first order wavelength. Solid lines are the experimental values R(n,λ) determined by Meekins (see Appendix B); dashed line is the calculated value assuming a mosaic crystal structure.

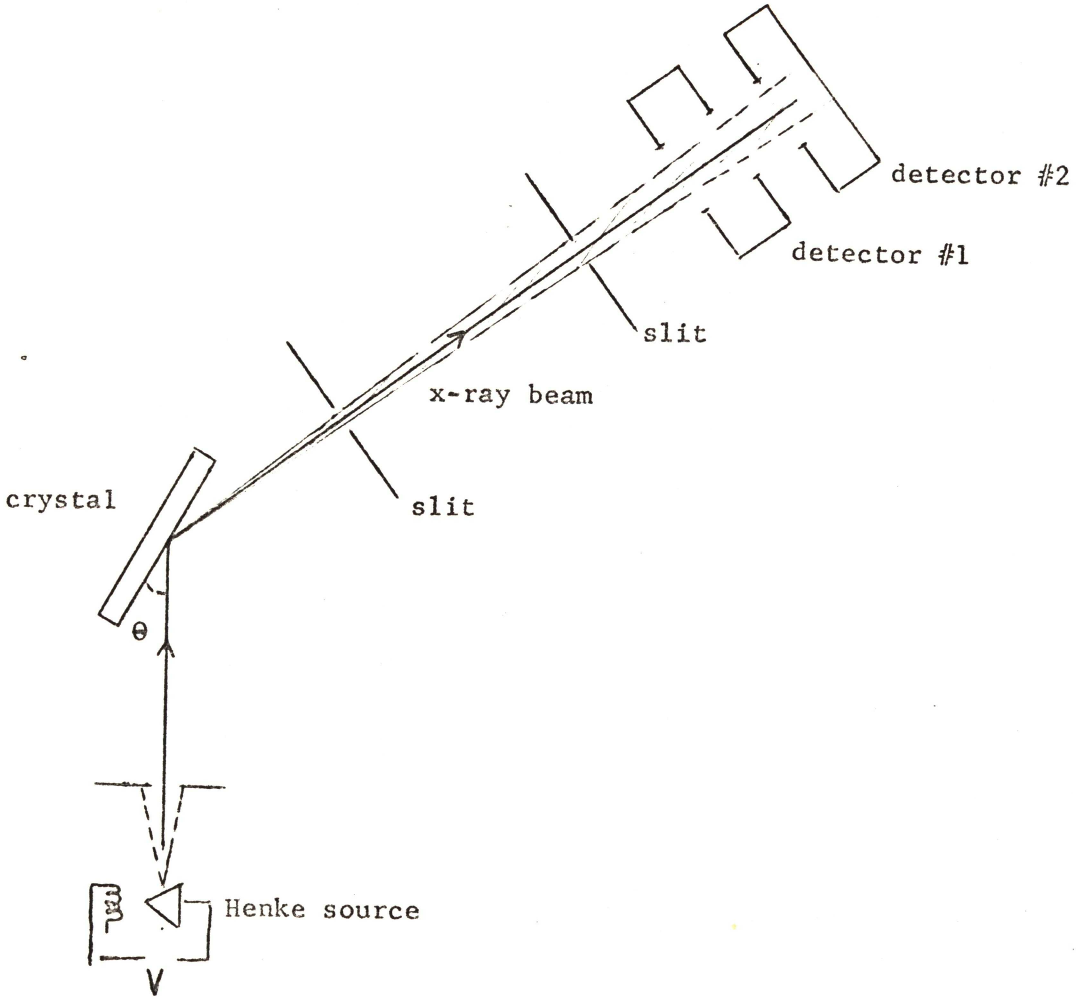

Figure IV-3. Schematic of the double detector arrangement used to find the quantum efficiency of the Geiger counter (#2). The entire set up is enclosed in a vacuum chamber.

A narrow x-ray beam is incident on a LiF crystal at a selected Bragg angle θ so that the first order continuum radiation of wavelength λ is diffracted. The diffracted beam passes successively through two narrow, rectangular defining slits and a double window proportional counter (#1) before reaching the Geiger counter (#2) under test. The windows of the detectors are large enough to allow the entire x-ray beam to pass through so that no geometrical corrections are necessary. The detector #1, which is gas filled and has two identical Mylar windows, is used to calibrate the x-ray beam incident on the Geiger counter in the following manner:

(1) With detector #1 removed from the beam, the counting rate R_{12} of detector #2 is determined (the final subscript digit of R refers to the detector whose counting rate is taken).

(2) With detector #1 in the beam, but with no fill gas in it, the counting rate R_{22} is determined.

(3) Then, with detector #1 in the beam and with its fill gas (90% argon + 10% methane), the counting rate R_{32} is determined.

(4) Finally, the counting rate R_{41} of detector #1 itself is determined.

These counting rates were measured subject to one per cent statistics, and were obtained for selected wavelengths that were known to an accuracy of ± 0.01 Å. The theory that relates these counting rates to the required quantum efficiency $\epsilon(\lambda)$ of the test detector #2 is as follows:

Let

I_o = intensity of the x-ray beam before it enters the window of the calibration detector #1,

T_M = transmission of each window of detector #1,

T_F = transmission of the fill gas in detector #1.

Then from the four experimental steps described above the following relations are obtained:

From (1), $R_{12} = I_o\, \epsilon(\lambda)$,

from (2), $R_{22} = I_o\, (T_M)^2\, \epsilon(\lambda)$,

from (3), $R_{32} = I_o\, T_M\, T_F\, T_M\, \epsilon(\lambda)$,

and from (4), $R_{41} = I_o\, T_M\, (1 - T_F)$,

where the product $T_M\,(1 - T_F)$ represents the efficiency of detector #1.

The above equations can be solved to yield

$$\epsilon(\lambda) = \frac{R_{12}}{R_{41}} \left(\frac{R_{22}}{R_{12}} \right)^{\frac{1}{2}} \left[1 - \frac{R_{32}}{R_{22}} \right] \qquad \text{(IV.4)}$$

In order to improve the continuity, graphs of T_M and T_F were first drawn as a function of λ and the smoothed values were used in equation (IV.4) to obtain the quantum efficiencies for detectors #1186 and #1176. These are shown in Figure IV-4. It is seen that the two sample tubes consistently differ in their efficiencies between 1 and 3.8 Å. Both show a complicated but small edge effect at the short wavelength side of the potassium absorption edge (3.43 Å). Comparison of differences in the range 3.9 - 8.5 Å cannot be made because one of the tubes (#1186) broke down. However, due to the fact that the chemical composition of the mica window slightly varies from sample to sample even in the same ore variety, it is possible that the efficiencies of the Geiger counters used aboard OSO-4 may be slightly different.

THEORETICAL EFFICIENCY

It would be of interest to compare the experimental values with the calculated values. The theoretical efficiency is calculated from the expression

$$\epsilon(\lambda) = T_w(\lambda) \left[1 - T_g(\lambda) \right] \qquad \text{(IV.5)}$$

where the transmission of the mica window is given by

$$T_w(\lambda) = \exp(-\sum \mu_m \rho x)_w \qquad \text{(IV.6a)}$$

and the transmission of the fill gas in the Geiger counter is given by

$$T_g(\lambda) = \exp(-\sum \mu_m \rho x)_g \qquad \text{(IV.6b)}$$

where the subscripts w and g refer to the window and the gas respectively. The factor $1 - T_g(\lambda)$ gives the photon absorption probability by the gas.

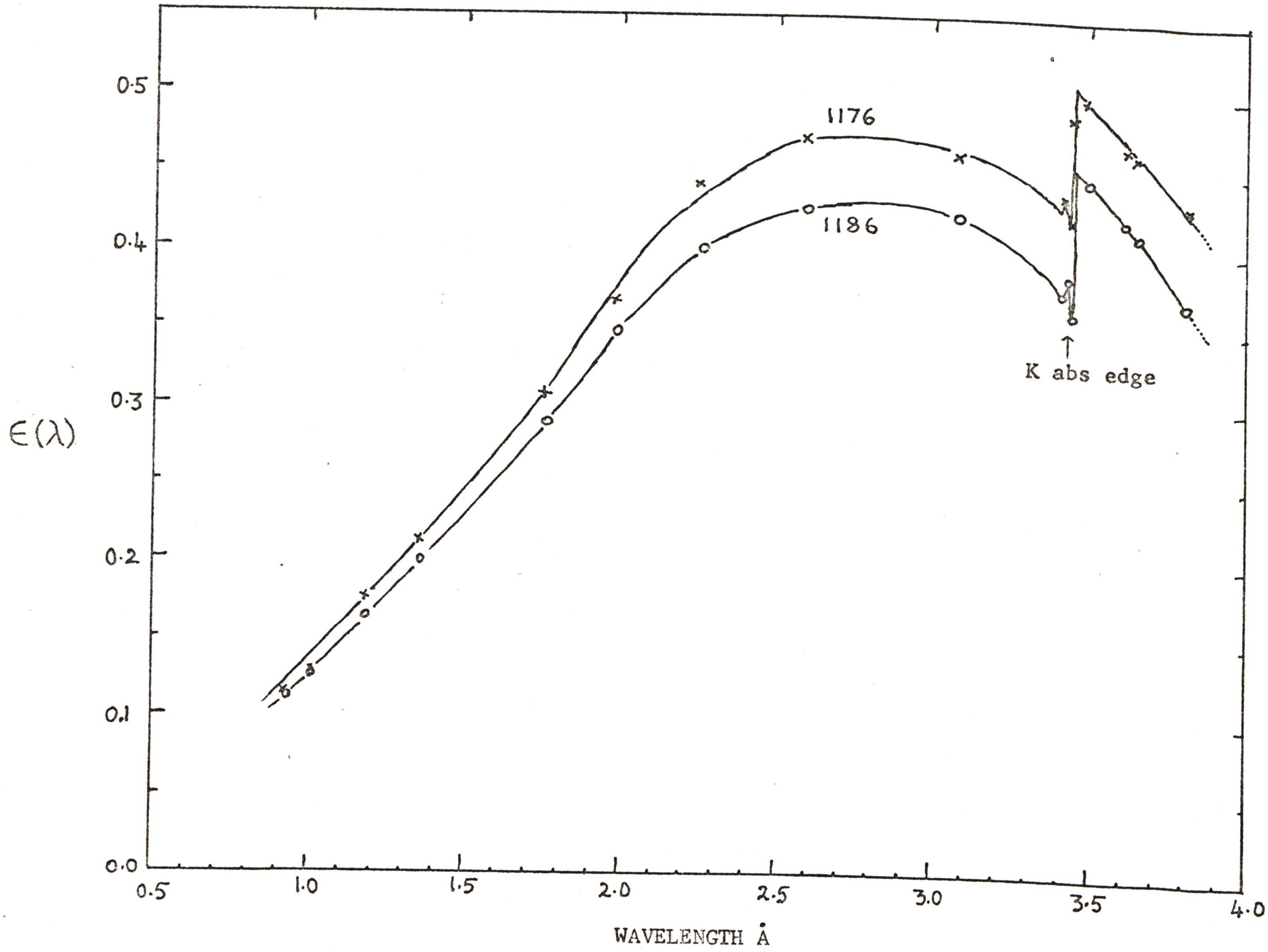

Figure IV-4. Experimental values of quantum efficiencies of the Geiger counters #1186 and #1176 similar to those used in OSO-4 spectrometers.

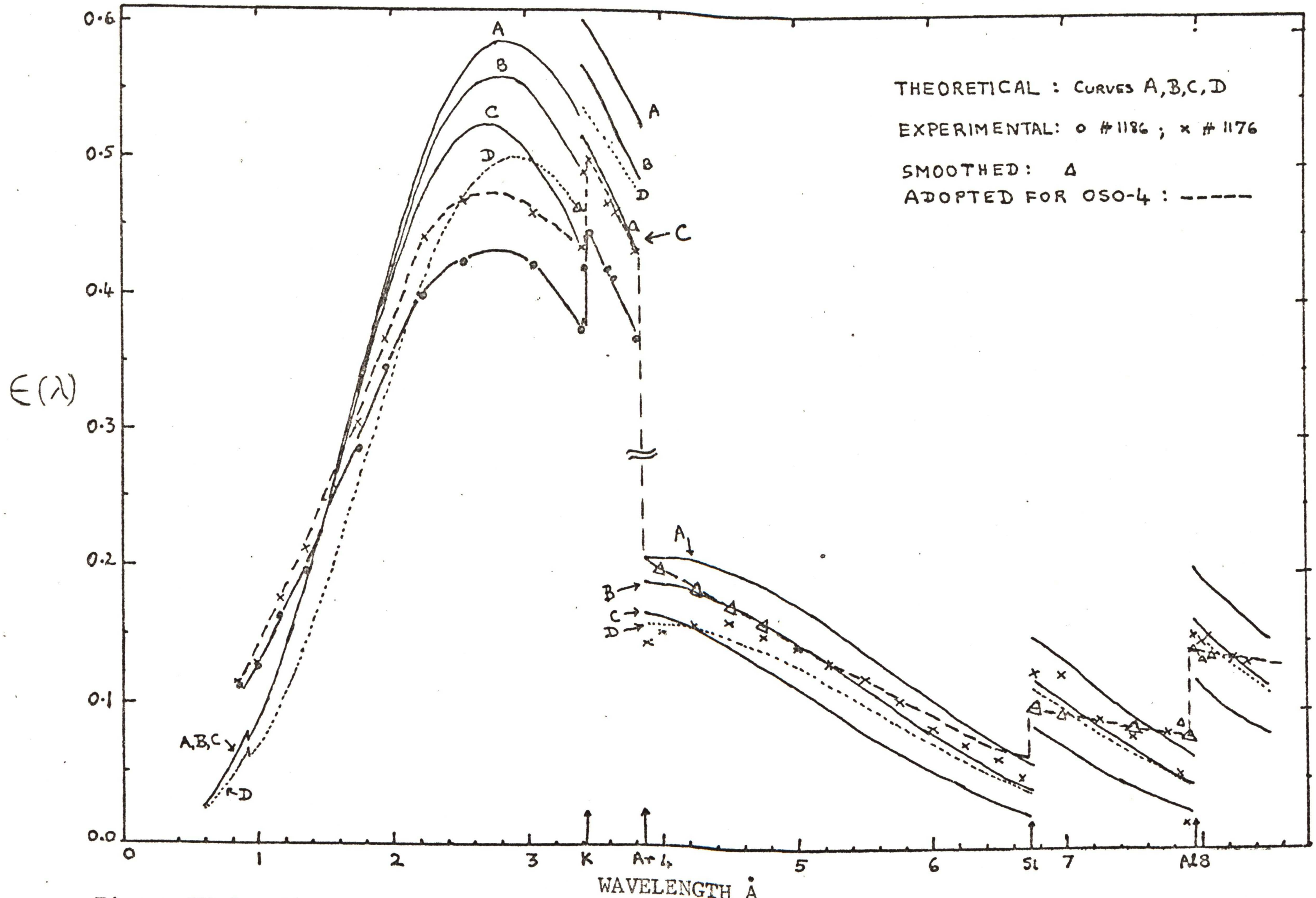

Figure IV-5. Theoretical efficiency curves (A, B, C, D) are compared with the experimental values of #1186 (●) and #1176 (x). Smoothed (Δ) and adopted values (---) are also shown (see text).

The product of μ_m, the mass absorption coefficient, and ρx, the area density of each element is summed over all the elements present in the window (mica, ruby India variety) or in the fill gas (argon + 1% bromine).

The chemical composition of the Indian ruby mica is taken from Skow (1962) to be SiO_2 (~46%) + Al_2O_3 (~36%) + K_2O (~10.5%) + H_2O (4.5%) + Fe_2O_3 (1.25%) + FeO (0.75%) + MgO (1.0%) + trace of other elements. Broken down by elements, their relative fraction by weight (in brackets) is O (0.482) + Si (0.215) + Al (0.190) + K (0.087) + Fe (0.015) + Mg (0.006) + H (0.005). The values in brackets are multiplied by the estimated total area density of the window to get the individual area density of each element. The mass absorption coefficient of each element is calculated from equation (IV.3). Then $T_w(\lambda)$ and $T_g(\lambda)$ are calculated taking the area densities of argon and bromine to be 2.58 and 0.104 mg cm^{-2} respectively. The theoretical efficiencies are now obtained from equation (IV.5) and are plotted in Figure IV-5 for three values of mica window thickness corresponding to 1.5, 1.7 and 2.0 mg cm^{-2} (curves A, B and C respectively). It is seen that the theoretical efficiency curve B with a window thickness of 1.7 mg cm^{-2} has closest agreement with the experimental values except near potassium and argon absorption edges. Even here the agreement improves if the amount of argon is reduced by 25 per cent (new $\rho x = 1.94$ mg cm^{-2}) and the curve D is plotted as shown. This suggests that the amount of argon in the Geiger counter may have been overestimated. However, perfect agreement is difficult to achieve if the composition given by Skow (1962) is adopted. Kreplin and Meekins (1973) also arrived at similar conclusions concerning OSO-6 detectors.

SOLAR FLARE CALIBRATION OF $\epsilon(\lambda)$

The experimental values of $\epsilon(\lambda)$ can be improved to match those of

OSO-4 detectors by using the observed solar continuum flux. This can be done by assuming that the continuum has no significant discontinuities other than the instrumental absorption edges. For this purpose an EDDT scan of the 3b flare shown in Figure III-11 is taken. A smooth curve is drawn to represent the observed continuum and the raw counting rate r_c is read off at intervals of 0.2 A between 2 Å and 8.4 Å. Then the following quantities are calculated and plotted in Figure IV-6:

Curve 1: Instrumental geometry corrections are applied to r_c by calculating $r_c \div (A' \ 2d \cos\theta)$ where A' is the effective area (see Figure III-12) and 2d cosθ is the dispersion factor.

Curve 2: Filter transmission $T(\lambda)$ and detector efficiency $\epsilon(\lambda)$ corrections are applied to the quantity in curve 1, by

$$[\text{curve } 1] \div [T(\lambda) \cdot \epsilon(\lambda)]$$

Separate calculations are made by taking the quantum efficiencies of #1186 (upto 3.8 Å) and #1176 respectively. As the integrated reflectivities of the EDDT crystal have not been determined, they are omitted in this calculation, but they are assumed to be continuous with respect to λ. This omission, therefore, is not expected to seriously affect the conclusions based on Curve 2. It is seen in Figure IV-6 that discontinuities do remain at the Ar, Si and Al absorption edges. When these are smoothed out it becomes apparent that the efficiency of 1176 fits the data better. The new efficiencies are calculated by adopting the smoothed values at the absorption edges and these are also indicated (dashed line) in Figure IV-5. Similar analysis is not possible for the LiF spectrometer detector because of its restricted wavelength range. It is concluded that the experimentally determined efficiency from 1 Å to 3.8 Å of detector #1176, and the smoothed efficiency from 3.9 Å to 8.5 Å, may be adopted for the calculation of

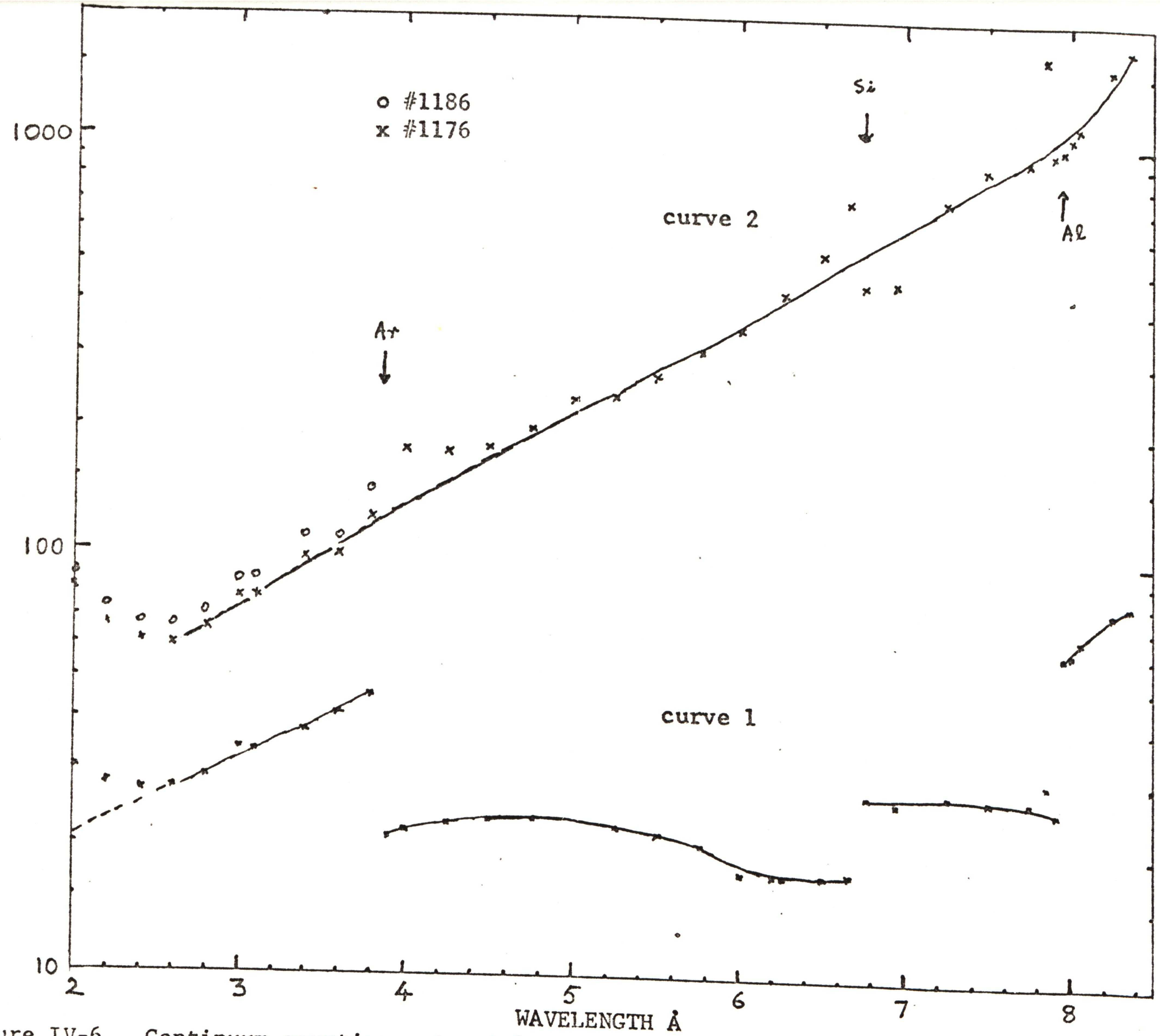

Figure IV-6. Continuum counting rates taken from an EDDT scan are corrected for geometry in curve 1 and then for the filter transmission as well as for the experimental values of $\epsilon(\lambda)$(of #1176 and #1186) in curve 2. A line was drawn to smooth the absorption edges and determine smoothed $\epsilon(\lambda)$(see text).

the OSO-4 spectrometer calibration parameters. This will be done below for the spectral range of the LiF crystal spectrometer.

FINAL CALIBRATION PARAMETERS

Since all the required instrumental parameters for the LiF spectrometer are determined, it is now possible to write down the experimental calibration parameters. Before doing this, it is worthwhile to consider Bragg's law again. According to this law, x-rays of wavelength λ will be diffracted in the first order at an angle θ such that

$$\theta = \sin^{-1} (\lambda / 2d).$$

The same angle also corresponds to higher orders of diffraction for lower wavelengths such that

$$\theta = \sin^{-1}\left(\frac{1}{2d}\lambda\right) = \sin^{-1}\left(\frac{2}{2d}\,\frac{\lambda}{2}\right) = \ldots\ldots\ldots = \sin^{-1}\left(\frac{n}{2d}\,\frac{\lambda}{n}\right)$$

where λ/n cannot be less than the lower limit of the spectral range of the instrument. As an example, in the LiF spectrometer scan, the counting rate at 3.6 Å will have second order contributions from the radiation of 1.8 Å, third order contributions from 1.2 Å, and fourth order contributions from 0.9 Å, all of which are covered by the spectral range of the instrument. The true counting rate $r_p(\lambda)$ of the continuum flux at the first order wavelength λ, is then given by the sum all contributions (from $\lambda, \frac{\lambda}{2}, \frac{\lambda}{3}, \ldots$):

$$r_p(\lambda) = A'(\theta) \sum_n R(n, \tfrac{\lambda}{n})\, \epsilon(\lambda)\, T(\tfrac{\lambda}{n})\, \frac{2d \cos\theta}{n}\, I(\tfrac{\lambda}{n}) \qquad \text{(IV.7)}$$

where

$\lambda = 2d \sin\theta$, the <u>wavelength</u> at which $r_p(\lambda)$ is <u>read from the scan</u>,

$A'(\theta)$ = effective collecting area of the detector which depends on θ,

$\epsilon(\lambda)$ = quantum efficiency of detector #1176 for the LiF spectrometer,

$I(\frac{\lambda}{n})$ = incident photons ($cm^{-2}\ sec^{-1}\ Å^{-1}$) at wavelength λ/n,

$T(\frac{\lambda}{n})$ = Filter transmission corresponding to the value of $\frac{\lambda}{n}$ (Figure IV-1),

$R\left(n, \frac{\lambda}{n}\right) \equiv R(n, \lambda)$ the integral reflectivity of order n (Figure IV-2), redefined here so that λ corresponds to nth order diffraction of first order radiation at $\frac{\lambda}{n}$.

This expression is summed over all orders of diffraction n. Obviously this expression is quite complicated enough, even if the entire spectrum (0.7 to 3.8 Å) had been obtained by an "instantaneous" scan. In that case $I(\frac{\lambda}{n})$ could easily have been estimated from the counting rate at $\frac{\lambda}{n}$ for use in equation (IV.7), so that the higher order contributions could be subtracted from it and the first order intensity be determined. Unfortunately, OSO-4 spectrometers require 14 minutes to complete one scan. During this period, considerable changes in the flare plasma parameters occur as can be seen in Figure III-8. Therefore, depending on the position of the wavelength (or step number) and the direction of scan, the value of $I(\frac{\lambda}{n})$ actually scanned at $\frac{\lambda}{n}$ is different from the required value when the wavelength λ is being scanned. Thus the observed data should be corrected for temporal variations before being used in equation (IV.7). The possibility of this procedure depends on the availability of simultaneous observations by OGO-4 or other satellites.

Fortunately a glance at the curves of $R(n,\frac{\lambda}{n})$ (Figure IV-2) suggests that the higher order reflectivities do not generally exceed 20 per cent of first order reflectivities. Hence, in the analysis of LiF spectrometer data, the higher order corrections will be neglected in this thesis.

Considering only the first order spectrum, equation (IV.7) can be rewritten after omitting unnecessary terms as

$$r_p = A' \, Q(1, \lambda) \, I_\lambda \qquad \text{(IV.8)}$$

where I_λ = number of incident photons cm^{-2} sec^{-1} A^{-1},

and $$Q(1,\lambda) = R(1,\lambda)\,\epsilon(\lambda)\,T(\lambda)\,2d\cos\theta \qquad (IV.9)$$

is the experimental version of equation (IV.1). A graph of equation (IV.9) is shown in Figure IV-7, and its values are given in Table IV-2. It is seen that these are an order of magnitude larger than Meekins' (1972) theoretical values (also shown). Equation (IV.8) will be used in Chapter V to derive the continuum source spectrum I_λ from the LiF spectrometer scans.

IV.2 IDENTIFICATION OF SPECTRAL LINES

The flare spectra reveal a large number of prominent line features which show an increase in intensity as compared to quiet or non-flare spectra (see figures III-10 and -11). In the LiF spectra the prominent features are at 1.9 Å and 3.2 Å. In the EDDT crystal spectra the most prominent feature is the Lymanα line of Mg XII at 8.421 Å, followed by lines of H- and He-like ions of Ca, Ar, S, Si, and Aℓ. Many of these were identified by Meekins et al.,(1970). They identified a number of lines such as those between 8 and 8.4 Å as due to K shell x-ray lines of Aℓ (Table III-3). Doschek et al., (1972) showed from a study of OSO-6 spectra that these lines were due in part to lines of Li-like Fe XXIV. In addition to optical transitions weaker satellite lines to the H- and He-like lines have also been identified in spectra of flares and active regions. As discussed in section II.4, Gabriel (1972) published more accurate wavelengths of He-like ion lines and their Li-like satellites. In view of these developments a re-identification of the lines has now been made by summing a large number of spectrometer scans. This project is described below.

SUMMATION OF OSO-4 SPECTRA

While studying a large number of spectrometer scans it became clear that a number of weak features show up in flare spectra; but in many cases

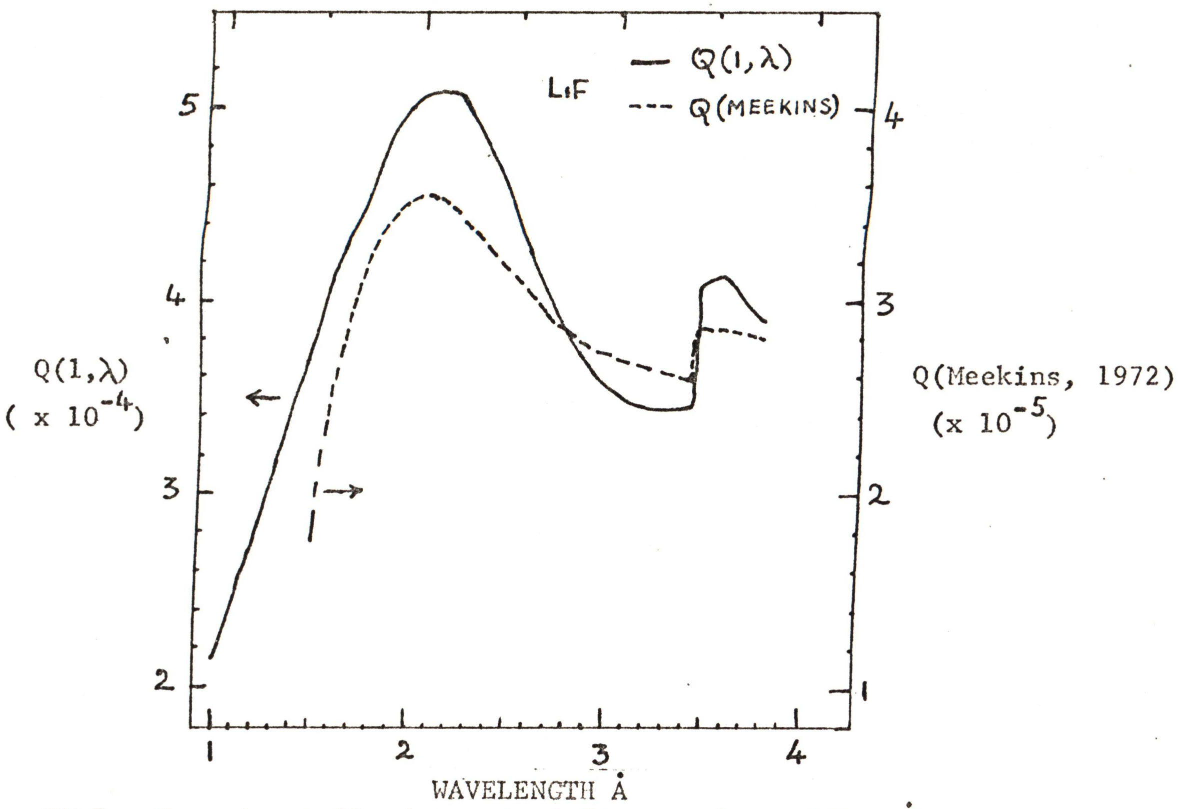

Figure IV-7. Experimentally determined first order calibration parameter is compared with its theoretical value (dashed line) for LiF spectrometer.

TABLE IV-2

OSO-4 LiF CALIBRATION PARAMETER Q(1, λ)

(Å)	Q(1, λ)	(Å)	Q(1, λ)
1.0	2.16*	2.5	4.48*
1.1	2.49	2.6	4.26
1.2	2.83	2.7	4.05
1.3	3.18	2.8	3.77
1.4	3.52	2.9	3.67
1.5	3.84	3.0	3.53
1.6	4.15	3.1	3.47
1.7	4.43	3.2	3.44
1.8	4.72	3.3	3.45
1.9	4.87	3.4	3.43
2.0	5.10	3.5	4.09
2.1	5.05	3.6	4.13
2.2	5.08	3.7	3.90
2.3	4.90	3.8	3.87
2.4	4.75		

* This column should be multiplied by 10^{-4}

these features could not be distinguished from statistical fluctuations which are proportional to the square root of the counting rates. In order to improve the statistics of these features and at the same time reduce the noise in the continuum it was decided to classify the scans before summing. The classification into three groups was based on the intensity of Mg XII Lα line which showed considerable variations depending on the solar activity:

$$\left.\begin{array}{ll} \text{Group I:} & 100 - 350 \\ \text{Group II:} & 350 - 700 \\ \text{Group III:} & 700 - \text{saturation} \end{array}\right\} \text{counts in Mg XII L}\alpha\text{ line (8.421 Å)}$$

In selecting the scans, those with raster motions, with particle interference or with partial data were rejected. For instance, class 3b flare scans (Figures III-10 and -11), the largest ever observed by OSO-4 spectrometers, could not be included in the summation because of the raster motion. The selection of usable scans yielded 102 scans under group I, 41 scans under group II and 18 scans under group III. The Solar Geophysical Data bulletins (1968) indicated that, (1) group II scans covered sub-flares (class S), unconfirmed flares and cooling phases of class I flares, (2) group III scans covered class I flares; and, (3) group I covered mostly normal solar activity. Before summing each scan successively on the computer, correction was applied for the location of the flare on the solar disk by centering the peak of the Mg XII Lα line (see section III.6). The results of the summation, averaged separately for the number of scans included in each group, were plotted together for comparison. These are shown in Figures IV-8 and IV-9 for the LiF and EDDT spectra respectively. In these figures, the upper plot corresponds to group III scans; the middle plot corresponds to group II scans and the lower plot corresponds to group I scans. For convenience they will also be referred to as flare scans, sub-flare scans and quiet scans. The results for both crystal spectrometers in the region 1.5 - 4.0 Å are plotted on the same wavelength scale in Figure IV-10. These plots are not corrected for instrumental effects. Examination of the plots reveals the following:

(1) Reflection of x-rays: There is an apparent increase in the continuum counting rates at the low wavelength side of both spectrometer scans ($<$ 1.2 Å for LiF; $<$ 2.5 Å for EDDT). This is due to the fact that at small Bragg angles of incidence x-rays are not only diffracted but also reflected directly. Thus in this region the real magnitude of the spectral continuum is masked.

(2) Statistical fluctuations: The statistical fluctuations are minimized as expected, and depend on the number of scans involved in each group. They increase gradually from the quiet to flare plots. Also, it can be seen that weak features and lines are strengthened. For instance, in Figure IV-8, the weak calcium feature at 3.2 Å stands out in the quiet scan; the weak potassium feature stands out near 3.5 Å in the sub-flare scan. In Figure IV-8, this strengthening of weak features is clearly evident. The faint but unmistakable presence of many identified lines can be noticed in the quiet scan. A few examples of this in the flare scan are the L β line of Al at 6.05 Å, L δ line of Mg at 6.58 Å and a feature at 6.8 Å just beyond the absorption edge of silicon at 6.74 Å.

(3) Evolution of lines: The influence of solar activity on the existence and evolution of lines can also be noticed. Lines of H-like and He-like ions of Mg, Al, Si, are present in quiet scans but greatly increase in intensity as the activity becomes hotter in the flare scans; lines of He-like ions of Ca, Ar, and S increase in intensity in flare scans; a group of lines

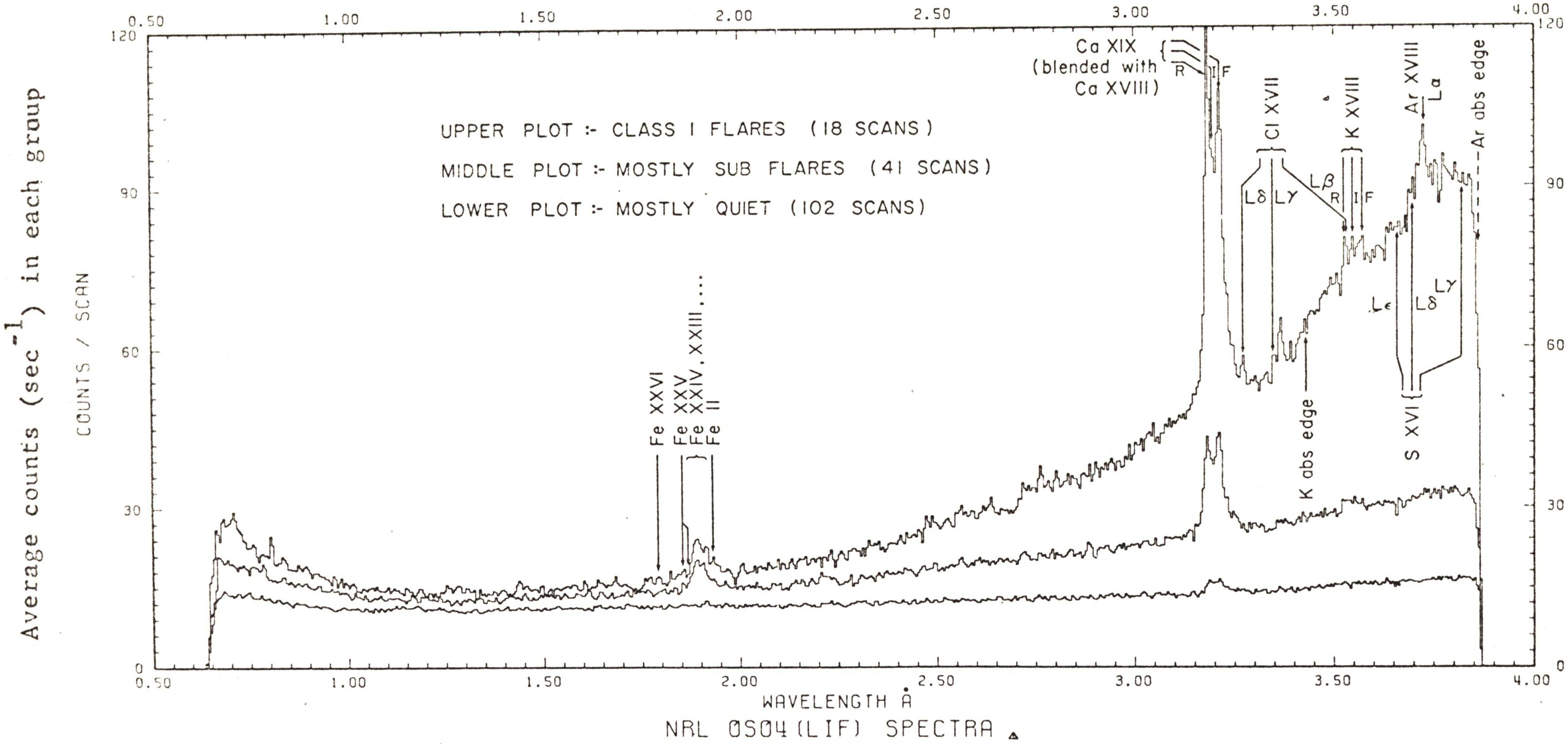

Figure IV-8. Summed and averaged spectra from LiF spectrometer scans of the quiet and flaring sun. See Table IV-4 for details of line identifications, and p 98 for a discussion of the identification of Lγ of Cl XVII.

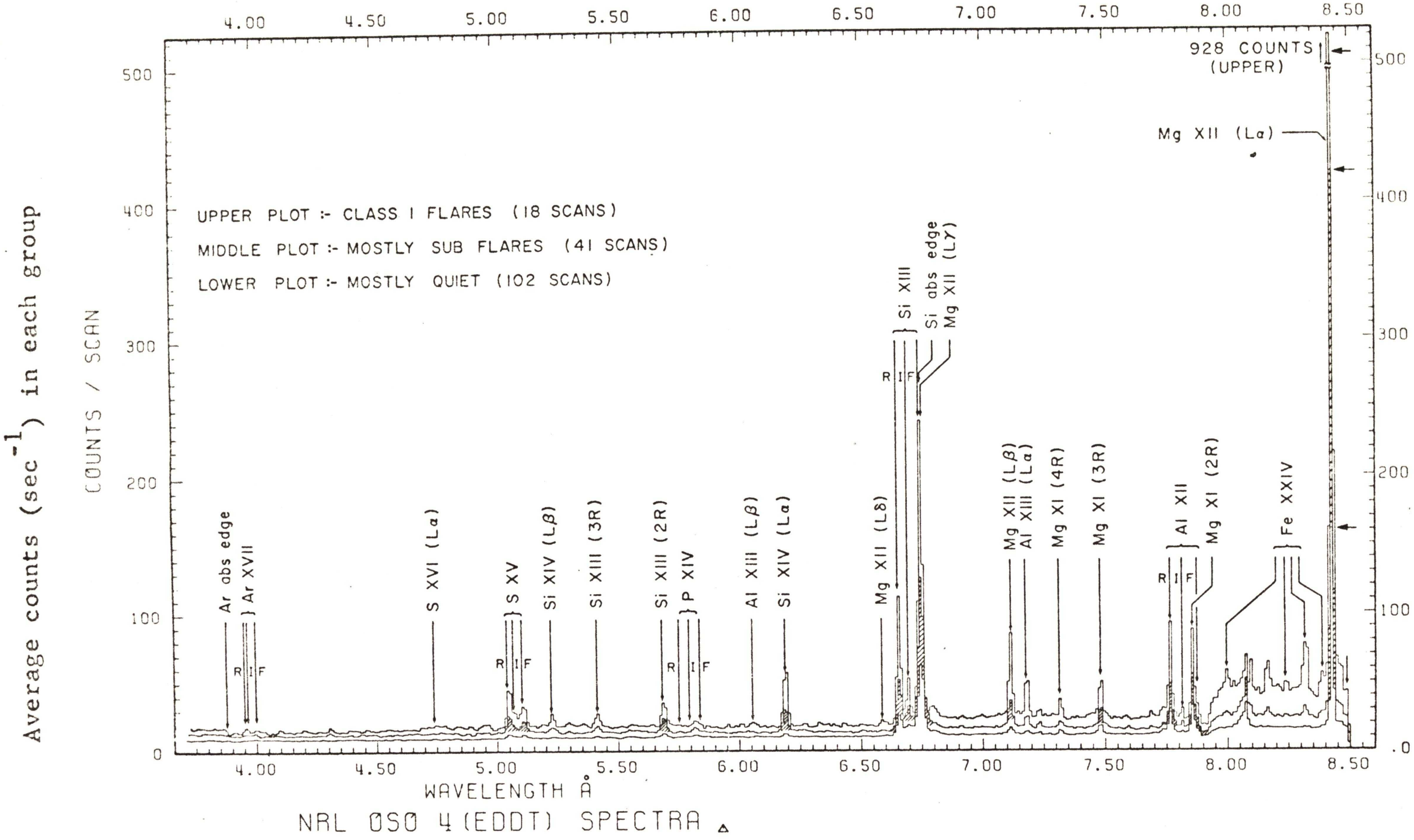

Figure IV-9. Summed and averaged spectra from EDDT spectrometer scans of the quiet and flaring sun. When there is an overlap of lines, those belonging to the middle scan are shaded to indicate their magnitudes. See Table IV-4 for details of line identifications.

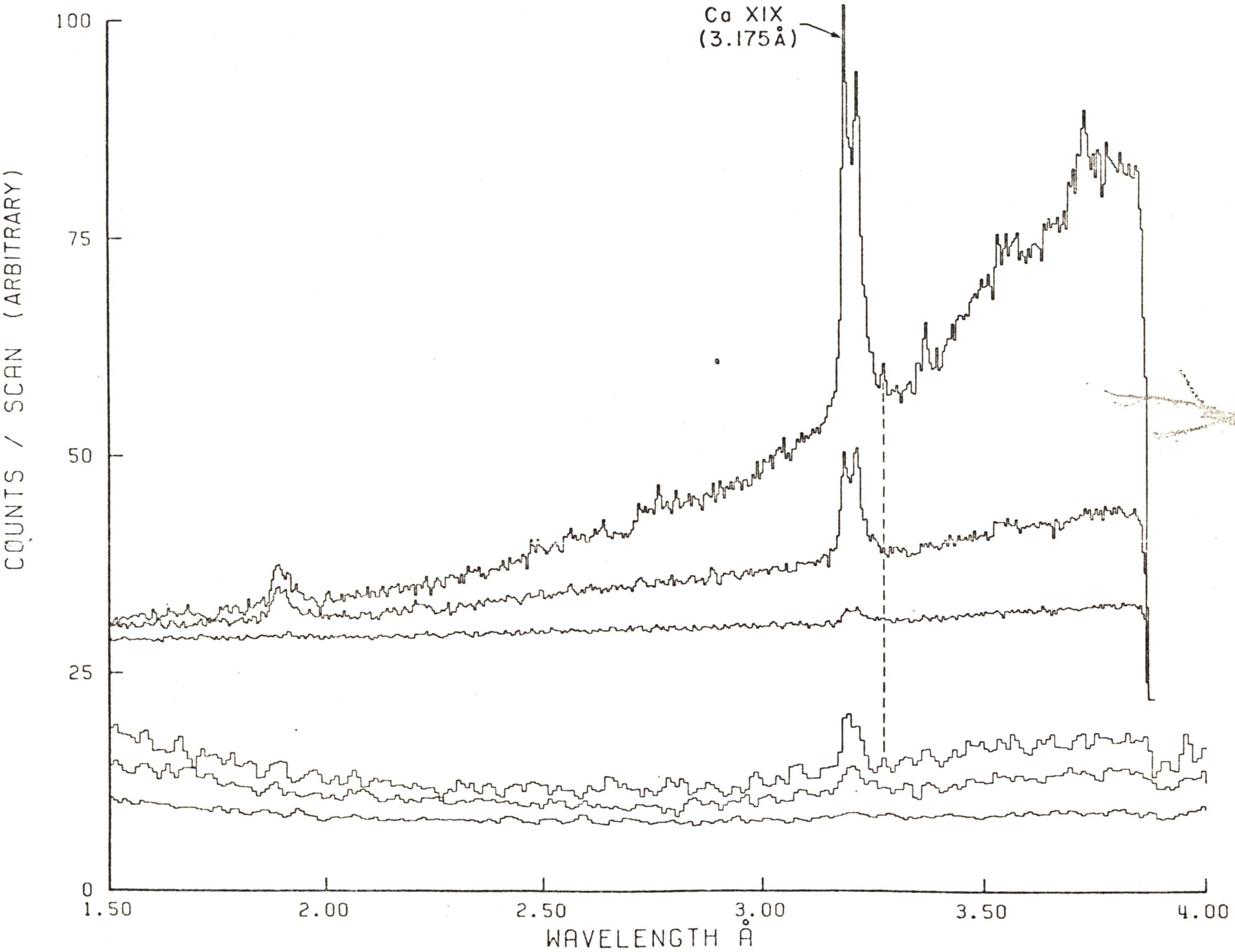

Figure IV-10. The spectral portion common to both LiF and EDDT spectrometers is plotted on the same wavelength scale. The three lower scans are from Fig. IV-9 and the three upper scans are from Fig. IV-8. The vertical line identifies the chlorine Lδ line at 3.27 Å present in the upper scans of both crystals. Many such coincidences can be seen throughout the spectral range.

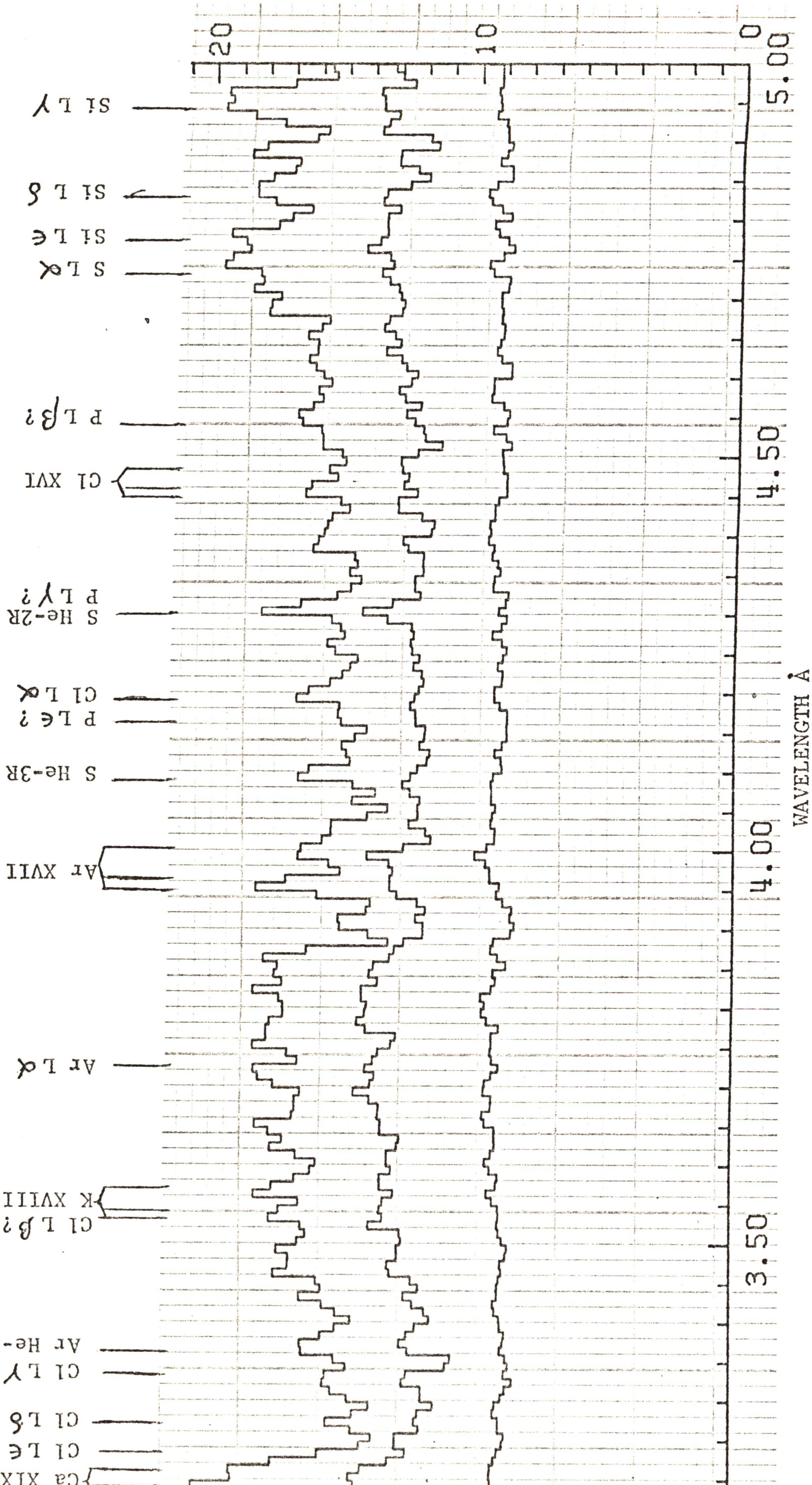

Figure IV-11. An enlarged section of the summed spectra from Fig. IV-9 showing lines of Cl and P.

between 8.0 and 8.4 Å are not present in quiet scans but appear with increasing intensity in sub-flare and flare scans, indicating that these are due to ions that exist only during flares.

(4) Absorption edges: The potassium absorption edge at 3.43 Å is quite weak and is apparent only in the LiF flare scan in Figure IV-8. A line like feature (marked by arrow) at that position is explained as due to a small jump observed in the experimental efficiency curves shown in Figure IV-4. The absorption edges of argon, silicon and aluminum are clearly evident through changes in the continuum levels. The forbidden line of Si XIII unfortunately falls right after the silicon absorption edge and therefore it appears much more intense than the resonance line of Si XIII at 6.65 Å. In addition the forbidden line is also blended by contributions from Lγ line of Mg.

IDENTIFICATION OF LINES

The identification of lines is based on the following guidelines adopted by other investigators (e.g., Doschek, 1972):

(1) Theoretical and extrapolated wavelength coincidences with observed lines

(2) Expectation of the transition based on element abundance, electron temperature and flux variations during the evolution of the flare.

(3) Consistency with available laboratory observations.

(4) Observation of several lines in each series.

(5) It is necessary to estimate the magnitude of the expected statistical fluctuation in order to determine what is a line and what is not. To do this, assume that N is the number of scans (data points) summed and $\bar{r}$ is the <u>average</u> counts per scan (at any λ) plotted in Figures IV-8 and IV-9. Then the uncertainty in the mean, $\bar{r}$, can be shown (see any text on error

analysis, e.g., Bevington, 1969) to be

$$\sigma_{\bar{r}} = (\bar{r}/N)^{\frac{1}{2}}$$

The values of $\sigma_{\bar{r}}$ and $2\sigma_{\bar{r}}$ for typical values of $\bar{r}$ in the three groups are given in Table IV-3.

TABLE IV-3

EXPECTED UNCERTAINTIES IN AVERAGE COUNTS

Group	N	$\bar{r}$	$\sigma_{\bar{r}}$	$2\sigma_{\bar{r}}$
I	102	16	0.4	0.8
II	41	25	0.25	0.5
III	18	18	1.0	2.0
		36	1.4	2.8
		72	2.0	4.0

Keeping these in mind, a feature that has

(i) two or more adjacent data points, and

(ii) stands at least two standard deviations above the continuum

will be considered a likely spectral line.

(6) The existence of a one to one correspondence between features in the flare scans of the two crystals shown in Figure IV-10, can also be considered to mean that the feature is a line, rather than a chance coincidence. An example of this is shown at 3.270 Å which is identified as the Lδ line of Cl XVII.

For the sake of convenience the more common lines and transitions are assigned key letters as listed in Appendix C. The lines which are identified using the criteria discussed above are listed with their key letters in Table IV-4. Results of other investigators as well as the latest theoretical wavelengths are also listed in this table for comparison.

The line identifications in the region 1.4 to 3.9 Å are based on Figures IV-8 and -10. Almost all the lines are identifiable only in the flare scan and therefore are produced at high temperatures. For $\lambda < 2.5$ Å, the error in wavelength is ± 0.01 Å; for $\lambda > 2.5$ Å it is ± 0.005 Å. However, the identified wavelengths are given to the nearest 0.005 Å in the first column of Table IV-4. The line identifications in the region 3.9 to 8.5 Å are based on Figures IV-9 and -11. The error in wavelength is ± 0.01 Å for all lines except where considerable blending exists. In this region the wavelengths are given to the nearest 0.01 Å.

Weak lines that barely satisfy the requirements of Table IV-3 are indicated by an apostrophe (') mark; lines which are present in both quiet scans and flare scans are indicated by a quotation (") mark in Table IV-4. When the theoretical wavelength or the atomic transition is uncertain (or unknown), the appropriate quantity is indicated by a question mark. The references for the theoretical wavelengths are listed at the end of Table IV-4.

DISCUSSION

Before discussing the confirmation of established identifications and new identifications made in this study a remark should be made about the intensities of lines in the summed scans. A study of individual flare scans (section IV.3) has shown that there are considerable variations in the line intensities during the course of the flares. Hence the summation of scans tends to average out the actual temperature dependence of the continuum or line intensities as well as their temporal dependence. Thus great significance should not be attached to the relative line intensities in the summed spectra. However, the magnitude of the intensities could be considered as typical of the solar activity involved. Thus the principal use of the summed scans is to identify new lines and improve the existing

TABLE IV-4

SOLAR FLARE EMISSION LINES

OSO-4 Å	NRL Å	GSFC Å	ASC Å	Theory Å	Ref.	Identification *
1.460'	1.47	1.456	-	1.4607	(12)	Fe XXV He - 4R
1.490'	1.52	1.509	-	1.4946	(12)	Fe XXV He - 3R
1.570'	1.58	1.567	-	1.5732	(12)	Fe XXV He - 2R
1.790	1.790	1.780	-	1.79	(5)	Fe XXVI H - L α
1.820	-	-	-	?		
1.850	1.852	1.850	-	1.8500	(7)	Fe XXV He - R
1.855	1.857	1.855	-	1.8551	(7)	Fe XXV He - I2
				1.8591		He - I1
1.865	1.867	1.865	-	1.8677	(7)	Fe XXV He - F
1.870 } unresolved				{	(7)	Fe XXIV, XXIII, XXII,
1.920					(5)	XXI, XX ...
1.930	1.94	1.931	-	1.937	(5)	Fe II K - α
1.965	-	-	-	?		
2.005	2.01	2.009	-	2.0056	(7)	Mn XXIV He - R
2.010	-	-	-	2.0114	(7)	Mn XXIV He - I2
				2.0154		He - I1
2.025'	-	-	-	2.0249	(7)	Mn XXIV He - F
2.180	2.175	2.179	-	2.1816	(7)	Cr XXIII He - R
2.185	-	-	-	2.1882	(7)	Cr XXIII He - I2
2.195	-	-	-	2.1922	(7)	He - I1
2.200	2.215	2.196	-	2.2028	(7)	Cr XXIII He - F
2.285	-	-	-	?		
2.325	-	-	-	?		
2.380	-	-	-	2.3815	(7)	Va XXII He - R
2.385	-	-	-	2.3891	(7)	Va XXII He - I2
2.390	-	-	-	2.3931		He - I1
2.405	-	-	-	2.4050	(7)	Va XXII He - F
2.420	2.42	2.441	-	?		
2.520	2.516	2.508	-	2.5136	(12)	Ca XIX He - 4R
2.550	2.55	2.548	-	2.549	(4)	Ca XX H - L β
2.570	2.573	2.572	-	2.5713	(12)	Ca XIX He - 3R
2.610	2.61	2.608	-	2.6099	(7)	Ti XXI He - R
2.615	-	-	-	2.6187	(7)	Ti XXI He - I2
2.620	-	2.621	-	2.6226	(7)	He - I1
2.635	2.64	2.634	-	2.6362	(7)	Ti XXI He - F
2.705	2.706	2.703	-	2.7053	(12)	Ca XIX He - 2R
2.715	-	-	-	?		
2.760	2.750	2.748	-	2.75 ?	(1)	Ca XVIII $(1s^2\ 2s\ ^2S-1s2s3p\ ^2P)$
2.800	-	--	-	?		
2.885	-	-	-	2.881	(4)	Ar XVIII H - L ϵ
2.900	-	-	-	?		
2.915	-	-	-	2.918	(4)	Ar XVIII H - L δ
2.985	-	2.990	-	2.987	(4)	Ar XVIII H - L γ

' indicates weak feature

* Appendix C

TABLE IV- 4 (Continued)

OSO-4 Å	NRL Å	GSFC Å	ASC Å	Theory Å	Ref.	Identification *	
3.025	3.026	3.022	-	3.020	(4)	Ca XX	H - Lα
3.150	3.16	-	-	3.151	(4)	Ar XVIII	H - Lβ
3.175	3.173	3.174	-	3.1765	(7)	Ca XIX	He - R
3.190	3.186	3.187	-	3.1887	(7)	Ca XIX	He - I2
				3.1924	(7)		He - I1
3.200	3.197 blend	blend	-	3.201	(7)	Ca XVIII	Li - q,r?
3.210	3.206	3.207	-	3.2103	(7)	Ca XIX + Ca XVIII	He - F Li - k,j..?
3.230	-	-	-	3.231	(4)	Cl XVII	H - Lϵ
3.245	-	3.238	-	3.254 ?	(5)	Ca XVI ($1s^2 2s^2 2p - 1s 2s^2 2p^2$)	
3.270	-	-	-	3.272	(4)	Cl XVII	H - Lδ
3.300	-	-	-	?			
3.330	-	-	-	?			
3.345	-	3.349	-	3.351	(4)	Cl XVII**	H - Lγ
3.365	3.371	-	-	3.367	(2)	Ar XVII	He - 2R
3.390	-	3.392	-	3.40 ?	(2)	Ar XVI ($1s^2 2s\ ^2S - 1s2s3p\ ^2P$)	
3.490	-	-	-	?			
3.505	-	-	-	?			
3.525	-	-	-	3.5312	(7)	K XVIII	He - R
3.530	3.534	3.542	-	3.534	(4)	Cl XVII	H -Lβ
3.540	-	-	-	3.5455	(7)	K XVIII	He - I2
3.545	3.550	-	-	3.5492	(7)		He - I1
3.560	-	-	-	3.563	(7)	K XVII	Li - q,k..?
3.570	3.573	3.572	-	3.5700	(7)	K XVIII	He - F
				3.5705	(7)	K XVII	Li - j
3.610	-	-	-	?			
3.630	-	-	-	?			
3.650	3.651	-	-	3.650	(4)	S XVI	H - Lϵ
3.685	-	-	-	?			
3.695	3.698	-	-	3.696	(4)	S XVI	H - Lδ
3.720	3.733	3.736	-	3.733	(4)	Ar XVIII	H - Lα
3.770	-	-	-	?			
3.800	-	-	-	?			
3.840	-	-	-	?			
3.91	-	-	-	?			
3.95	3.949	3.950	-	3.9483	(7)	Ar XVII	He - R
3.96	blend	3.969	-	3.967	(7)	Ar XVII	He - I2,I1
3.99	-	-	-	?			
4.00	4.004	3.995	-	3.9934	(7)	Ar XVII + Ar XVI	He - F Li - ?
4.06	-	4.058	-	?			

* Appendix C

** See, however, the discussion on page 98 for an alternative and more likely identification as K XIX.

TABLE IV-4 (continued)

OSO-4 Å	NRL Å	GSFC Å	ASC Å	Theory Å	Ref.	Identification *	
4.09	4.104	4.096	-	4.089	(6)	S XV	He - 3R
4.13"	-	-	-	?			
4.16	-	-	-	4.154	(4)	P XV	H - Lε
4.19	4.184	-	-	4.187	(4)	Cl XVII	H - Lα
4.20	-	-	-	4.207	(4)	P XV	H - Lδ
4.26	4.244	-	-	?			
4.30	4.299	4.306	-	4.30 4.308	(2) (4)	S XV P XV	He - 2R H - Lγ
4.38	4.394	4.383	-	4.38 ?	(2)	S XIV ($1s^2\ 2s\ ^2S - 1s2s3p\ ^2P$)	
4.45	-	4.454	-	4.4436	(7)	Cl XVI	He - R
4.46	-	-	-	4.466	(7)	Cl XVI	He - I2,I1
4.48	-	4.49	-	4.4965	(7)	Cl XVI	He - F
4.54	-	-	-	4.543	(4)	P XV	H - Lβ
4.68	4.674	4.685	-	?			
4.71	-	-	-	?			
4.73	4.729	4.733	4.734	4.729	(4)	S XVI	H - Lα
4.77	4.769	4.774	-	4.770	(4)	Si XIV	H - Lε
4.83	4.834	4.829	-	4.831	(4)	Si XIV	H - Lδ
4.88	4.884	4.879	-	?			
4.94	4.948	4.948	-	4.947	(4)	Si XIV	H - Lγ
4.96	-	-	-	?			
5.04	5.039	5.044	5.039	5.0379	(7)	S XV	He - R
5.06	5.067	5.068	5.065	5.064	(7)	S XV	He - I2,I1
5.10	5.099	5.105	5.100	5.1007	(7)	S XV +Li	He - F - ?
5.18	-	5.18	-	5.18 ?	(2)	S XII ($1s^2 2s^2\ 2p - 1s2s^2\ 2p^2$)	
5.22	5.221	5.223	5.219	5.217	(4)	Si XIV	H - Lβ
5.29	5.283	-	-	5.2853	(12)	Si XIII	He - 4R
5.35	-	-	-	?			
5.39	-	-	-	5.383	(4)	P XV	H - Lα
5.41	5.410	5.410	5.401	5.4044	(12)	Si XIII	He - 3R
5.54'	-	-	-	5.534	(4)	Al XIII	H - Lε
5.60'	-	-	-	5.605	(4)	Al XIII	H - Lδ
5.64	-	-	-	?			
5.68"	5.680	5.672	5.68	5.6805	(12)	Si XIII	He - 2R
5.74'	-	5.725	-	5.739	(4)	Al XIII	H - Lγ
5.75'	-	-	-	5.7593	(7)	P XIV	He - R
5.79'	-	-	-	5.792	(7)	P XIV	He - I2,I1
5.80	5.816?	-	5.810	5.797 ?	(3)	Si XII ($1s^2\ 2s\ ^2S - 1s2s3p\ ^2P$)	
5.81	-	-	-	5.817 ?	(3)	Si XII ($1s^2\ 2p\ ^2P - 1s2p3p\ ^2S, ^2D$)	
5.83	-	-	-	5.8349	(7)	P XIV	He - F
5.86	-	-	-	?			
5.95	-	-	-	?			

" appears in quiet and flare scans. ' weak feature. * Appendix C

TABLE IV-4 (Continued)

OSO-4 Å	NRL Å	GSFC Å	ASC Å	Theory Å	Ref.	Identification *	
6.00	-	-	-	?			
6.05	6.049	-	-	6.053	(4)	Al XIII	H - Lβ
6.18	6.182	6.182	6.184	6.182	(4)	Si XIV	H - Lα
6.20 bl	-	-	-	6.200 ?	(3)	Si XIII(1s2p ^{1}P - 2p^2 ^{1}P)	
6.21	-	-	-	6.224 ?	(3)	Si XIII(1s2s ^{1}S - 2s2p ^{1}P)	
6.24'	6.224	-	-	6.244 ?	(3)	Si XIII(1s2s ^{3}S- 2s2p ^{3}P)	
6.26	6.272	-	-	6.263 ?	(3)	Si XIII(1s2p ^{1}P- 2p^2 ^{1}D)	
6.32	-	-	-	6.314	(8)	Al XII	He - 3R
6.36'	-	-	-	?			
6.42	-	-	-	?			
6.49	-	-	-	6.497	(4)	Mg XII	H - Lϵ
6.58	6.58	6.578	-	6.580	(4)	Mg XII	H - Lδ
6.63"	-	-	-	6.635	(8)	Al XII	He - 2R
6.65"	6.650	6.640	6.649	6.6470	(7)	Si XIII	He - R
6.69"	6.690	6.681	6.684	6.686	(7)	Si XIII	He - I2,I1
6.74"bl	6.737	6.737	6.739	6.738	(4)	Mg XII	H - Lγ
				6.7394	(7)	Si XIII	He - F
6.78bl	6.787	6.78	6.788	6.785	(7)	Si XII	Li - ?
6.90"	-	6.884	-	6.896	(7)	Si XII	Li - ?
6.99	-	-	-	?			
7.06	-	-	-	?			
7.11"	7.106	7.104	7.111	7.106	(4)	Mg XII	H - Lβ
7.14	-	-	-	?			
7.17"	7.172	7.160	7.179	7.173	(4)	Al XIII	H - Lα
7.18 bl				7.18		Mg XI	He - 6R
7.23	-		-	7.23		Mg XI	He - 5R
7.31"	7.312	-	7.316	7.310	(8)	Mg XI	He - 4R
7.44	7.440	-	-	?			
7.48"	7.470	7.475	7.474	7.473	(6)	Mg XI	He - 3R
7.58	-	-	-	?			
7.68	7.682	-	-	?			
7.72 bl	-	-	-	?			
7.73"	-	-	-	7.735	(4)	Na XI	H - Lϵ
7.76"	7.755	7.761	7.759	7.7563	(7)	Al XII	He - R
7.81	-	7.795	7.805	7.805	(7)	Al XII	He - I2,I1
7.83"bl	-	-	7.827	7.833	(4)	Na XI	H - Lδ
7.85"	7.854	7.857	7.850	7.850	(6)	Mg XI	He - 2R
7.86" bl	7.864?	-	7.864	7.863 ?	(3)	Mg XI	He - 2I
7.87"	-	7.897	7.873	7.8712	(7)	Al XII	He - F
7.93"	7.935	-	-		(7)	Al XI	Li - ?

' weak feature. * Appendix C

" appears in quiet and flare scans. bl = blend

TABLE IV-4 (Continued)

OSO-4 Å	NRL Å	GSFC Å	ASC Å	Theory Å	Ref.	Identification *
7.99	7.990	-	-	7.979	(10)	Fe XXIV($1s^2 2s\ ^2S_{\frac{1}{2}}$ - $4p\ ^2P_{1\frac{1}{2}}$) Fe XXIV($^2S_{\frac{1}{2}}$ - $^2P_{\frac{1}{2}}$)
8.02"	-	-	-	8.021	(4)	Na XI H - L γ
8.04"	-	-	8.034	8.039 ?	(3)	Mg X ($1s^2 2s\ ^2S$- $1s2s3p\ ^2P$)
8.07"	8.073	-	8.068	8.073 ?	(3)	Mg X ($1s^2 2p\ ^2P$-$1s2p3p\ ^2D, ^2S$)
8.09	8.094	-	-	8.10 ?	(10)	Fe XXII($1s^2 2s^2 2p\ ^2P_{\frac{1}{2}}$- $5d\ ^2D_{1\frac{1}{2}}$)
8.12	-	-	-	?		
8.15	8.157	-	-	?		
8.16	8.170	-	-	?		
8.20	8.208	-	-	8.20 ?	(10)	Fe XXII($2p\ ^2P_{\frac{1}{2}}$ - 5s/5d)
8.23	8.233	-	-	8.225	(10)	Fe XXIV($1s^2 2p\ ^2P_{\frac{1}{2}}$- $4d\ ^2D_{1\frac{1}{2}}$)
8.24 bl	8.254	-	-	?		
8.26				?		
8.27	-	-	-	?		
8.28				?		
8.29	8.290	-	-	8.279	(10)	Fe XXIV($1s^2 2p\ ^2P_{\frac{1}{2}}$- $4s\ ^2S_{\frac{1}{2}}$)
8.30	8.307	-	-	8.306	(10)	Fe XXIII($2s^2\ ^1S$-$2s4p\ ^1P$)
8.31	8.317	-	-	8.311	(10)	Fe XXIV($2p\ ^2P_{1\frac{1}{2}}$- $4d\ ^2D_{2\frac{1}{2}}$)
				8.314	(10)	Fe XXIV($2p\ ^2P_{1\frac{1}{2}}$- $4d\ ^2D_{1\frac{1}{2}}$)
8.32	-	-	-	8.319	(10)	Fe XXIII($2s^2\ ^1S$-$2s4p\ ^3P$)
8.37	8.378	-	-	8.368	(10)	Fe XXIV($2p\ ^2P_{1\frac{1}{2}}$- $4s\ ^2S_{\frac{1}{2}}$)
8.38"	-	-	-	?		
8.42"	8.421	8.421	8.421	8.421	(4)	Mg XII H - L α
8.44 bl	-	-	-	8.449 ?	(3)	Mg XI($1s2p\ ^1P$ - $2p^2\ ^1S$)
8.46"	8.458	-	-	8.459	(4)	Na XI H - L β
8.48"	8.490	-	-	8.486 ? 8.488 ?	(11) (3)	Fe XXIII($2s2p\ ^3P$-$2s4d\ ^3D$) Mg XI($1s2s\ ^1S$-$2s2p\ ^1P$)

" appears in quiet and flare scans. * Appendix C

References:

(1) Naval Research Laboratory: Meekins et al.(1970); Doschek et al.(1971a,b)
(2) Goddard Space Flight Center: Neupert (1971)
(3) Aerospace Corporation: Walker and Rugge (1970,1971)
(4) Garcia and Mack (1965). (5) House (1969). (6) Blake (1968)
(7) Gabriel (1972b). (8) Flamberg (1942). (9) Cohen et al.(1968)
(10) Doschek et al.(1972). (11) Chapman (1969), wavelength extrapolated from (10). (12) Ermolaev et al.(1972)

identification if possible.

EXISTING IDENTIFICATIONS

As the Table IV-4 shows, most of the existing identifications are confirmed (see second, third and fourth columns). In the case of H-like and He-like ions, most of the lines, wherever resolved are in good agreement with accurate theoretical wavelengths calculated by Gabriel (1972b) and Garcia and Mack (1965). The iron feature between 1.87 and 1.92 Å is not resolved but is known to contain dielectronic satellites and inner-shell excitation lines (see Table II-4) of Fe XXIV and Kα lines of Fe XXIII, XXII, etc., upto Fe II (Doschek, 1972). Most of the lines due to He-like ions of Fe, Mn, Cr, Va and Ti are barely detectable. In all cases the two intercombination line components I2 and I1 (Appendix C) of He-like ions are not resolved and they will be referred to as I in the discussion. The peaks of R, I, and F lines of Ca XIX agree with Gabriel's wavelength. But they are also blended with unidentified dielectronic satellite contributions from Li-like Ca XVIII (see Table II-4 for a description of important lines). The feature at 3.270 Å (to be discussed later) is not considered to be a satellite line of Ca XIX since no known line falls in this region. Indication of weak but definitely present satellite lines can be seen in the flare scans at the red side of He-F lines of S (5.10 Å) and Si (6.75 Å); at the red side of Lα lines of Si (6.18 Å); at the blue side of He-2R line of Mg (7.48 Å). As these are not resolved proper identifications cannot be made.

The group of lines between 7.98 and 8.40 Å are interesting. All lines except those between 8.02 and 8.08 Å are not present in the quiet scan (Figure IV-9) but gradually rise in intensity in the sub-flare and the flare scans. Doschek et al., (1972) demonstrated that these lines are due to a blend of lines from the Li-like Fe XXIV and the Be-like Fe XXIII (see Table IV-4) rather than the K α transitions in aluminum ions as suggested by Meekins et al., (1970).

NEW IDENTIFICATIONS

The new identifications made in this study are the lines of H-like and He-like ions of chlorine, sodium and phosphorus. A few of these lines are shown in Figure IV-11, which is an enlargement of a part of Figure IV-9.

Chlorine: Lines at 4.19 Å and 3.27 Å are tentatively identified as the L α and L δ lines of Cl XVII. The observation of the 3.27 Å feature in the flare scans of both crystals in Figure IV-10 is an indication that it is a real line. This line is at least 0.04 Å away from the nearest known dielectronic satellite of He-like calcium (see Table II.4; Gabriel 1972b). Lines at wavelengths corresponding to the Lβ , Lγ and Lε transitions of Cl XVII are also present, but are blended with other lines (Figure IV-8). A perusal by Dr. Doschek of the more intense flare spectrum observed by the NRL OSO-6 experiment reveals the presence of these lines there. There are also lines present near 4.45 Å (Figure IV.11) near to the expected He R , I and F lines of Cl XVI. These lines also satisfy the statistical criteria given in Table IV.3.

However, it is now known (personal communication from Dr. Doschek) that the 1s ^2S - 2p ^2P transition of K XIX lies at 3.348Å , very close to the expected Lβ transition of Cl XVIII at 3.351 Å . In view of the greater solar and cosmic abundance of potassium than chlorine, it seems likely that the K XIX line is the major (and possibly the sole) contributor to the observed OSO-4 line at 3.345 Å . The masking of Lβ of Cl XVII therefore somewhat weakens, but does not destroy, the case for the positive identification of chlorine from other observed lines.

If, however, we accept the identification of the He-R line of Cl XVI, an estimate of the relative abundance of chlorine to calcium can be made by comparison with the corresponding lines of Ca XIX as measured in Figure IV-11. This ratio is approximately proportional to that of their abundances. The counts are corrected for the effective collecting area $A'(\gamma)$ and the efficiency $\varepsilon(\lambda)$ of the #1176 detector as described in section IV.2 and the ratio is determined. It is also assumed that the other instrumental parameters which are not taken into account here do not seriously affect the approximation. It is then estimated that the relative abundance of chlorine is about 40 per cent of calcium. This can be compared with almost equal abundance suggested by Aller's (1963) data for stellar composition.

Sodium: L-β, -γ and -δ lines of sodium have been identified. The Lyman α line falls at ~10 Å and therefore cannot be observed in OSO-4 spectra. The feature at 8.02 Å (Figure IV-9) is present in the quiet scan and increases in intensity in the flare scan. It is identified as the Lγ line of sodium. The other two lines are blended with the more intense magnesium lines but appear to be present in quiet and in flare scans. Other factors that support this identification are that sodium is ionized along with magnesium and that the He-like lines of sodium are observed with sufficient intensity in OSO-6 KAP crystal spectra (Doschek et al., 1973).

Phosphorus: The Lyman α and β lines of P XV have been identified. L-γ, L-δ, and L-ϵ lines are blended but appear to be present in the flare scan (Figures IV-11 and -10). The He-like lines of P XIV also appear to be present. On statistical grounds the identification of phosphorus is not absolutely certain. A likely reason is that the abundance of phosphorus in the solar corona is quite small and therefore only a very intense flare can bring out the lines.

IV.3 TEMPORAL VARIATION OF LINE INTENSITIES DURING FLARES

The slow scan speed (14 minutes/scan) of the OSO-4 spectrometers limits the number of scans to three or four during a flare. From these scans the temporal variations of the line intensities with the time history of a flare can be studied. This information will shed more light on the evolution of the flare.

For this purpose the scans of a class 1b flare that occurred on October

25, 1967, are studied. The corresponding Hα flash phase occurred at ~2328 UT (Table III-1). The available OGO-4 record is shown in Figure III-3. The raw counting rates in several prominent lines of Mg, Al, Si, S, Ca, and Fe have been measured and corrected for the counter dead time. These are plotted with an error of one standard deviation in Figure IV-12 as functions of the exact times (UT) of observation. The counting rates in the continua as well as the background (~8 c/s) are also indicated. The points are joined by guessed extrapolations. Surprisingly, all emission lines seem to attain their peak intensities nearly simultaneously with the Hα flare maximum. Other observations are the following:

(1) Hydrogen-like ion line intensities decay faster than those of helium-like ion lines.

(2) Heavier ion (e.g., Fe, Ca, S, Si) lines show a faster rate of decay than those of lighter ions (e.g., Al, Mg).

(3) At all wavelengths shown, the continuum intensity shows identical rise and decay with the flare.

(4) Rise times of line intensities appear to be short compared to decay times (assuming that the extrapolations are correct).

These observations can be interpreted as follows:

(1) The ionization equilibrium curves shown in Figure A-1 (Appendix A) indicate that the population of H-like ions are more sensitive to temperature than those of He-like ions. The curves also show that heavier ions exist in equilibrium at higher temperatures. These suggest that the flare plasma is cooling in the example considered above.

(2) The plasma temperature is capable of exciting lighter ion lines but not the heavier ions. This also explains the slower decay of light ions. Since OGO-4 data indicate an increasing emission measure and a decreasing

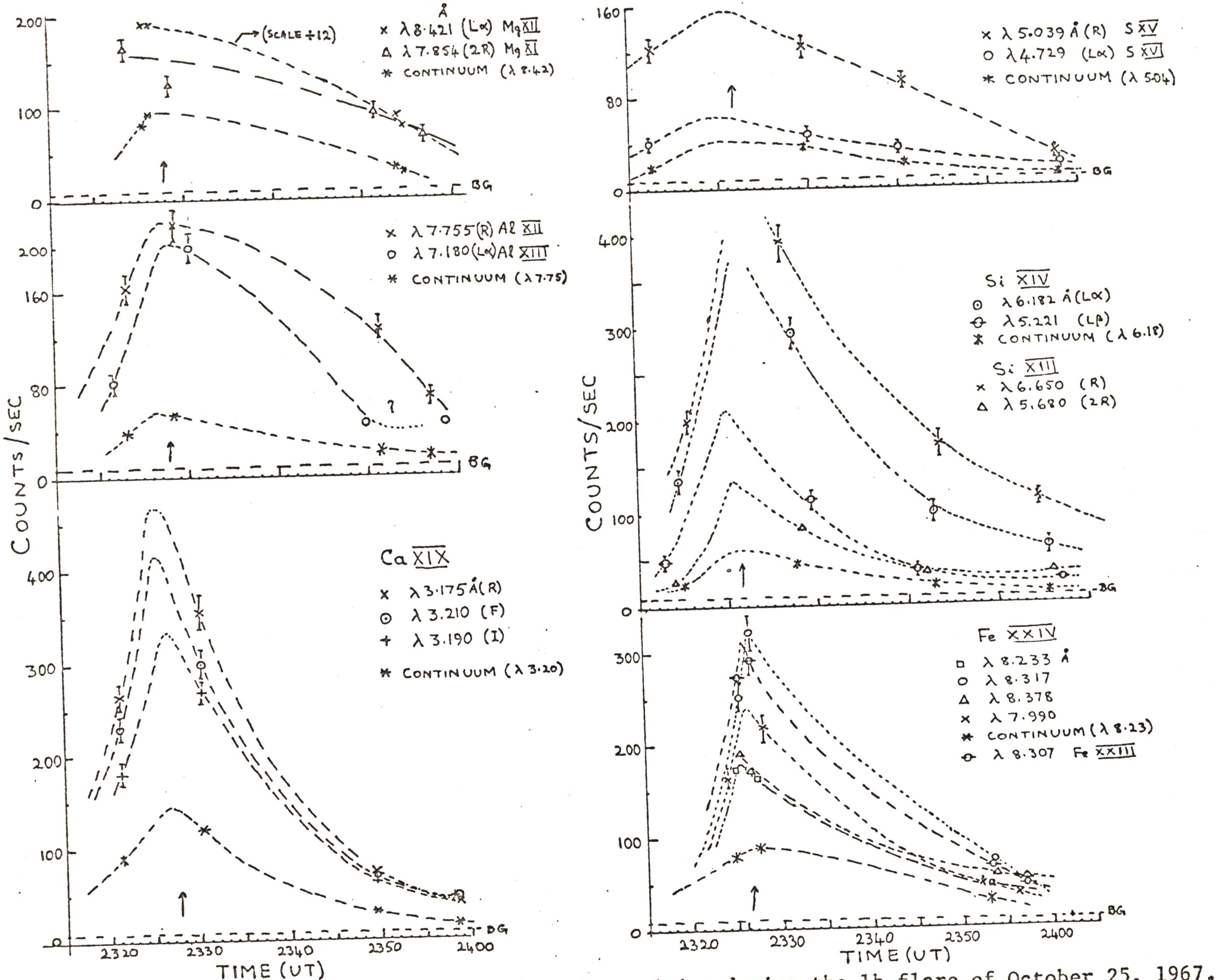

Figure IV-12. Temporal variation of line intensities during the 1b flare of October 25, 1967.

temperature, it is also likely that the lighter ion line emission is caused either by an increase in the plasma volume at constant electron density, or by an increase in electron density at constant volume, or both.

(3) The rise in line intensities appears to be as rapid as is the evolution of the flare before the flash phase.

The data points are too few to permit a more detailed analysis of the temporal variations. In fact, recently published data show that these are more complicated than the curves in Figure IV-12 suggest. The data from NRL OSO-6 spectrometers which have a faster scan time of 6 minutes, suggest that the peak flare emission in the lines of different elements is not simultaneous (Doschek, 1972). Similarly, studies of EUV line intensities (e.g., Mg X 625 Å line, and O VI 1032 Å line) with a time resolution of 30 seconds indicate that the EUV flare emissions consist of two main time components; one component is impulsive and coincides with the flash phase; the other component is a slow one that depends on the nature of the line and its emission region on the sun (Wood Jr. et al., 1972; Donnelly et al., 1973).

The temporal variation of the He-like Ca XIX line intensities which are illustrated in Figure IV-12, may be briefly considered. It is apparent that the forbidden (F) and the intercombination (I) line intensities are enhanced relative to that of the resonance (R) line as the flare cools.

The likeliest explanation is that the contributions from dielectronic satellites and inner shell excitation lines from the lithium-like Ca XVIII ion are increasing. The dielectronic recombination of Ca XIX as well as the inner shell excitation of Ca XVIII gives rise to a number of closely lying satellite lines as shown in Table II-4. Gabriel (1972b) has shown that the total intensity of these satellites is of the order of 30 to 40 per cent of the Ca XIX resonance line intensity, and that this fraction increases at lower temperatures depending on the amount of the Ca XVIII ion. A quantitative analysis of the satellite line contributions is not possible with OSO-4 spectra because of severe blending due to the low resolution.

The other possible explanation that the radiative recombination from the hydrogen-like Ca XX ion may be responsible can be ruled out because no significant emission of the Lymanα line of that ion is found in the scans, and therefore the number of radiative recombinations to ^3P and ^3S levels (from which the lines I and F are emitted) is negligible. Another extremely unlikely possibility is that the electron densities are decreasing from their original values in the range 10^{15} to 10^{16} cm^{-3} as required by the Gabriel-Jordan theory discussed in section II.3. As there is no indication of these high values in the flare plasma this mechanism can also be safely ruled out.

Finally, the enhancement of the He-F line relative to the He-R line is also noticed in the summed spectra by comparing the middle scan with the upper scan in Figures IV-8 and -9. This is not surprising since scans of the cooling phases of several flares were included in group II comprising the middle scan.

CHAPTER V

COMPARISON OF CONTINUUM SPECTRA AND BROAD BAND DATA

V.1 REDUCTION OF FLARE CONTINUUM SPECTRA

The experimental calibration parameters applicable to the spectral range 1.0 to 3.8 Å covered by the LiF spectrometers were determined in section IV.1. Typical flare scans will now be reduced using these parameters to obtain the continuum spectrum denoted by $I_{\lambda t}$ (photons cm^{-2} s^{-1} $Å^{-1}$) where t is the time of scanning the wavelength region around λ . As explained in connection with Figure IV-6, where an EDDT scan was partially reduced (with the exception of the integrated reflectivities of EDDT crystal), the LiF spectrometer scan are similarly smoothed and the continuum counting rates are read off at intervals of 0.1 Å between 0.8 Å and 3.8 Å. These are divided by the product of the effective collecting area of the LiF crystal (A') and its dispersion factor (2d sin θ) and the corrected values are plotted in the same manner as curve 1 in Figure IV-6. Since the region 0.8 - 1.5 Å also contains significant amounts of directly reflected x-rays, they are graphically estimated and subtracted out of the spectrum such that continuity is maintained with the plotted values at higher wavelengths. However, this procedure forces a cut off at 1.2 Å below which the actual spectrum cannot be estimated. This correction is based on the assumption that the actual continuum spectrum is slowly varying and has no discontinuities. Now the corrected values are divided by the appropriate value of $R(1,\lambda)$ $\in(\lambda)$ $T(\lambda)$ (these are explained in section IV.1) to obtain the continuum source spectrum $I_{\lambda t}$. In this way a few scans have been reduced and are discussed below.

Figure V-1 presents the continuum spectra from 1.2 to 3.8 Å derived from three scans relating to the 3b flare of November 16, 1967. These

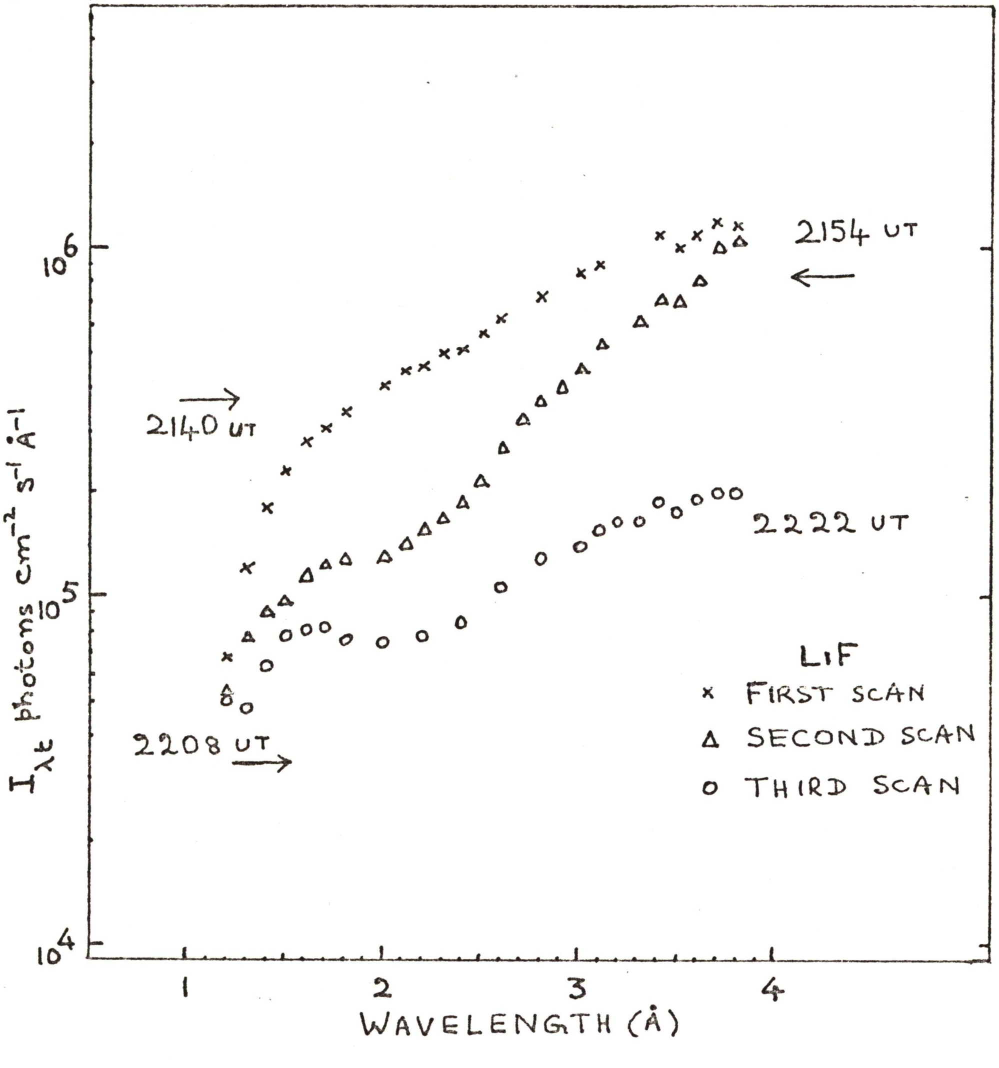

Figure V-1. Reduced continuum spectra of the 3b flare that occurred on November 16, 1967. The first LiF crystal scan begins at 2140 UT at 0.8 Å (direction is indicated by arrows), the second scan begins at 2154 UT at 3.87 Å, and the last complete scan ends at 2222 UT at 3.87 Å. The spectra indicate a cooling plasma.

scans cover successively the periods 2140-2154 UT, 2154-2208 UT, and 2208-2222 UT, and the first of these periods is shown in Figure III-10. The OGO-4 data of the flare (Fig. III-5) indicate that the start of the first scan has just missed the flare maximum. Thus all the scans cover only the cooling phase of this flare. Figure V-1 indicates that the flare is cooling by the gradual decrease in $I_{\lambda t}$ as the scans progressed in time and wavelength. It is also possible that the temperature is constant but the emission measure (N_e^2 V) is decreasing. The shape of any spectrum is affected by the fact that a time variation over an interval of 14 minutes is contained in the wavelength distributions of the incident solar flux. The apparent flattening of the spectrum in successive scans indicates that the rate of cooling is slowing down. An attempt at interpreting the changes in the spectra with the help of the OGO-4 data will be made in the next section.

Figure V-2 presents the continuum spectra reduced from two scans which cover the rise as well as the decay of a 1b flare of October 25, 1967. The two scans cover the periods 2312-2326 UT and 2326-2340 UT respectively, while the flare maximum was near 2327 UT. The corresponding OGO-4 record (Fig. III-3) are available only from 2330 UT onwards and they indicate a steady but rapid cooling of the plasma. The continuum spectrum $I_{\lambda t}$ between 2312 and 2340 UT shows nearly identical rise and fall with respect to the flare maximum. The 3.8 Å photon flux of the November 16 flare at 2154 UT (~14 min after maximum) in Figure V-1 is larger by a factor of 2 compared to the corresponding flux at the flare maximum (2326 UT) of the October 25 event in Figure V-2. This indicates that $I_{\lambda t}$ at the time of maximum for the 3b flare would have been much greater than the corresponding values for the 1b flare.

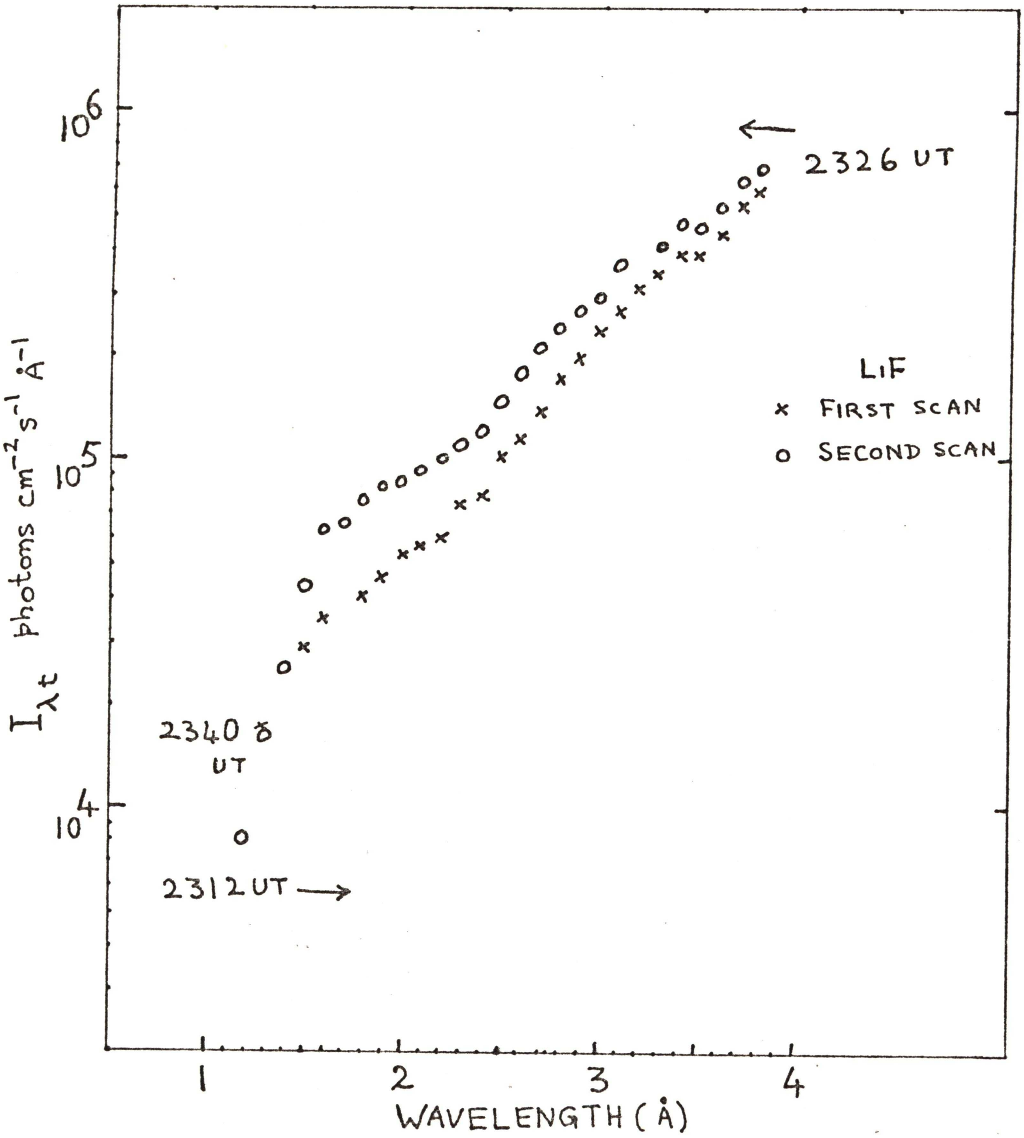

Figure V-2. Reduced continuum spectra of the 1b flare of October 25, 1967. The first LiF spectrometer scan begins at 2312 UT (in the direction shown by the arrows) and covers the rising phase of the flare. The second scan begins at the time of flare maximum and covers the cooling phase of the flare.

However, it is obvious that as each available scan has a different time relationship with flare time history no general conclusions can be made.

Errors: The errors in $I_{\lambda t}$ as reduced from the scans are the following:

(1) The statistical fluctuations proportional to the square root of counting rates.

(2) Error in $\epsilon(\lambda)$ of ~ 10%.

(3) Error in $R(1,\lambda)$ of ~20%.

Apart from these there are two other causes of errors whose magnitude cannot be determined. One is the uncertain amount of direct reflection of x-rays below 1.6 Å. The other is the unknown contribution from higher order reflectivities to the region 3 - 3.8 Å.

V.2 COMPARISON WITH SIMULTANEOUS OGO-4 DATA

The flare continuum spectra discussed above can be understood by comparing them with the predicted values from the simultaneous OGO-4 data. This comparison will shed light on the accuracy of the flare electron temperature T(K) and emission measure S(N_e^2 V cm^{-3}, where N_e is the electron density and V is the volume of the flare plasma) determined from the OGO-4 data. The method of determining these two plasma parameters and the underlying assumptions have been discussed in section III.4. The predicted continuum flux are found in the following manner:

(1) Determine T_t and S_t where the subscript t is added to emphasise the time dependence from OGO-4 data using the OGO-4 flux ratios given in Figure III-6.

(2) Determine the exact scan time t (UT) of the selected wavelength from OSO-4 scans.

(3) Using equation (II. 8) calculate the photon flux per unit emission

measure at temperature T_t; then multiply this by the corresponding emission measure S_t. This gives the predicted flux $I'_{\lambda t}$ to be compared with the reduced (observed) continuum flux $I_{\lambda t}$ plotted in Figure V-1 and -2.

It may be recalled here that T_t and S_t can be calculated either under a pure continuum (FF+FB) spectrum assumption or under a combined continuum and line (FF+FB+L) spectrum assumption (both of these are discussed in section III.4). Thus two sets of values of T_t and S_t, calculated from OGO-4 data in Figure III-5, are shown in Figure V-3 for the 3b flare of November 16, 1967. The purpose is to predict $I'_{\lambda t}$ under both spectral assumptions and find out which prediction gives a better agreement with OSO-4 data. In Figure V-3 it is observed that the temperature T_t(FF+FB+L) is $\sim 2 \times 10^6$K higher than T_t(FF+FB). However, the emission measure S_t(FF+FB) is found to be a factor $\sim$1.5 to 2 larger than S_t(FF+FB+L). The curves have a similar time dependence except between 2145 and 2200 UT (after which data is not available) when the continuum plus line based emission measure curve (S_t, lower curve) appears to be unchanging rather than increasing like the continuum based emission measure (S_t, upper curve). The reason for this becomes obvious by noting that the corresponding values of T_t(FF+FB+L) range between 14 and 10 x 10^6K. For this range of temperature, the expected total line flux as computed by Tucker and Koren (1971) has a maximum value with respect to the continuum flux in the 1 - 8 Å region; this can be seen in Figure III-7. This means that for an isothermal plasma at these temperatures, the line radiation provides an equally efficient energy loss mechanism; hence an increase in the emission measure (either in the electron density N_e or in the volume V or both) is thus prevented.

Now as described earlier in this section, using the values of T_t and

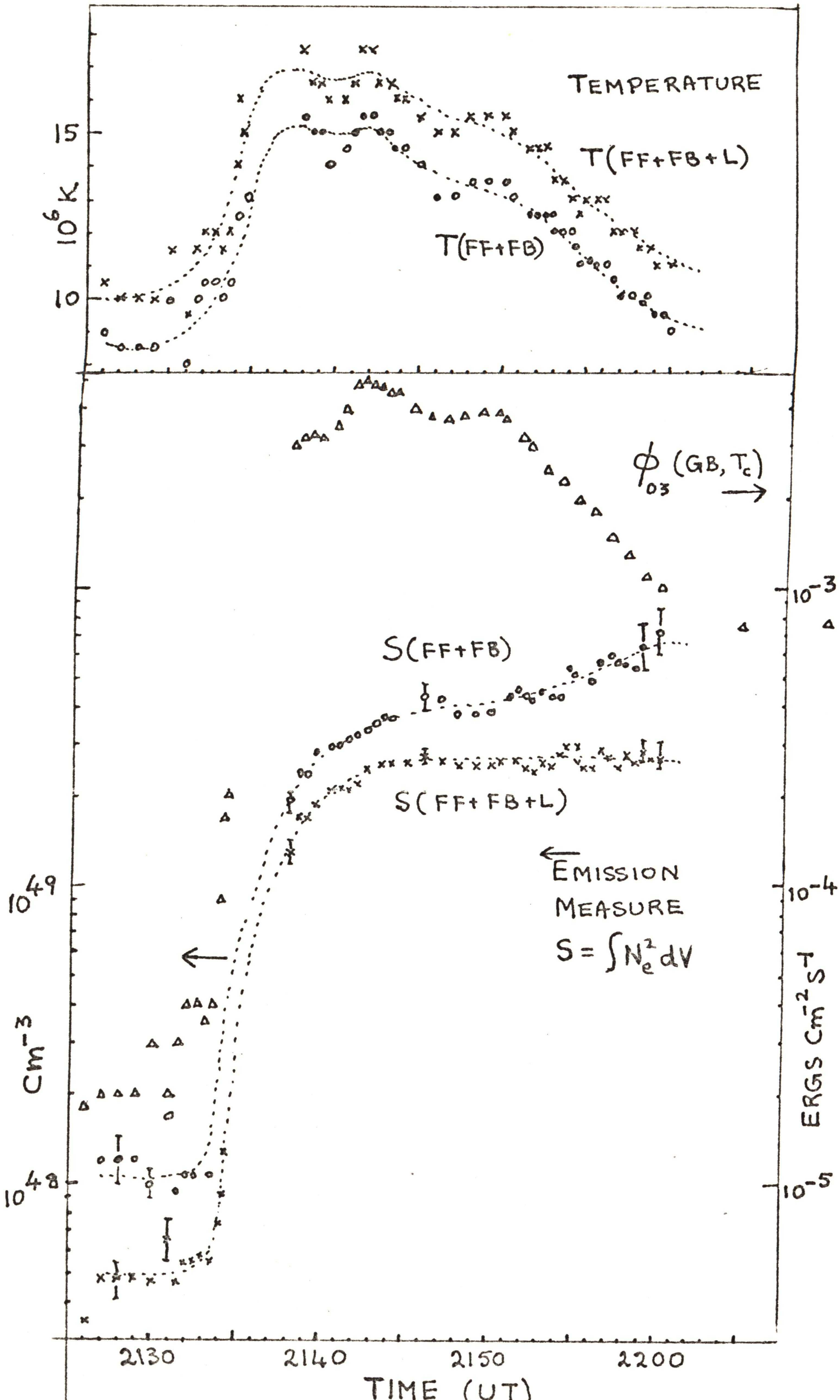

Figure V-3. Temperatures and emission measures calculated for the 3b flare of November 16, 1967. OGO-4 0-3 Å flux is also shown. Values are based on FF+FB flux (x) and FF+FB+Line flux (o).

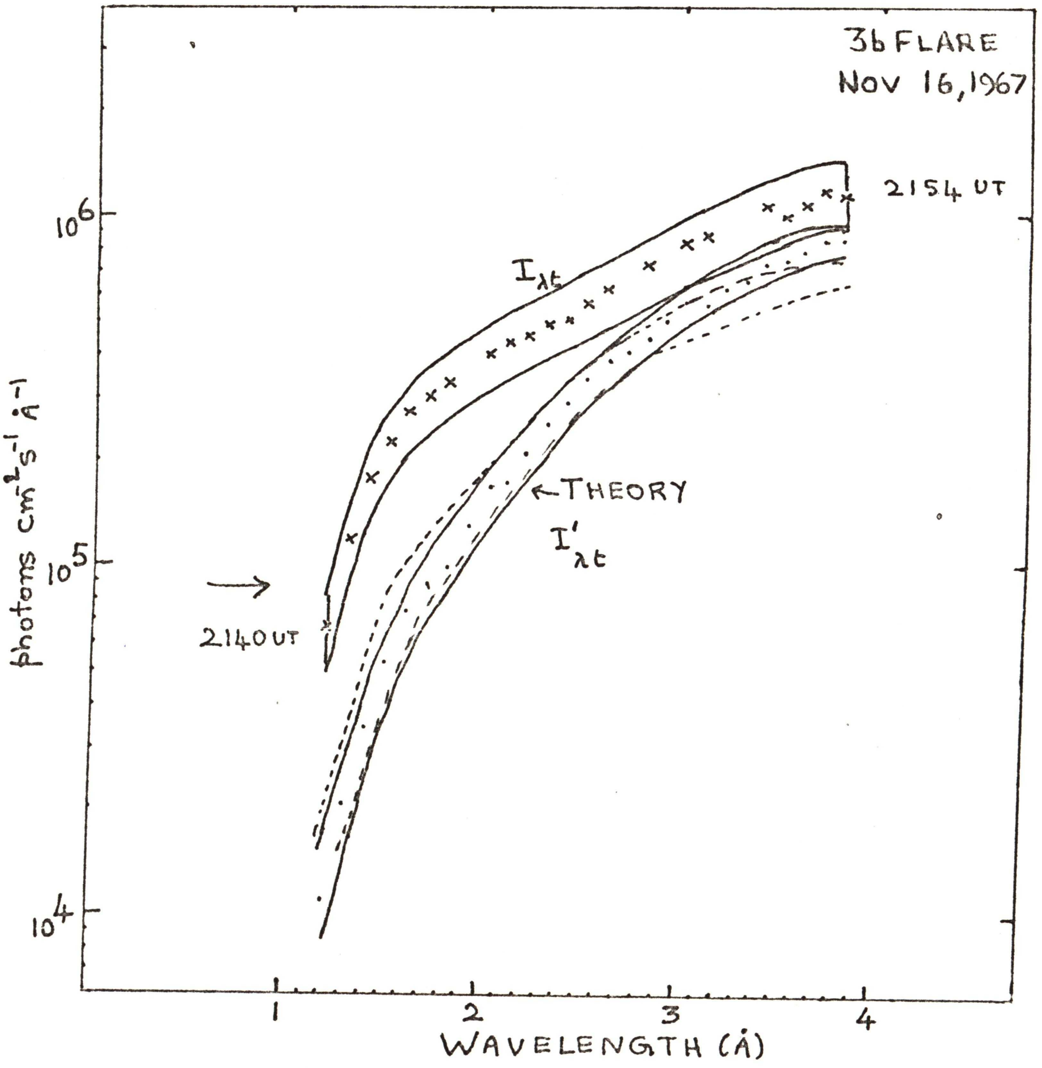

Figure V-4. Comparison of the predicted spectra with the reduced continuum spectrum for the scan times shown. The solid and dashed lines indicate the error bounds. The predicted values (Theory) are based on FF+FB emission and the two sets of temperatures and emission measures found from simultaneous OGO-4 data as shown in Fig. V-3. Dashed lines are the predicted values based on FF+FB+Line assumption (see text).

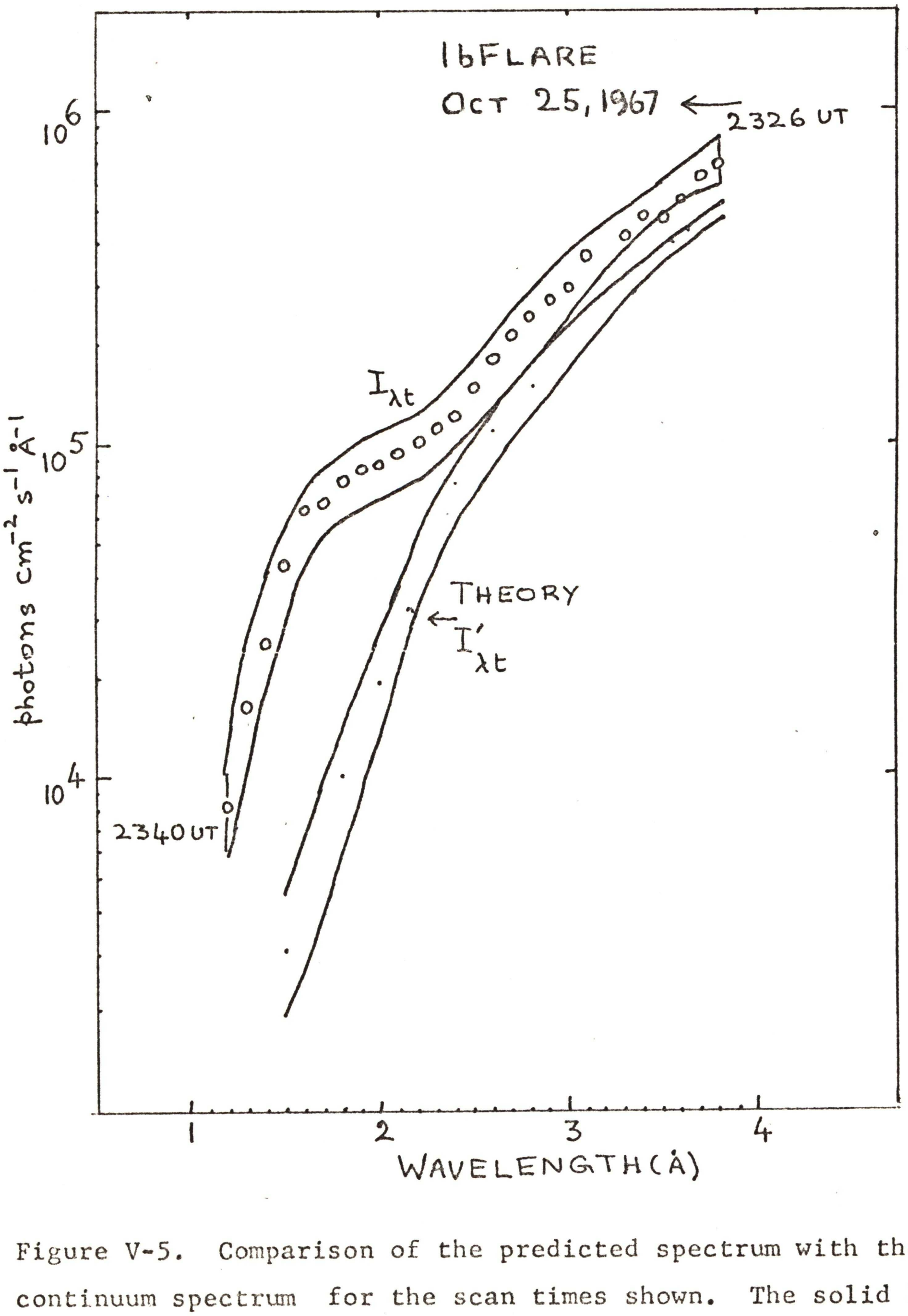

Figure V-5. Comparison of the predicted spectrum with the reduced continuum spectrum for the scan times shown. The solid lines indicate the error bounds. The predicted values (Theory) are based on FF+FB emission at the temperatures and emission measures found from simultaneous OGO-4 data (Fig. III-3).

S_t calculated under both spectral assumptions (FF+FB+L and FF+FB), the corresponding predicted continuum fluxes $I'_{\lambda t}$(FF+FB) and $I'_{\lambda t}$(FF+FB+L) respectively are calculated and plotted in Figure V-4, along with the reduced continuum flux $I_{\lambda t}$ between 2140 and 2154 UT. The error limits of the predicted values assume an error of $\pm$ 0.5 x 10^6K in T_t only. However the error limits in $I_{\lambda t}$ are assumed to be $\pm$ 25 per cent in view of the various sources of error described in section V.1. But these may have been underestimated both for $\lambda < 1.5$ Å and $\lambda > 3$ Å. Hence the predicted and observed fluxes are enclosed within their upper and lower error bounds.

It can be seen that there is good agreement between observed and predicted continuum fluxes above 2.5 Å. The extent of disagreement increases at lower wavelengths to a factor of ~ 2 near 1.2 Å. The interesting thing is that the predicted fluxes based on the continuum plus line assumption do not significantly differ from those based on continuum (FF + FB) flux assumption. This is brought about by the lower values of emission measures at higher temperatures as shown in Figure V-3. Thus, on the whole, the spectral shape of $I_{\lambda t}$ is well approximated by that of $I'_{\lambda t}$ (FF+FB). In the example considered below only the continuum based temperatures and emission measures will therefore be considered. The fit of the predicted values with the second scan (2326 — 2340 UT, Figure V-2) for which the OGO-4 data is available (Figure III-3) is shown in Figure V-5. The disagreement between $I_{\lambda t}$ and $I'_{\lambda t}$(FF+FB) is again obvious at lower wavelengths even though this flare is small compared to the earlier example considered here.

However, in both Figures V-4 and -5, the magnitude of the disagreement between the predicted and the reduced continuum fluxes at low wavelengths should not be taken seriously. This is because it is not possible to determine exactly the contribution of the directly reflected radiation to the continuum spectrum at these wavelengths. But the satisfactory agreement at higher wavelengths permits the following conclusions:

(1) The flare plasma processes responsible for the continuum emission above 2 Å are thermal in nature.

(2) The continuum flux in these wavelengths can be adequately described by a free-free and free-bound emission at an appropriate temperature from the plasma.

(3) The simultaneous flare data from the OSO-4 LiF spectrometer and from the OGO-4 broad band detectors are in agreement with each other within the limits of the expected instrumental errors.

V.3 TOTAL FLARE EMISSION IN 0 - 3 Å AND 1 - 8 Å BANDS

As described in section III.2 , OGO-4 data plots give the flare emission rates (ergs cm^{-2} s^{-1}) in both the 0.5 - 3 Å and the 1 - 8 Å bands as a function of the time. It is possible to determine the total energy emitted in these bands during the active lifetime of the flare. Since each flare has a different time history (see Figures III-1 to III-5) a study of the total energy emitted through the soft x-radiation channel will make it possible to define the energy scale involved in different flares.

A perusal of the time profiles of several flares as given in OGO-4 data plots indicates that many have a triangular shape (see Figure III-2). In these cases the area enclosed by the 'triangle' above the preflare flux base line gives the total energy received at the earth per unit area of the detector; this is equal to one half the product of the peak flux in the band above the preflare level and the duration of the flare. The same triangular approximation was used to estimate the areas of the time profiles which were not exactly triangular; the accuracy of the areas so determined was considered adequate for the purposes of this investigation.

The areas of the flare time profiles give the total energies received at the earth in units of ergs cm^{-2}; since the data points are based on the gray body approximation (equation III.6) the total energies are also based on the same approximation. In order to convert them to the values based on the thermal continuum (free-free and free-bound) spectrum the following have to be done:

(1) Determine the electron temperature at each data point using Horan's method described in section III.3.

(2) Pick the appropriate conversion factor from the last two columns of Table III-2 and multiply the corresponding data point in order to base it on the thermal continuum assumption.

(3) Integrate (numerically or use a planimeter) to determine the area which gives the required quantity.

While this method gives accurate values it is quite tedious when a large number of flares are considered. Hence an alternate method which acheives the conversion by a simple multiplication has been developed for use in this work as described below.

The method is based on the fact most of the flares pass through temperatures ranging from 7 to 20 x 10^6 K during their evolution and decay (see e.g., Figures III-8 and V-3). Table III-2 shows that the corresponding gray body to continuum conversion factors do not vary considerably. Thus it would be justifiable to use an average value of these conversion factors. The mean of the last 14 conversion factors listed in Table III-2 for each soft x-ray band are:

0.5 - 3 Å band: 0.94, 1 - 8 Å band: 0.35

Now the gray body based total energies determined earlier can be multiplied by the appropriate mean conversion factor to base them on the thermal continuum spectral assumption. The converted quantities are then multiplied by the area factor $4\pi\cdot(\text{sun to earth distance})^2\ \text{cm}^2$, to give the total energies L_{03} and L_{18} ergs where the subscripts denote the soft x-ray bands; these are the total energies produced in the flare and therefore are characteristic of the flare. The method will now be illustrated for the 1n flare shown in Figure III-2:

0 - 3 Å band:

$$\begin{aligned} \text{area} &= 0.5 \times 8.0 \times 10^{-3} (\text{erg cm}^{-2}\text{s}^{-1}) \times 33 \times 60\ (\text{sec}) \\ &= 7.92\ \text{ergs cm}^{-2}\ (\text{gray body based}) \\ &= 7.92 \times 0.94\ \text{ergs cm}^{-2}\ (\text{FF} + \text{FB based}) \\ L_{03} &= 7.92 \times 0.94\ \text{ergs cm}^{-2} \times 2.79 \times 10^{27}\ \text{cm}^2 \\ &= 2.0 \times 10^{28}\ \text{ergs.} \end{aligned}$$

1 - 8 Å band:

$$\begin{aligned} \text{area} &= 0.5 \times 1.75 \times 10^{-1} \times 33 \times 60\ \ \text{ergs cm}^{-2} \\ &= 173.25 \times 0.35\ \text{ergs cm}^{-2}\ \ (\text{FF} + \text{FB based}) \\ L_{18} &= 173.25 \times 0.35 \times 2.79 \times 10^{27}\ \text{ergs} \\ &= 1.7 \times 10^{29}\ \text{ergs.} \end{aligned}$$

In addition to L_{03} and L_{18} it is useful to calculate the ratio RL which determines the spectral hardness of emission and is given by

$$RL = L_{18} / L_{03}$$

which, for the example considered above, has the value 8.50. In this way 21 flares which occurred during the interval July 1967 - March 1968 have been analysed and the results are presented in Table V-1. These flares were selected subject to the requirement that nearly complete

TABLE V-1

TOTAL FLARE EMISSION IN 0 - 3 Å AND 1 - 8 Å RADIATION

DY MO YR	CLASS	MAXIMUM * FLUX AT UT	L_{03} ergs	L_{18} ergs	RL
16 01 68	Sn #	1702	1.6×10^{27}	1.8×10^{28}	11.4
28 02 68	Sn	1937	5.5×10^{26}	8.2×10^{27}	14.9
30 07 67	1b	0627	3.6×10^{27}	3.5×10^{28}	10.0
02 08 67	1n	0047	2.0×10^{28}	1.7×10^{29}	8.5
30 08 67	1b	0504	1.1×10^{28}	8.8×10^{28}	8.0
20 10 67	1b	0010	5.8×10^{27}	5.3×10^{28}	9.0
22 10 67	1b	2217	4.3×10^{27}	5.0×10^{28}	11.5
24 10 67	1b	1613	1.9×10^{27}	2.5×10^{28}	12.7
25 10 67	1b	2327	1.4×10^{28}	2.0×10^{29}	14.3
26 10 67	1b	0614	8.1×10^{27}	9.1×10^{28}	11.2
13 11 67	1f	1815	1.7×10^{27}	2.0×10^{28}	11.7
01 12 67	1b	1252	2.8×10^{28}	2.3×10^{29}	8.4
11 12 67	1b	2214	1.6×10^{28}	1.4×10^{29}	8.8
11 01 68	1b	1702	1.3×10^{28}	9.8×10^{28}	7.5
21 03 68	1b	1425	1.3×10^{27}	2.3×10^{28}	18.0
24 03 68	1b	1645	1.4×10^{28}	1.4×10^{29}	10.0
25 03 68	1b	1449 1505	9.6×10^{27}	1.0×10^{29}	10.2
01 08 67	2b	1736	1.6×10^{28}	1.5×10^{29}	9.4
29 10 67	2b #	2358	1.9×10^{29}	2.5×10^{30}	13.1
16 11 67	2n	1014	3.2×10^{28}	3.0×10^{29}	9.4
16 11 67	3b	2142	4.1×10^{28}	3.5×10^{29}	8.5

Limb flare
* Time of peak 0-3 Å detector flux as indicated by OGO-4 data.

OGO-4 data were available and that their time histories were not long ($<$ 3 hours) and complex. The selected flares had a duration between 28 and 155 minutes. Their date of occurrence, Hα importance rating (S for sub, 1, 2, or 3 depending on the estimated area of maximum H emission; the letters f, n, or b are also attached to indicate if the flare was visually faint, normal, or bright respectively), and the time of peak emission in the 0-3 Å OGO-4 broad band flux are also listed in Table V-1.

It is seen in Table V-1 that there is a considerable variation in the energies lost by flares. The distinction between the total emissions and the H flare importance does not appear to be quite clear. The wide fluctuations in the spectral hardness RL (ratio of total emissions in the two bands) shows that Hα flare area is probably not a good parameter to use when describing flare x-ray emission. A better sense of comparison emerges when the mean values (denoted by a prime) of the total energies and their ratios are calculated for each flare area category. These are listed in Table V-2.

TABLE V -2

MEAN VALUES OF L_{03}, L_{18}, and RL

FLARE IMPORTANCE	NUMBER OF EVENTS	L'_{03} (ergs)	L'_{18} (ergs)	RL'
S	2	1.1×10^{27}	1.3×10^{28}	11.8
1	15	1.0×10^{28}	1.0×10^{29}	10.0
2	3	8.0×10^{28}	1.0×10^{30}	12.0

It can be seen that the average total emission in the two soft x-ray bands increases by an order of magnitude as the flare importance (area) increases. Thus the energy output is proportional to the Hα area of the flare. The fact that the mean value of the spectral hardness is nearly a constant (Table V-2) for the flares considered clearly shows that there is no relationship between $H\alpha$ flare area and the spectral hardness; but a relationship probably does exist between $H\alpha$ flare area and the total emission as a whole.

Comparison with other studies: The total energy lost in the soft x-ray bands as given in Tables V-1 and -2 can be compared with the total emission in different wavelength segments. The typical values estimated by other investigators are collected in Table V-3.

TABLE V-3

TOTAL EMISSION IN OTHER WAVELENGTHS DURING FLARES

WAVELENGTH INTERVAL	FLARE IMPORTANCE	TOTAL ENERGY LOST (ergs)	REFERENCE
0 - 1.2 Å	1b	3×10^{26}	Kane, 1969
3.5 - 12 Å	"Typical"	$10^{28} - 10^{29}$	Krieger & Vaiana, 1969
3.5 - 12 Å	"Great"	10^{30}	"
8 - 12 Å	1f	2×10^{28}	Thomas, 1970
"	1n	5×10^{28}	"
"	1b, 2f	1×10^{29}	"
"	2n	2×10^{29}	"
"	2b	5×10^{29}	"
"	3n	1×10^{30}	"
8 - 12 Å	3b	1×10^{31}	"
10 - 1030 Å	1b	6×10^{29}	"
$H\alpha$	1b	1×10^{29}	"
$H\alpha$	2	3×10^{30}	Billings & Roberts, 1953
$H\alpha$	3	10^{31}	Bruzek, 1967
Visual	2	6×10^{29}	Kiepenheuer, 1967
Visual	3	10^{32}	Bruzek, 1967
Fast electrons (hard x-rays)	"Large"	5×10^{31}	de Jager, 1968 (see Ref.
Relativistic particles	"	3×10^{31}	" #119)
Subrelativistic "	"	2×10^{31}	"
Total energy	"Large"	3×10^{32}	"

The comparison for flares of identical Hα flare areas suggests that:

(1) The total 0.5 - 3 Å emission is larger than the total emission in hard x-rays (0 - 1.2 Å).

(2) The total 1 - 8 Å emission has the same order of magnitude as that of the 8 - 12 Å emission.

(3) The total emission in 1 - 8 Å, 8 - 12 Å, 10 - 1030 Å, visual, and in Hα wavelength segments respectively has the same order of magnitude. However, the total emission in 0.5 - 3 Å segment appears to be an order of magnitude smaller.

In conclusion the total flare energy emitted in the soft x-ray (0.5 to 8.0 Å) channel constitutes a non-negligible fraction of the total electromagnetic energy produced during a flare. This conclusion is complimented by that of Thomas (1970) from a similar study of the total 8-12 Å emission in flares.

CHAPTER VI

DISCUSSION AND CONCLUSION

VI.1 SUMMARY

The following results were obtained in Chapters IV and V :

(1) More accurate instrumental calibration parameters for the range 1.0 - 3.8 Å were obtained by experimentally determining the quantum efficiency of the Geiger counter and by using the values of the first order LiF crystal reflectivities measured by Meekins.

(2) Reduced continuum spectra (photons cm^{-2} sec^{-1} $Å^{-1}$) were obtained for several OSO-4 flare scans. They were compared with the calculated continuum spectra based on the time dependent values of temperature and emission measure as determined from OGO-4 data and on the theoretical expression given by equation (II.8) for free-free and free-bound emission. It was found that the predicted continuum spectrum fairly approximated the shape of the observed spectrum and that their magnitudes agreed with each other between 2.5 and 3.8 Å. Thus it was concluded that the continuum based temperature and emission measure as determined by the application of Horan's method (section III.3) to OGO-4 data give a fairly accurate picture of the gross properties of the flare plasma.

(3) A large number of OSO-4 flare scans and quiet scans were separately summed to improve the statistics of weak lines. Most of the statistically significant lines agreed with their theoretical wavelengths (see Table IV-4) to within ± 0.01 Å; inaccuracies in the earlier wavelengths and identifications (Doschek, 1972) were reduced. Several weak lines were identified as probably due to Na XI, P XV, and Cl XVII; but the Li-like satellites to

He-like R, I and F lines were blended and could not be identified.

(4) The temporal behaviour of line intensities closely matched the evolution of the flare. However, the data points were spaced too far in time to reveal any significant differences in the evolution of different ion lines.

(5) The total flare emission in 0.5 - 3 Å and 1 - 8 Å soft x-ray bands were determined from OGO-4 data for 21 flares (ranging from class S to class 3). A simple method was devised to convert the gray body based areas of time profiles to ones based on thermal continuum flux. It was found that the total emission in the 0.5 - 8 Å band was comparable to the total emission in other wavelength bands (see Table V-3).

VI.2 DISCUSSION

The results discussed above (except the first) have been affected by the following instrumental limitations:

(1) Both OGO-4 and OSO-4 instruments view the entire sun. Thus they have no spatial resolution.

(2) OSO-4 spectrometers have, in addition, a very slow scan speed (14 minutes per scan).

In view of the slow scan speed a typical flare scan reflects temperature changes of the order of ~ 5 to 10×10^6K. Thus it is difficult to decide whether the reduced continuum spectrum between 1 and 3.8 Å is due to the flare plasma at a single temperature or due to a plasma with multithermal composition. This is possible only if the entire spectral range is scanned instantaneously or within a few seconds. Recent experiments with fast scanning speeds of ~ 1 minute (Meekins, 1973) indicate that the continuum spectrum (1 to 25 Å) even from active regions can be described only by a multithermal plasma. It has been described as a differential emission measure which exponentially decreases as the temperature increases. It is thus clear that the slow scan speed of the OSO-4 spectrometer is a serious limitation. This study shows that a fairly accurate description of the average plasma parameters at any time during the OSO-4 scan can be obtained by determining the temperature and emission measure from the simultaneous OGO-4 data. The electron number density, however, can be determined from the emission measure (N_e^2 V) only if the volume of the particular flare plasma is known. The x-ray focussing spectrometer experiments by Vaiana et al., (1968) show that the soft x-ray emitting region consists of small filaments of threads which have a typical volume of the order of 10^{28} cm^3. Considering that the maximum emission measure of the 3b flare of November 16, 1967 (see Figure V-3) was about 5 x 10^{49} cm^{-3}, this would mean an N_e of the order of 10^{10} to 10^{11} cm^{-3}.

It can be seen in the line list (Table IV-4) that the theoretical wavelengths are in many cases known to an accuracy of 0.001 A or better, whereas the measured wavelengths in the summed scans are accurate to ± 0.01 A; blended lines are more uncertain. Hence this line list cannot be considered as final.

The following picture of a flare is suggested from the analysis of the soft x-ray emission data carried out in this thesis:

(1) During the rising phase of the flare, ions are further ionized and the line intensities reach their peaks nearly simultaneously with that of the Hα emission of the flare.

(2) During the decaying phase of the flare, the decrease in the line intensities appears to follow the decrease in the average electron temperature as indicated by the OGO-4 data, in the expected manner.

However, it is not possible to specify whether changes in N_e, or T, or in the volume of the plasma alone or together are responsible for the temporal behaviour of the line intensities.

(3) It appears that a residual injection of energy continues throughout the duration of the flares studied in this thesis, and this results in a continuing emission of soft x-rays.

(4) The fact that the spectral hardness (defined earlier as the ratio of the total emission in the 0 - 3 Å and the 1 - 8 Å bands respectively) varies from flare to flare, but is in general a constant for the flares studied here, suggests that this is an important feature to be explained by any proposed detailed model of a flare.

VI.3 PROPOSALS FOR FURTHER RESEARCH

(1) It is desirable to obtain a positive confirmation of the identification of the lines of chlorine and phosphorus in the spectra of intense flares as these are not available from OSO-4 scans.

(2) A list of average line intensities (absolute values) should be compiled from the summed scans when the measured reflectivities of the OSO-4 EDDT crystal are available.

(3) Future crystal spectrometer experiments should have high temporal, spatial, and wavelength resolution. In particular, it is necessary to resolve the large number of blended lines as noted in Table IV-4, and identify as well as determine their wavelengths to an accuracy of at least ± 0.001 Å. A theoretical calculation of the wavelengths of the expected satellites to H-like ion lines and also to the higher members of He-like ion lines (e.g., satellites to $1s^2 - 1s\,n\ell$ where n = 3, 4,...) similar to that of Gabriel (1972b) is also required.

In this connection the study carried out in this thesis supports the recent suggestion of Meekins (1973) that measurement of solar flare spectra should be made by an array of spectrometers, simultaneously sampling the important lines such as Fe XXVI, Fe XXV, Fe XXIV, Ca XX, Ca XIX, and similar ions of the lighter elements. It is also interesting to note that Grineva et al., (1973) have obtained high resolution spectra of iron lines near 1.87 Å. Similarly Bonnelle et al., (1973) have studied the emission of the He-R line of Mg XI and the Lyman α line of Mg XII. A number of high resolution instruments aboard the manned SKYLAB spacecraft are now producing data of a high quality (Maran and Thomas, 1973).

(4) The temporal behaviour of the soft x-ray emission lines should be investigated by instruments having a time resolution of the order of a few seconds in order to determine the nature of the excitation mechanisms.

REFERENCES

1. Aller, L.H. 1963. The Atmospheres of the Sun and Stars. The Ronald Press Co., New York, p 417.

2. Bame, S.J., Asbridge, J.R., Hundhausen, A.J., and Montgomery, M.P. 1970. Solar wind ions: Fe IX to Fe XIII, Si IX, Si X, and O VII. J. Geophys. Res. 75, 6360.

3. Bevington, P.R. 1969. Data Reduction and Error Analysis for the Physical Sciences. McGraw-Hill Book Co., Inc., New York, p 78.

4. Billings, D.E. 1966. A Guide to the Solar Corona. Academic Press, New York, p 131.

5. Billings, D.E., and Roberts, W.O. 1953. Isophotal photometry of a solar flare. Astrophys. J. 118, 429.

6. Blaha, M. 1971. Theoretical intensities of Fe XIV in the solar extreme ultra violet spectrum. Solar Physics, 17, 99.

7. Blake, R.L. 1968. Private Communication quoted by Doschek (1972).

8. Blumenthal, G.R., Drake, G.W.F., and Tucker, W.H. 1972. Ratio of line intensities in He-like ions as a density indicator. Astrophys. J. 172, 205.

9. Bonnelle, C., Chambe, G., Guionnet, M., Henoux, J.C., Michard, R., Senemand, C., and Senemand, G. 1973. X-Ray spectroheliograms in lines of Mg XI and Mg XII. Solar Physics, 29, 341.

10. Brussard, P.J., and van de Hulst, H.C. 1962. Approximation formulas for non-relativistic Bremsstrahlung and average Gaunt factors for a Maxwellian electron gas. Rev. Mod. Phys. 34, 507.

11. Bruzek, A. 1967. Physics of solar flares: The energy and mass problem. In Solar Physics, edited by J.N. Xanthakis, Interscience, New York, p 399.

12. Burgess, A. 1964. Dielectronic recombination and the temperature of the solar corona. Astrophys. J. 139, 776.

13. Burgess, A. 1965. A general formula for the estimation of dielectronic recombination coefficients in low density plasmas. Astrophys. J. 141, 1588.

14. Burgess, A., and Seaton, M.J. 1964. The ionization equilibrium for iron in the solar corona. Mon. Not. R. astr. Soc. 127, 355.

15. Burnight, T.R. 1949. Soft x-radiation in the upper atmosphere. Phys. Rev. 76, 165.

16. Chapman, R.D. 1969. Oscillator strengths and wavelengths of some x-ray and EUV spectrum lines of highly ionized iron. Astrophys. J. 156, 87.

17. Chubb, T.A. 1972. Evidence that solar x-ray emission is of purely thermal origin (also observation of far UV flash during 28 Aug 1966 proton flare). In Solar-Terrestrial Physics/1970, edited by E.R. Dyer, Reidel Publishing Co., Holland, Part I, p 99.

18. Cohen, L., Feldman, U., Swartz, M., and Underwood, H.J. 1968. Study of the x-rays produced by a vacuum spark. J. Opt. Soc. Amer. 58, 843.

19. Cox, D.P., and Tucker, W.H. 1969. Ionization equilibrium and radiative cooling of a low density plasma. Astrophys. J. 157, 1157.

20. Culhane, J.L. 1969a. Thermal continuum radiation from coronal plasmas at soft x-ray wavelengths. Mon. Not. R. astr. Soc. 144, 375.

21. Culhane, J.L., Sanford, P.W., Shaw, M.L., Phillips, K.J.H., Willmore, A.P., Bowen, P.J., Pounds, K.A., and Smith, D.G. 1969b. A study of the solar soft x-ray spectrum. Mon. Not. R. astr. Soc. 145, 435.

22. Culhane, J.L. and Acton, L.W. 1970. A simplified thermal continuum function for the x-ray emission from coronal plasmas. Mon. Not. R. astr. Soc. 151, 141.

23. de Boer, K.S., Olthof, H., and Pottasch, S.R. 1972. Abundances in the solar Corona. Astron. and Astrophys. 16, 417.

24. Dere, K.P., Horan, D.M., and Kreplin, R.W. 1973. Corrections to solar soft x-ray flux values measured by NRL ionization chamber experiments. NRL Report 7589 (preprint).

25. Dickerman, P.J., and Thornton, E. 1966. Solar Physics 1958-1964, NASA SP-100.

26. Donnelly, R.F. 1968. The x-ray EUV radiation of the August 28, 1966 proton flare as deduced fron SID data. Solar Physics, 5, 123.

27. Donnelly, R.F. 1969. Contribution of x-ray and EUV radiation of solar flares to sudden frequency deviations. ESSA Technical Report, ERL 95-SDL 7.

28. Donnelly, R.F., Wood Jr., A.T., and Noyes, R.W. 1973. The EUV emissions of solar flares: A comparison between OSO-6 spectroheliograph observations and SFDs. Solar Physics, 29, 107.

29. Doschek, G.A., and Meekins, J.F. 1970. Helium-like Ca, Si, and S lines during the decay of a large flare. Solar Physics, 13, 220.

30. Doschek, G.A., Meekins, J.F., Kreplin, R.W., Chubb, T.A., and Friedman, H. 1971a. Helium-like Calcium emission lines observed during a solar flare. Astrophys. J. 164, 165.

31. Doschek, G.A., Meekins, J.F., Kreplin, R.W., Chubb, T.A., and Friedman, H. 1971b. Iron line emission during solar flares. Astrophys. J. 170, 573.

32. Doschek, G.A. 1972. The solar flare plasma: Observation and interpretation. Space Science Reviews, 13, 765.

33. Doschek, G.A., Meekins, J.F., and Cowan, R.D. 1972. Further iron line observations during solar flares. Astrophys. J. 177, 261.

34. Doschek, G.A., Meekins, J.F., and Cowan, R.D. 1973. Spectra of solar flares from 8.5 A to 16 A. Solar Physics, 29, 125.

35. Doschek, G.A., and Meekins, J.F. 1973. Note on He-like Si and S lines observed in the x-ray spectra of solar flares (erratum). Solar Physics, 28, 517.

36. Edlén, B., and Tyrén, F. 1939. Atomic energy states of an unusual type. Nature, 143, 940.

37. Elwert, G. 1954. Die weiche Rontgenstrahlung der ungestörten Sonnenkorona. Z. Naturforsch, 9a, 637.

38. Ermolaev, A.M., Jones, M., and Phillips, K.J.H. 1972. Accurate calculations of wavelengths of certain helium-like lines in the x-ray region. Astrophys. Letters, 12, 53.

39. Flamberg, H. 1942. Arkiv. Mat. Astron. Fys. 28A, 18.

40. Freeman, F.F., Gabriel, A.H., Jones, B.B., and Jordan, C. 1971. Helium-like ion forbidden line emission, and solar active regions. Phil. Trans. Roy. Soc. London, A 270, 127.

41. Friedman, H. 1960. The sun's ionizing radiations. In Physics of the Upper Atmosphere, edited by J.A. Ratcliffe, Academic Press, N.Y., p 133.

42. Friedman, H. 1962. Solar observations obtained from vertical sounding. Reports Prog. Phys. 25, 163.

43. Friedman, H. 1963. I A U Symposium, 16, 45.

44. Fritz, G., Kreplin, R.W., Meekins, J.F., Unzicker, A.E., and Friedman, H. 1967. Solar x-ray spectrum from 1.9 to 25 Å. Astrophys. J. 148, L 133.

45. Froese, C. 1969. A multi-configuration Hartree-Fock Program. Computer Physics Communications, 1, 151.

46. Gabriel, A.H., and Jordan, C. 1969a. Long wavelength satellites to the He-like ion resonance lines in the laboratory and in the sun. Nature, 221, 947.

47. Gabriel, A.H., and Jordan, C. 1969b. Interpretation of solar He-like ion line intensities. Mon. Not. R. astr. Soc. 145, 241.

48. Gabriel, A.H., and Jordan, C. 1972. Interpretation of spectral intensities from laboratory and astrophysical plasmas. In Case Studies in Atomic Collision Physics - II, edited by McDaniel and McDowell, North-Holland Publishing Co.

49. Gabriel, A.H., and Paget, T.M. 1972. Measurement and interpretation of dielectronic recombination satellite intensities. J. Phys. B, 5, 673.

50. Gabriel, A.H. 1972a. Dielectronic satellite spectra in the soft x-ray region. Space Science Reviews, 13, 493.

51. Gabriel, A.H. 1972b. Dielectronic satellite spectra for highly charged He-like ion lines. Mon. Not. R. astr. Soc. 160, 99.

52. Garcia, J.D., and Mack, J.E. 1965. Energy level and line tables for one-electron atomic spectra. J. Opt. Soc. America, 55, 654.

53. Giacconi, R. 1973. X-Ray astronomy. The Physics Teacher, 11, 135.

54. Giovanelli, R.G. 1938. Astrophys. J. 88, 204.

55. Grineva, Yu.I., Karev, V.I., Korneev, V.V., Krutov, V.V., Mandelstam, S.L., Vainstein, L.A., Vasilyev, B.N., and Zhitnik, I.A. 1973. Solar x-ray spectra observed from the 'Intercosmos-4' satellite and the 'Vertical-2' rocket. Solar Physics, 29, 441.

56. Hallam, K.L. 1964. AAS-NASA Symposium on the Physics of Solar Flares. NASA SP-50, p 63

57. Horan, D.M. 1970. Coronal Electron Temperatures Associated with Solar Flares. Ph.D. Thesis, Catholic University of America, Washington, D.C.

58. Horan, D.M. 1971. Electron temperature and emission measure variations during solar x-ray flares. Solar Physics, 21, 188.

59. Horan, D.M., and Kreplin, R.W. 1972. The SOLRAD 10 Satellite, Explorer 44, 1971-058 A. NRL Report 7408.

60. Horan,D.M., Dere, K.P., and Kreplin, R.W. 1973. Electron temperature and emission measure variations in the solar corona. To be published in the Proceedings of the XVI COSPAR Symposium, Konstanz, F.R.G.

61. House, L.L. 1964. Astrophys. J. Suppl. Ser. 8, 307.

62. House, L.L. 1969. Theoretical wavelengths for K type x-ray lines in the spectra of ionized atoms (carbon to copper). Astrophys. J. Suppl. Ser. 18, 21.

63. Hulburt, E.O. 1938. Photoelectric ionization in the atmosphere. Phys. Rev. 53, 344.

64. Jones, B.B., Freeman, F.F., and Wilson, R. 1968. XUV and soft x-ray spectra of the sun. Nature, 219, 252.

65. Jordan, C. 1969. The ionization equilibrium of elements between carbon and nickel. Mon. Not. R. astr. Soc. 142, 501.

66. Jordan, C. 1970. Ionization equilibria for high ions of iron and nickel. Mon. Not. R. astr. Soc. 148, 17.

67. Kafatos, M.C., and Tucker, W.H. 1972. Time-dependent ionization equilibrium and line radiation under flarelike conditions. Astrophys. J. 175, 837.

68. Kane, S.R. 1969. Observations of two components in energetic solar x-ray bursts. Astrophys. J. 157, L 139.

69. Karzas, W.J., and Latter, R. 1961. Electron radiative transitions in a coulomb field. Astrophys. J. Suppl. Ser. 6, 167.

70. Kiepenheuer, K.O. 1964. AAS-NASA Symposium on the Physics of Solar Flares. NASA SP-50, p 323.

71. Kreiger, A.S., and Vaiana, G.S. 1969. Bull. Amer. Astron. Soc. 1, 283 (Abstract).

72. Kreplin, R.W. 1961. Solar x-rays. Ann. Geophys. 17, 151.

73. Kreplin, R.W., Chubb, T.A., and Friedman, H. 1962. X-Ray and Lyman α emission from the sun as measured from the NRL SR-1 satellite. J. Geophys. Res. 67, 2231.

74. Kreplin, R.W., Horan, D.M., Chubb, T.A., and Friedman, H. 1969. Measurements of solar x-ray emission from the OGO-4 spacecraft. In Solar Flares and Space Research, edited by C. DeJager and Z. Svestka, COSPAR Symposium, p 121.

75. Kreplin, R.W., and Meekins, J.F. 1973. Analysis of solar flare x-ray radiation with Bragg spectrometers. To be published in the Proceedings of the XVI COSPAR Symposium, Konstanz, F.R.G.

76. Kundu, M.R. 1965. Solar Radio Astronomy. Interscience, New York.

77. Landini, M., and Monsignori Fossi, B.C. 1970. Solar radiation from 1 to 100 A. Astron. and Astrophys. 6, 408.

78. Landini, M., and Monsignori Fossi, B.C. 1971. A simple formula for the total dielectronic recombination coefficient. Solar Physics, 20, 322.

79. Letfus, V. 1969. Tables for computing dielectronic recombination rates from Burgess' general formula. Bull. astr. Inst. Czech. 20, 159.

80. Lexa, J. 1970. Distribution of ionization stages of argon under coronal conditions. Bull. astr. Inst. Czech. 22, 1.

81. Lytle, F.W., and Bingham, R.G. 1969. Some Diffraction Techniques for X-Ray Astronomy. Boeing Scientific Document No. D1-82-0875, Boeing Aircraft Co., Seattle.

82. Maran, S.P., and Thomas, R.J. 1973. The OSO-7 year of discovery. Sky and Telescope, 45, 4.

83. Martyn, D.F., Munro, G.H., Higgs, A.J., and Williams, S.E. 1937. Ionospheric disturbances, fadeouts and bright hydrogen solar eruptions. Nature, 140, 603.

84. McMaster, W.H., Kerr Del Grande, K., Mallett, J.H., and Hubbell, J.H. 1969. Compilation of X-Ray Crosssections. Lawrence Radiation Laboratory Report UCRL 50174, Sec. 11, Rev. I. University of California, Los Angeles.

85. Meekins, J.F., Kreplin, R.W., Chubb, T.A., and Friedman, H. 1968. X-Ray line and continuum spectra of solar flares from 0.5 to 8.5 Angstroms. Science, 162, 891.

86. Meekins, J.F., Doschek, G.A., Friedman, H., Chubb, T.A., and Kreplin, R.W. 1970. Solar soft x-ray flare spectra from OSO-4. Solar Physics, 13, 198.

87. Meekins, J.F., and Doschek, G.A. 1970. Recombination edges observed in solar soft x-ray flare spectra. Solar Physics, 13, 213.

88. Meekins, J.F. 1972. The NRL OSO-4 Bragg Crystal Spectrometer Instrument. NRL Report 7423.

89. Meekins, J.F. 1973. Solar X-ray Spectra of Coronal Active Regions. Ph.D. Thesis, Catholic University of America, Washington, D.C.

90. Mewe, R. 1972a. Note on the He-like ion line emission in solar plasmas. Solar Physics, 22, 114.

91. Mewe, R. 1972b. Calculated solar x-radiation from 1 to 60 A. Solar Physics, 22, 459.

92. Mitra, A.P. 1972. Interpretation of ionospheric effects of solar flares. In Solar-Terrestrial Physics/1970, edited by E.R. Dyer, Reidel Publishing Co., Holland, Part IV, p 1.

93. Moser, P.J. 1967. NRL OSO-D X-ray Wheel Experiment. NRL (unnumbered).

94. Neupert, W.M., Gates, W., Swartz, M., and Young, R. 1967. Observations of the solar flare x-ray emission line spectrum of iron from 1.3 to 20 A. Astrophys. J. 149, L 79.

95. Neupert, W.M. 1971. Satellite lines in the solar x-ray spectrum. Solar Physics, 18, 474.

96. Newton, H.W., and Barton, H.J. 1937. Bright solar eruptions and radio fadings during the years 1935-36. Mon. Not. R. astr. Soc. 97, 605.

97. Noci, G. 1971. Atomic processes in the solar corona. In the Physics of the Solar Corona, edited by C.J. Macris, Reidel Publishing Co., Holland, p 13.

98. Petersen, L.E., and Winckler, J.R. 1958. Short gamma-ray burst from a solar flare. Phys. Rev. Letters, 1, 205.

99. Rugge, H.R., and Walker, A.B.C. 1968. Solar x-ray spectrum below 25 A. Space Research VIII, 439, North-Holland, Amsterdam.

100. Shore, B.W. 1969. Dielectronic recombination. Astrophys. J. 158, 1205.

101. Skow, M.L. 1962. U.S. Bureau of Mines Information Circular No.8125.

102. SOLAR-GEOPHYSICAL DATA. 1968. IER-FB- 284 to 289, U.S. Department of Commerce, ESSA, Washington, D.C.

103. Speer, R.J., Garton, W.R.S., Goldberg, L., Parkinson, W.H., Reeves, E.M., Morgan, F.J., Nicholls, R.W., Jones, T.J.L., Paxton, H.J.B., Shenton, D.B., and Wilson, R. 1970. Rocket UV flash spectra from the solar eclipse of March 7, 1970. Nature, 226, 249.

104. Thomas, R.J. 1970. Solar Soft X-radiation. Ph.D. Thesis, University of Michigan, Ann Arbor.

105. Tucker, W.H. 1966. Cosmic X-ray Sources. Ph.D. Thesis, University of California.

106. Tucker, W.H., and Koren, M. 1971. Radiation from a high-temperature low-density plasma: The x-ray spectra of the solar corona. Astrophys. J. 168, 283.

107. Vaiana, G.S., Reidy, W.P., Zehnpfenning, T., Van Speybroeck, L., and Giacconi, R. 1968. X-Ray structures of the sun during the importance 1N flare of 8 June 1968. Science, 161, 564.

108. Vaiana, G.S., and Giacconi, R. 1969. Observation of an x-ray flare: Spatial distribution and physical parameters. In the Proceedings of the Conference on Plasma Instabilities in Astrophysics, edited by D.G. Wentzel and D.A. Tidman, Gordon and Breach, New York (preprint).

109. Van Regemorter, H. 1962. Rate of collisional excitation in stellar atmospheres. Astrophys. J. 136, 906.

110. Walker, A.B.C., and Rugge, H.R. 1970. Solar x-ray observations of forbidden lines in the helium isoelectronic sequence. Astron. and Astrophys. 5, 4.

111. Walker, A.B.C., and Rugge, H.R. 1971. Observations of autoionizing states in the solar corona. Astrophys. J. 164, 181.

112. Walker, A.B.C. 1972. The coronal x-spectrum: Problems and prospects. Space Science Reviews, 13, 672.

113. Warwick, C.S. 1963. In Radio Astronomical and Satellite Studies of the Atmosphere, edited by J. Aarons, North-Holland Publishing Co., p 457.

114. Watts Jr., R.N. 1973. Progress Report on SKYLAB. Sky and Telescope, 45, 24.

115. Withbroe, G.L. 1971. The Chemical Composition of the Photosphere and Corona. Presented at the Donald H. Menzel Symposium, Harvard College Observatory, Cambridge, Mass., NBS Special Publication No.353.

116. Wood Jr., A.T., Noyes, R.W., Dupree, A.K., Huber, M.C.E., Parkinson, W.H., Reeves, E.M., and Withbroe, G.L. 1972. Solar flares in the extreme ultra violet I: The observations. Solar Physics, 24, 169.

117. Zirin, H. 1966. The Solar Atmosphere. Blaisdell, New York, p 184.

118. Zirker, J.B. 1970. The excitation equilibrium of coronal ions. Solar Physics, 11, 68.

119. de Jager, C. 1968. Acceleration processes in solar flares. In Mass Motions in Solar Flares and Related Phenomena - Proceedings of the Ninth Nobel Symposium, edited by Y. Ohman, Wiley Interscience Division, New york.

APPENDIX A

IONIZATION AND EXCITATION EQUILIBRIUM

A knowledge of the ionization and excitation (or statistical) equilibrium distribution of coronal ions is necessary to interpret the continuum and line spectra as discussed in Chapter II. Many authors have published these distribution calculations; some of the recent papers are: House (1964), Jordan (1969, 1970), Cox and Tucker (1969), Lexa (1971), Noci (1972), Kafatos and Tucker (1972), and Mewe (1972b). Of these the most extensively used are those of Jordan. The important atomic processes considered and the general method of the ionization and excitation distribution calculations will now be described.

A.1 IONIZATION EQUILIBRIUM

The three important electron-ion interaction processes are described below with their rate coefficients.

(a) Collisional ionization from the ground state of the ion by electron impact. If m represents the degree of ionization of an ion X^{+m} and dN represents the number of events of collisional ionization $X^{+m} \rightarrow X^{+m+1}$ per unit volume in an interval of time dt, then

$$dN = q(X^{+m})\, N_m\, N_e\, dt \tag{A.1}$$

where N_m is the number of ions (X^{+m}) per unit volume, N_e is the number of electrons (cm^{-3}) and $q(X^{+m})$ is the collisional ionization rate coefficient ($cm^3 . sec^{-1}$). A frequently used expression is that given by Burgess and Seaton (1964):

$$q(X^{+m}) = 2 \times 10^{-8}\, T^{\frac{1}{2}} \sum_{\ell} \zeta_{n\ell}\, I_{n\ell}^{-2}\, \exp(-I_{n\ell} / kT) \tag{A.2}$$

where n is the principal quantum number of the outer electrons of the initial ion, ℓ is the orbital angular momentum quantum number, ζ is the number of electrons in the subshell $n\ell$ of the initial ion, $I_{n\ell}$ is the ionization energy (eV) of the electron of the subshell and T is the electron temperature (K). Collisional ionization from excited levels is not important because of the extremely small population of those levels relative to that of the ground term under coronal conditions.

(b) Radiative recombination by electron capture and emission of the released energy as a photon: The number of recombinations dN' per unit volume in the time interval dt is given by

$$dN' = \alpha_r(X^{+m})\ N_{m+1}\ N_e\ dt \qquad \text{(A.3)}$$

where N_{m+1} is the number of recombining ions per unit volume and the radiative recombination rate coefficient α_r is given by

$$\alpha_r = 1.3 \times 10^{-9}\ I_m^{0.5}\ (m + 1)^2\ T^{-1}\ \mathrm{cm}^3\ \mathrm{s}^{-1} \qquad \text{(A.4)}$$

where I_m is the ionization energy (eV) of the lower ionization stage (recombined ion). This is a hydrogenic approximation (Burgess and Seaton, 1964) valid for high temperatures ($T > 6 \times 10^5$ K).

(c) Dielectronic Recombination: Burgess (1964, 1965) describes dielectronic recombination in the following manner:

(i) A colliding electron at below threshold energy excites an ion to a resonance transition, but itself gets trapped in an outer orbital. If autoionization then occurs, no recombination has taken place.

(ii) Alternatively, the doubly excited ion stabilizes by radiative decay of the inner excited electron. The wavelength of the emitted photon is slightly longer than that of the resonance transition of the recombining ion, due to the influence of the additional outer electron (see Figure II-3).

in the equation (A.5a) need be considered. This is rewritten as

$$D = \frac{8.2 \times 10^{-4}}{T^{1\frac{1}{2}}} \; \frac{m^{\frac{1}{2}}\,(m+1)^2}{(m^2+13.4)^{\frac{1}{2}}} \; \frac{f(^1P \rightarrow {}^1S)\; E_o^{\frac{1}{2}}\; \exp(-E_o/kT)}{(1+.105\,\chi + .015\,\chi^2)} \qquad \text{(A.5b)}$$

where E_o is now the energy of the resonance line. The ratio of the dielectronic to the direct contribution (by electron impact excitation) to the resonance line is given by

$$\frac{D\cdot}{C_{\ell u}} = \frac{m^{\frac{1}{2}}\,(m+1)^2}{(m^2+13.4)^{\frac{1}{2}}} \; \frac{0.48}{(1+.105\,\chi + .015\,\chi^2)} \; \frac{E_o^{1\frac{1}{2}}}{P\,T} \qquad \text{(A.5c)}$$

where $C_{\ell u}$ and P are both defined in equation (A.12). This ratio is also discussed in section II.4. Shore (1969) has shown that the expression (A.5b) tends to overestimate the contribution by ~10 per cent for helium-like ions (see Gabriel (1972b) or Tucker and Koren (1971) for details).

Several authors (e.g., Letfus, 1969; Landini and Monsignori Fossi, 1971, and other references given therein) have devised simple expressions for the total dielectronic recombination rate given by equation (A.5a); these are based on the fact that most of the dielectronic recombinations lead to the resonance line of the recombined ion.

The number of dielectronic recombinations per unit volume in a time interval dt is given by

$$dN'' = \alpha_d(X^{+m})\; N_{m+1}\; N_e\; dt \qquad \text{(A.6)}$$

where $\alpha_d(X^{+m})$ is given by equation (A.5a).

The three processes discussed above determine the ionization equilibrium of the coronal ions. In steady state equilibrium the number of ionizations from X^{+m} to X^{+m+1} are equal to the total of all (radiative plus dielectronic) recombinations from X^{+m+1} to X^{+m}. This is written as

$$dN = dN' + dN'' \qquad \text{(A.7)}$$

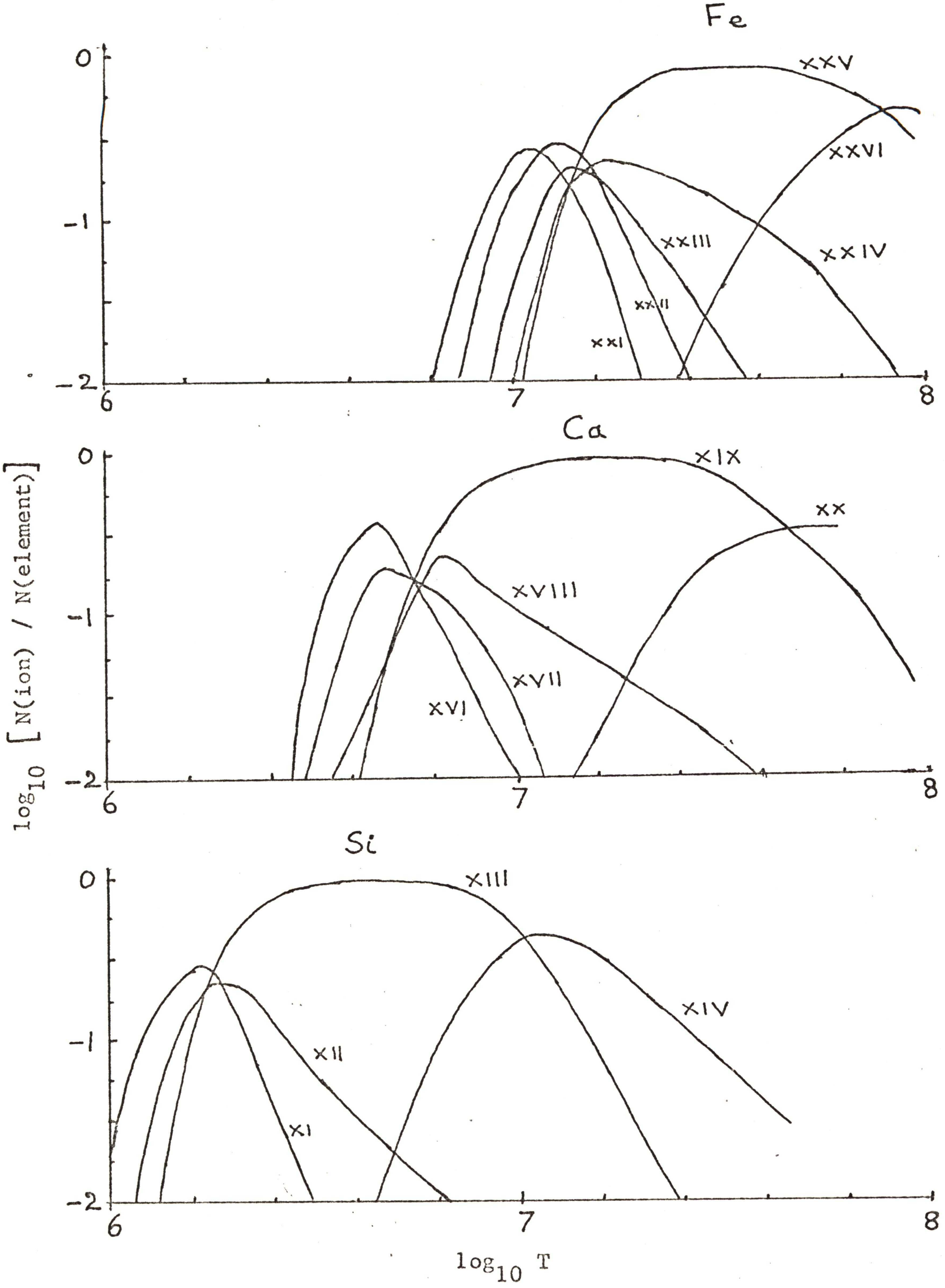

Figure A-1. Ionization eqillibrium curves of silicon, calcium, and iron plotted as a function of temperature (values are based on those of Jordan (1970) and of Mewe (1972b).)

or, $$q(X^{+m})\, N_m N_e\, dt = \left[\alpha_r(X^{+m}) + \alpha_d(X^{+m})\right] N_{m+1} N_e\, dt.$$

Therefore,

$$\frac{N_{m+1}}{N_m} = \frac{q(X^{+m})}{\alpha_r(X^{+m}) + \alpha_d(X^{+m})} \tag{A.8}$$

This equation is independent of N_e and is only a function of the electron temperature. The ionization equilibrium distribution obtained by using the above equation is known as the electron density independent solution.

Minor processes which will not be described here, arise from the excited levels above the ground term. Jordan (1969) has shown that they are generally negligible in the solar corona.

The ionization equilibrium curves for silicon, calcium and iron are presented in Figure A-1.

A.2 STATISTICAL EQUILIBRIUM FOR EXCITED STATES

As in the case of the ionization equilibrium calculations discussed in the previous section, the important atomic processes that govern the excitation (or statistical) equilibrium are quite well understood (see e.g., Zirker, 1970; Blaha, 1971; de Boer et al., 1972; Gabriel and Jordan, 1972). In these calculations, it will be assumed that changes in population of each ion stage are slow compared with excited state redistribution, so that each ion stage has a fixed total population. The energies of the excited states that lead to lines in the x-ray region are so large that only two processes govern the statistical equilibrium between them. They are the electron impact excitation and spontaneous radiative decay. Then the rate of change of the population density N_i of a state i can be expressed as a function of all the other excited states j, as

$$\frac{dN_i}{dt} = \sum_j N_j N_e C(j \rightarrow i) - \sum_j N_i N_e C(i \rightarrow j) + \sum_{j>i} N_j A(j \rightarrow i)$$
$$- \sum_{j<i} N_i A(i \rightarrow j) \qquad (A.9)$$

Here $C(i \rightarrow j)$ is the electron collisional excitation rate (equation (A.14) given below) producing the transition $i \rightarrow j$ and $A(i \rightarrow j)$ is the corresponding spontaneous decay rate (these two quantities will be denoted as C_{ij} and A_{ij} in this thesis from now on). Since the plasma is assumed to be optically thin and the x-ray photon density is very small, photoexcitation is negligible. Mewe (1972a) has shown that excitation by protons is also negligible. Under these conditions the time-independent solution of the equation (A.9) is given by

$$N_i = \frac{N_e \sum_j N_j C_{ji} + \sum_{j>i} N_i A_{ji}}{N_e \sum_j C_{ij} + \sum_{j<i} A_{ij}} . \qquad (A.10)$$

For the ideal corona which is characterized by low electron densities ($\sim 10^{+9}$), the dominating terms are the first one in the numerator and the second one in the denominator in the above expression. Then N_i is given by

$$N_i = N_e N_g C_{gi} / \sum_{\ell<i} A_{i\ell} \qquad (A.11)$$

where N_j is replaced by N_g, the population of the ion in the ground state g from which collisional excitations lead to the population of the excited states. The denominator can be replaced by a single term A_{ig} when only the $i \rightarrow g$ transition is possible.

The general solution of the equation (A.10), however, involves n simultaneous equations where i and j each range from 1 (=g) to n. Blaha (1971), for example, has calculated the excitation equilibrium distribution in Fe XIV with 47 levels.

A.3 EXPRESSION FOR COLLISIONAL EXCITATION BY ELECTRONS

The expression commonly used in published literature for the excitation rate coefficient C_{ij} for the transition i → j by electron collisions is given by

$$C_{ij} = 1.7 \times 10^{-3} f_{ij} E_o^{-1} T^{-\frac{1}{2}} P \exp(-E_o/kT) \quad \text{cm}^3 \text{ sec}^{-1} \qquad (A.12)$$

where f_{ij} = the oscillator strength for the i → j transition,

E_o = the resonance energy of the transition i → j,

T = the electron temperature,

k = Boltzmann's constant,

and P = is a temperature average of the effective Gaunt factor G_{eff} and is tabulated by Van Regemorter (1962). It is slowly varying with respect to the energy of the colliding electron causing the excitation.

Mewe (1972b) expresses P as an analytical expression given by

$$P = A + (By + C) \left(\ln (y+1) - \ln y - 0.4 (y+1)^{-2} \right) \qquad (A.13)$$

where $y = E_o/kT$. The parameters A, B and C are adjusted such that the excitation cross sections fit the available theoretical or experimental data. Their values as well as that of P for allowed transitions in H-, He- and Li-like isoelectronic sequences of coronal ions are also given by Mewe.

Many authors prefer to use the following equivalent expression for C_{ij}. It is given by

$$C_{ij} = 8.63 \times 10^{-6} T^{-\frac{1}{2}} \frac{\Omega_{ij}}{g_i} \exp(- E_o / kT) \qquad (A.14)$$

where g_i = the statistical weight of the initial level i,

and Ω_{ij} = collision strength parameter of the i → j transition.

The collision strength of the transition is given by

$$\Omega_{ij} = 197.4\ g_i\ f_{ij}\ G_{eff}\ E_o^{-1} \qquad (A.15)$$

where the excitation energy E_o is in eV and the other parameters have been defined in the preceding equations. It can be seen that substitution of equation (A.15) in equation (A.14) leads to equation (A.12). Since G_{eff} slowly varies with the energy of the colliding electron, Tucker and Koren (1971) adopt an average value of the expression (A.15) evaluated at an electron energy equal to 1.5 times the resonance energy E_o of the transition. Blaha (1971) expresses Ω as a function of three parameters by fitting them to the collision strength calculated from a Coulomb-Born approximation technique. While this method has merits, it is quite tedious and has been applied only to the Fe XIV ion. Hence it appears that Mewe's approach (equation A.13) is better than that of Tucker and Koren (1971) for the coronal ions considered by them. However, the fact that considerable uncertainties exist in the available data on atomic parameters and also in the element abundances offsets any difference between the methods considered above.

The collisional excitaion (C_{ij} given by equation A.12) and de-excitation (C_{fi}) rates are related to each other through the principle of detailed balance by the expression

$$C_{ji} = (\ g_i\ /\ g_j\ )\ C_{ij}\ \ \exp(\ E_o\ /\ kT\ ) \qquad (A.16)$$

The initial level i usually corresponds to the ground state g of many coronal ions from which collisional excitation takes place (see Table IV-5). When discussing such cases C_{ij} can be rewritten as C_{gj} or C_{gu} $(u = j)$ as is done in Chapter II. A discussion of the various quantum mechanical methods of computing the required atomic parameters (such as the oscillator strength or collision strength for allowed and forbidden transitions) is beyond the scope of this thesis. These topics are reviewed by Gabriel and Jordan (1972)

APPENDIX B

REFLECTIVITY OF CRYSTALS

The following topics are discussed:

(1) Rocking curve of a crystal

(2) Theoretical reflectivity of a crystal

(3) Experimental determination of the integrated reflectivities for several orders of diffraction carried out by Meekins (1973).

Detailed treatment of these topics can be found in Lytle and Bingham (1969), Meekins (1972, 1973), and in Kreplin and Meekins (1973). A brief summary is given below.

B.1 ROCKING CURVE

The Bragg relation describes the condition under which x-ray photons of wavelength λ have a diffraction maximum at an angle θ_B such that

$$\lambda = 2d \sin \theta_B \qquad (B.1)$$

The diffraction profile is not sharp even for a monochromatic radiation, but spreads through a small angle about θ_B. The intensity versus angle relation is called the rocking curve of the crystal and is shown in Figure B-1(a) for a flat crystal. The FWHM (full width at half maximum)

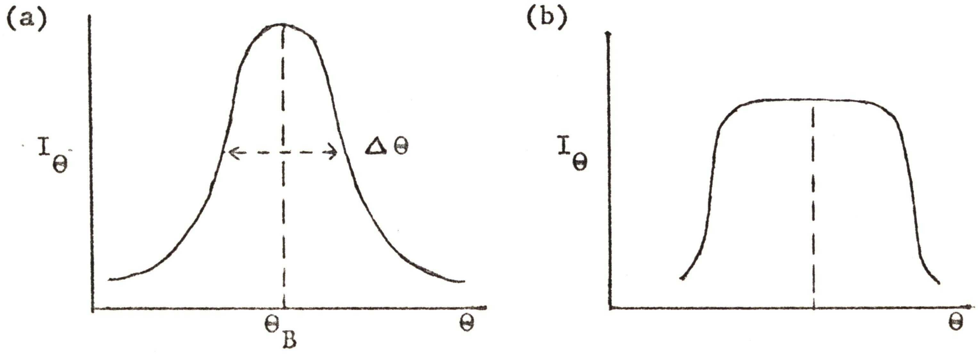

Figure B-1. Rocking curve of (a) a flat, and (b) a bent crystal.

$\Delta\,\theta$ of the rocking curve is about 2 arc minutes or less for the EDDT crystal and about 20 arc minutes for the LiF crystal used in OSO-4 spectrometers. Thus the LiF crystal has a broad rocking curve so that when the stepping motor rotates in steps of 6 arc minutes no line would be missed. But the flat EDDT crystal with its narrow FWHM of 2 arc minutes has a chance of missing the peak of a line. Therefore the EDDT crystal as used in the spectrometer was slightly bent to obtain a square-wave rocking curve of the type shown in Figure B-1(b) with a FWHM of 6 arc minutes. Meekins (1972) has shown on theoretical considerations that the reflectivity (see below) of a bent crystal is the same as that of a flat crystal.

B.2 THEORETICAL REFLECTIVITY (Integrated Reflectivity)

The interaction of the x-ray photon (incident at a suitable angle θ) with the crystal involves not only its diffraction as discussed above but also its reflection. It is the reflectivity of the crystal surface which determines the fraction of the intensity of incident radiation diffracted into the rocking curve. To develop a convenient definition of the reflectivity of the crystal, consider that a narrow monochromatic, parallel x-ray beam is incident upon a plane crystal face. As the crystal is rotated at a uniform rate, ω , through θ_B the intensity of the diffracted (in the first order) beam I_θ traces the rocking curve profile shown in Figure B.1a with total number of photons under the curve equal to E. If the fraction of the total incident beam diffracted at θ is given by

$$\frac{I_\theta}{I_o} = R(\theta) \qquad \text{(B.2)}$$

where I_o is the incident intensity (photon s^{-1}) then

$$\frac{E\,\omega}{I_o} = \int R(\theta)\, d\theta = R(\text{radians}) \qquad \text{(B.3)}$$

R is defined as the integrated reflection coefficient (integral reflectivity or reflecting power), having the dimensions of radians, and is the angular range through which an equivalent amount of diffraction would occur at 100 per cent efficiency. For real crystals the rocking curve can be approximated by a Gaussian curve of the form

$$(\sigma\sqrt{2\pi})^{-1}\exp\left[-(\theta-\theta_B)^2/2\sigma^2\right] \qquad (B.4)$$

where σ is very small ($\sim$1 arc minute) in most cases.

The integral reflectivity R depends on the polarization of the incident radiation. For polarized radiation (magnetic vector $\parallel$ and $\perp$ to the plane of incidence)R can be defined by the sum of the components $R_{\parallel}$ and $R_{\perp}$ so that

$$R = R_{\parallel} + R_{\perp} \qquad (B.5)$$

where $R_{\parallel} = E_{\parallel}\omega/I_{o\parallel}$ and $R_{\perp} = E_{\perp}\omega/I_{o\perp}$.

There are two theories of crystal diffraction, the kinematic theory and the dynamic theory, both of which make idealized assumptions regarding crystal structure (these are discussed in texts on x-ray diffraction e.g., James, R. W. "The Optical Principles of the Diffraction of X-rays", Vol II of The Crystalline State ed. Sir L. Bragg, Cornell U. Press, New York, 1965). These can be used to calculate R for randomly polarized x-radiation.

The kinematic theory assumes an ideally imperfect crystal consisting of a mosaic of small blocks ($\sim$1 micron in size) which may be rotated slightly so that the waves reflected from any one block are incoherent with respect to those from any other block. On this basis the kinematic theory gives, for symmetric Bragg diffraction (diffracting plane parallel to crystal surface)

$$R_{m\parallel} = \frac{r_e^2 N_c^2 \lambda^3 F_{hkl}^2}{2\mu} \quad \frac{1}{\sin 2\theta},$$

$$R_{m\perp} = \frac{r_e^2 N_c^2 \lambda^3 F_{hkl}^2}{2\mu} \frac{\cos^2 2\theta}{\sin 2\theta} ,$$

and $$R_m = R_{m\parallel} + R_{m\perp} \qquad (B.6)$$

where R_m is the integral reflectivity of a mosaic crystal (indicated by the subscript 'm), λ is the wavelength of the incident radiation, θ is the Bragg angle, r_e is the classical electron radius, N_c is the number of elementary cells of the crystal per unit volume, F_{hkl} is a structure factor (h, k, l are Miller indices of the crystal and are the electron positions in reciprocal space), and μ is the mass absorption coefficient of the crystal (a function of λ).

The dynamic theory considers a perfect crystal which has an infinite set of equivalent lattice planes perfectly parallel and equidistant from one another so that the waves reflected from any part of the crystal are coherent with waves reflected from any other part. This theory leads to the following expressions:

$$R_{p\parallel} = \frac{8 r_e N_c \lambda^2 |F_{hkl}|}{3\pi} \frac{1}{\sin 2\theta} ,$$

$$R_{p\perp} = \frac{8 r_e N_c \lambda^2 |F_{hkl}|}{3\pi} \frac{|\cos 2\theta|}{\sin 2\theta} ,$$

$$R_p = R_{p\parallel} + R_{p\perp} \qquad (B.7)$$

where R_p is the integrated reflectivity for a perfect crystal (indicated by the subscript p) and the other terms are defined for the previous equation.

Graphs of R_m and R_p vs λ for LiF crystal are shown in Figure B-2. The calculated values for EDDT crystals are similar (stretched between 1 and 8.8 A).

Real crystals generally have integrated reflectivities which lie

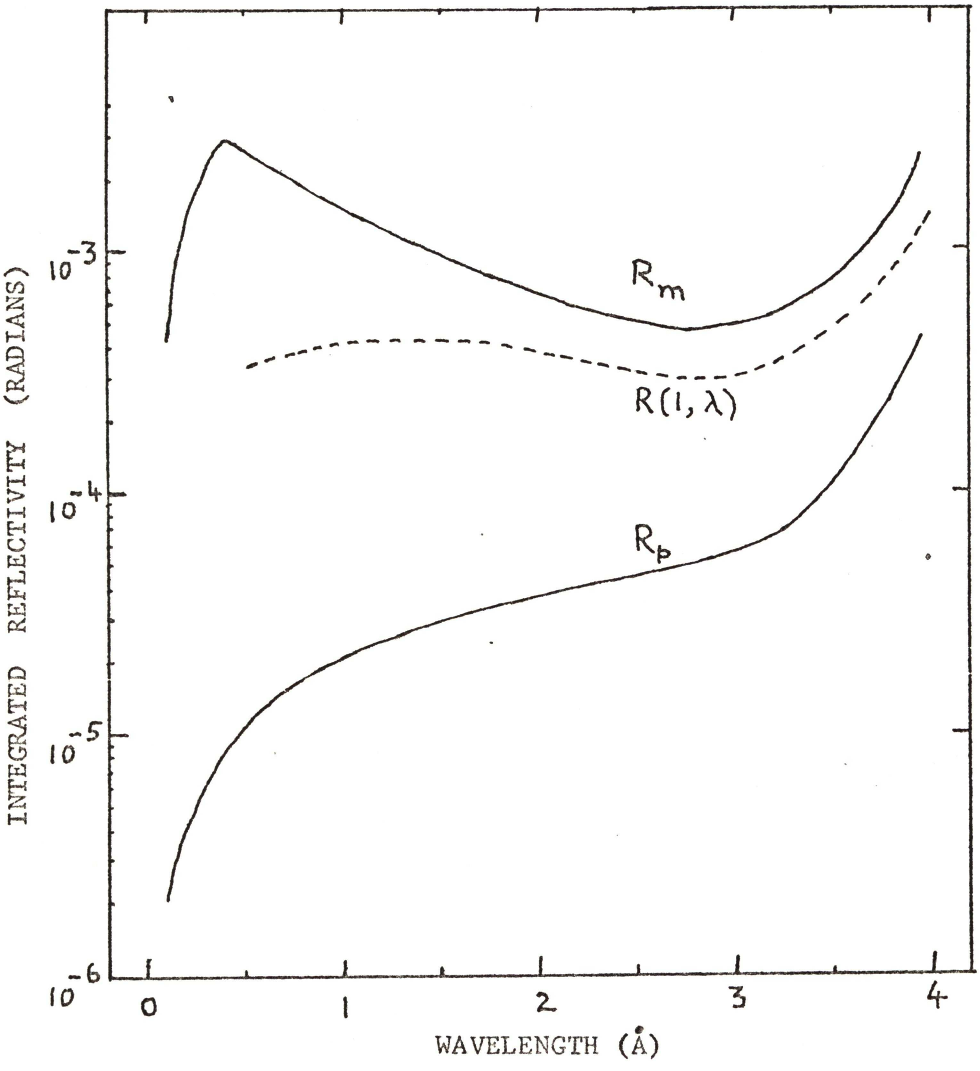

Figure B-2. Integrated reflectivities of LiF crystal (2d=4 Å) are plotted vs λ Å. Solid lines indicate theoretical values R_m and R_p calculated by assuming an ideally mosaic crystal and an ideally perfect crystal respectively. For comparision the experimental value $R(1,\lambda)$ for first order (Meekins, 1973) is also plotted (dashed line).

somewhere between those predicted by the two theories. Therefore reflectivities of real crystals must be measured in the laboratory to insure proper correction of experimental data. This can be appreciated by again referring to Figure B-2 and comparing the experimentally measured (Meekins, private communication) first order reflectivity $R(1, \lambda)$ for LiF crystal used in OSO-4 with the calculated value R_m which was used in computing the theoretical calibration parameter Q (see equation III.21b).

B.3 EXPERIMENTAL DETERMINATION OF CRYSTAL REFLECTIVITY

In the previous section a definition of the integral reflectivity of a crystal (see equation B.3 and Figure B-1a) was given using the concept of sweeping the crystal over the Bragg angle θ. Meekins (1973) has developed this concept into a method of determining integral reflectivities $R(n, \lambda)$ of a crystal for different orders of diffraction of randomly polarized x-radiation. The method involves the use of two crystals, one as a monochromator to diffract radiation of a known wavelength and the other as the test crystal whose reflectivity is to be determined. The x-rays are extracted as a narrow-beam from a Henke source which produces characteristic line radiation and polarized continuum. In Meekins's double crystal spectrometer technique the reflectivity of the test crystal for the unpolarized line radiation is determined after subtracting the effect of the polarized continuum. The reasons for using line radiation are:

(1) Polarization of source radiation is small;

(2) Identification of order and wavelength is simple; and

(3) The integrated reflectivity is related directly to the integral of the detector response under the line (equation B.3).

As the theory of the method is involved only the main aspects of the technique will be mentioned here (details are given in the references mentioned at the beginning of this appendix).

A sketch of Meekins's double crystal spectrometer is shown in Figure B-3. The alignment of the two crystals is in the (1, -1) position. The experiment proceeds according to the following steps:

(1) The first crystal is set at a suitable angle with respect to an incident narrow beam of x-rays so that a selected line is diffracted in the first order. The second crystal (whose face is parallel to that of the first) and its detector scan the line with an angular velocity ω. The integrated intensity (see Figure B-1a), E_{L+C} (1, -1), thus obtained contains the contributions from both line and continuum.

(2) The peak intensity of the line and continuum, I_{L+C}, incident on the second crystal is measured by swinging the second crystal out of the beam. In order to determine the continuum intensity, the first crystal is rotated slightly so that the line is no longer observed and only continuum radiation is seen by the second crystal. Proceeding in the same manner as in step (1) the integrated continuum intensity, $E_C(1, -1)$, reflected by the second crystal and the peak intensity I_C incident on the second crystal are determined.

(3) The effects of the continuum are now subtracted from the total intensities as follows:

$$E_L(1, -1) = E_{L+C}(1, -1) - E_C(1, -1),$$
$$I_L(1, -1) = I_{L+C}(1, -1) - I_C(1, -1),$$

where $E_L(1, -1)$ and $I_L(1, -1)$ are the integrated line intensity (reflected by the second crystal) and peak incident intensity respectively.

(4) The polarization effect due to diffraction from the first crystal was found to be important. To determine this both the crystal and detector

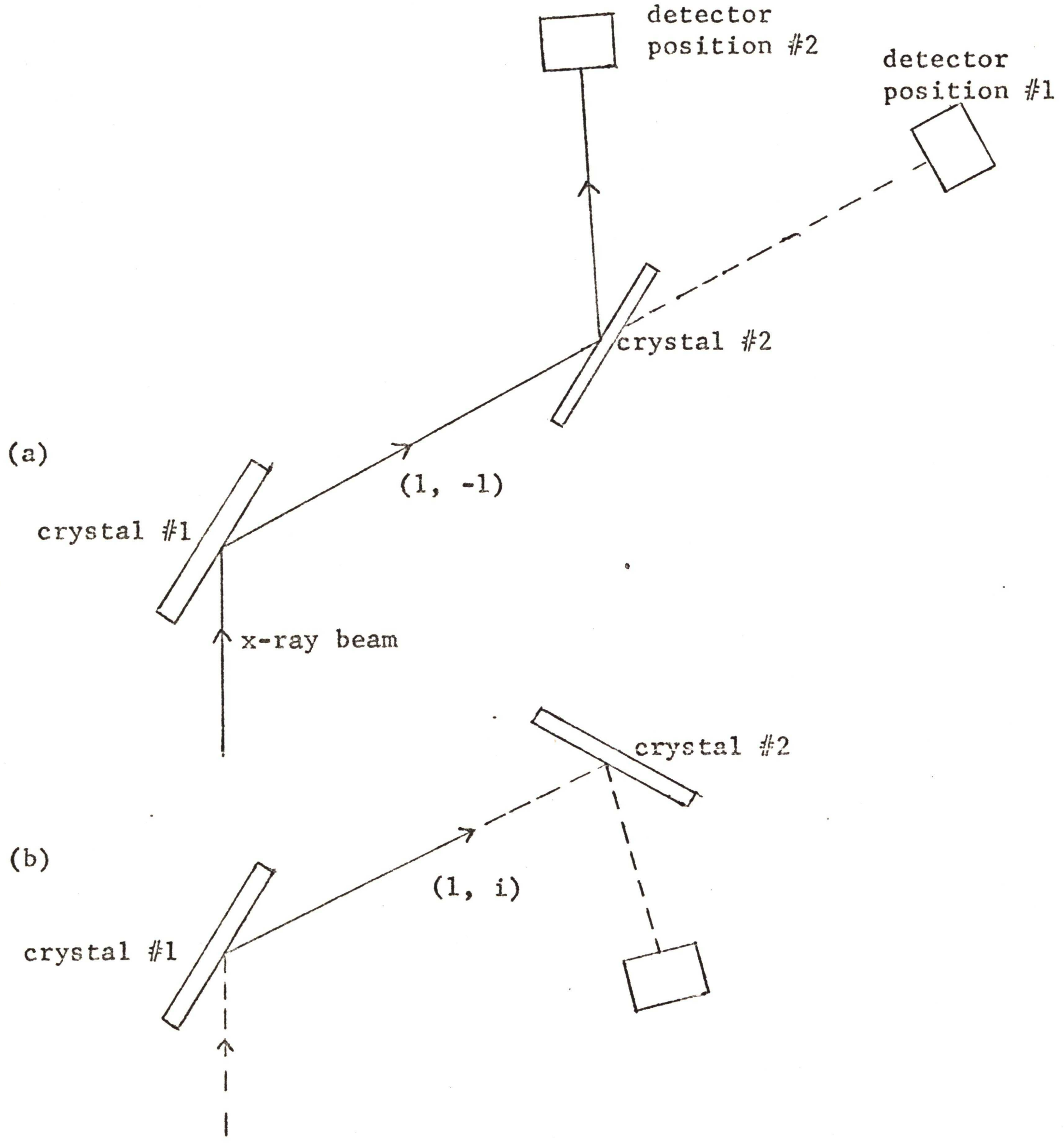

Figure B-3. Schematic of the double crystal spectrometer arrangement employed by Meekins (1973) to determine the integrated reflectivities, $R(n, \lambda)$, of Bragg crystals. (a) Crystals in position (1, -1) with respect to each other; Detector in position #2 measures E (see text); in position #1 measures I with crystal #2 off the beam. (b) Crystals in position (1, i) to investigate polarization effects.

in position 2 are rotated by 90° about the direction of incident radiation, so that the plane of diffraction for the second crystal is perpendicular to the plane of diffraction of the first crystal. This position is referred to as (1, i). The procedure outlined in steps #1, #2 and #3 are now repeated to determine the integral line intensity, $E_L(1, i)$, and the peak incident intensity, $I_L(1, i)$.

Meekins (1973) has derived the following theoretical relationships:

The integral reflectivity for order n in response to random source polarization is given by

$$R(n, \lambda) = \left[A(n, \lambda)\right]^2 \frac{(1 + f_n^2)}{2} \tag{B.8}$$

where $A(n, \lambda)$ is the diffraction amplitude containing the crystal structure factors and f_n contains the polarization factors. In the first order, f is related to the diffraction angle θ by

$$f_1^2 = (\cos 2\theta)^q \tag{B.9}$$

where $q = 1$ for a perfect crystal and $q = 2$ for an ideal mosaic crystal. The measured quantities (in steps #3 and #4 above) are related f_1^2 by

$$H(\lambda) = \frac{E_L(1, i)}{E_L(1, -1)} = \frac{2f_1^2}{1 + f_1^4}, \tag{B.10}$$

and

$$G(\lambda) = \frac{E_L(1, -1)}{I_L(1, -1)} = \frac{\left[A(1, \lambda)\right]^2 (1 + f_1^4)}{\omega\ (1 + f_1^2)} \tag{B.11}$$

where ω is the angular velocity (radians s^{-1}) of the second crystal as determined in step #1 above.

$H(\lambda)$ is determined experimentally for several wavelengths and the resulting values of f_1^2 are used to calculate q by a least-squares fit. Meekins (1973) finds that $q = 1.8$ for the LiF crystal, indicating that it behaves like a mosaic crystal. Once f_1 is determined, the first order amplitude factor $A(1, \lambda)$ can be computed from equation (B.11). Since f_1 and $A(1, \lambda)$ are now known, the first order integral reflectivity $R(1, \lambda)$ is calculated from

$$R(1, \lambda) = \left[A(1, \lambda)\right]^2 \frac{(1 + f_1^2)}{2} \qquad \text{(B.12)}$$

which is the first order version of equation (B.8).

The higher order reflectivities, $R(n, \lambda)$, are now easily determined from the experimentally measured relation for relative reflectivities:

$$F(n, \lambda) = \frac{E_{Ln}(1, -1)}{E_L(1, -1)} = \frac{R(n, \lambda)}{R(1, \lambda)} \qquad \text{(B.13)}$$

where $E_{Ln}(1, -1)$ is the integrated intensity of the line (less continuum) of order n and is determined as described in step #3 above.

Meekins (1973, private communication) has recently determined the values $R(n, \lambda)$ up to order 4 for randomly polarized x-rays incident on the LiF crystal identical to the one used in OSO-4 spectrometer. For comparison $R(1, \lambda)$ is plotted in Figure B-2 along with the theoretical values R_m and R_p. The other experimental reflectivities are shown in Figure IV-2.

APPENDIX C

LIST OF COMMON ISOELECTRONIC TRANSITIONS

Array	Multiplet	Line	Key Letter*
$1s - 2p$	$^2S - {}^2P$	½ - ½,1½	H - Lα
$1s - 3p$	"	"	H - Lβ
$1s - 4p$	"	"	H - Lγ
$1s - 5p$	"	"	H - Lδ
$1s - 6p$	"	"	H - Lϵ
$1s^2 - 1s2p$	$^1S - {}^1P$	0 - 1	He - R
	$^1S - {}^3P$	0 - 2	He - I2
		0 - 1	He - I1
$1s^2 - 1s2s$	$^1S - {}^3S$	0 - 1	He - F
$1s^2 - 1s3p$	$^1S - {}^1P$	0 - 1	He - 2R
	$^1S - {}^3P$	0 - 2,1	He - 2I
$1s^2 - 1s4p$	$^1S - {}^1P$	0 - 1	He - 3R
$1s^2 - 1s5p$	$^1S - {}^1P$	0 - 1	He - 4R
$1s^2\ 2p - 1s2p^2$	$^2P^o - {}^2P$	1½ - 1½	Li - a
		½ - 1½	Li - b
		1½ - ½	Li - c
		½ - ½	Li - d
	$^2P^o - {}^4P$	1½ - 2½	Li - e
		1½ - 1½	Li - f
		½ - 1½	Li - g
		1½ - ½	Li - h
		½ - ½	Li - i
	$^2P^o - {}^2D$	1½ - 2½	Li - j
		½ - 1½	Li - k
		1½ - 1½	Li - l
	$^2P^o - {}^2S$	1½ - ½	Li - m
		½ - ½	Li - n
$1s^2\ 2s - 1s2s^2$	$^2P^o - {}^2S$	1½ - ½	Li - o
		½ - ½	Li - p

LIST OF COMMON ISOELECTRONIC TRANSITIONS (Continued)

Array	Multiplet	Line	Key Letter*
$1s^2\ 2s - 1s2p2s$	$^2S - (^1P)\ ^2P$	½ - 1½	Li - q
		½ - ½	Li - r
	$^2S - (^3P)\ ^2P$	½ - 1½	Li - s
		½ - ½	Li - t
	$^2S - {}^4P$	½ - 1½	Li - u
		½ - ½	Li - v

---

* Lyman lines of hydrogenic ions are abbreviated as $L\alpha$, $L\beta$, $L\gamma$ .... in this thesis. The notation of Gabriel (1972b) is adopted for the lines of lithium-like ions.